

Mg II ABSORPTION AT $2 < Z < 6$ WITH MAGELLAN / FIRE.
II: A LONGITUDINAL STUDY OF H I, METALS, AND IONIZATION IN GALACTIC HALOES ¹

MICHAEL S. MATEJEK², ROBERT A. SIMCOE², KATHY L. COOKSEY^{2,3} AND EDUARDO N. SEYFFERT²

Draft version August 22, 2018

ABSTRACT

We present a detailed study of H I and metals for 110 Mg II absorption systems discovered at $1.98 \leq z \leq 5.33$ in the infrared spectra of high redshift QSOs. Using new measurements of rest-frame UV lines from optical spectra of the same targets, we compare the high redshift sample with carefully constructed low redshift control samples from the literature to study evolutionary trends from $z = 0 \rightarrow 5.33$ (> 12 Gyr). We observe a significant strengthening in the characteristic $N(\text{H I})$ for fixed Mg II equivalent width as one moves toward higher redshift. Indeed at our sample's mean $\bar{z}=3.402$, all Mg II systems are either damped Ly α absorbers or sub-DLAs, with 40.7% of systems exceeding the DLA threshold (compared to 16.7% at $\bar{z}=0.927$). We set lower limits on the metallicity of the Mg II systems where we can measure H I; these results are consistent with the full DLA population. The classical Mg II systems ($W_0^{\lambda 2796} = 0.3 - 1.0 \text{ \AA}$), which preferentially associate with sub-DLAs, are quite metal rich at ~ 0.1 Solar. We applied quantitative classification metrics to our absorbers to compare with low redshift populations, finding that weak systems are similar to classic Mg II absorbers at low redshift. The strong systems either have very large Mg II and Fe II velocity spreads implying non-virialized dynamics, or are more quiescent DLAs. There is tentative evidence that the kinetically complex systems evolve in similar fashion to the global star formation rate. We speculate that if weaker Mg II systems represent accreting gas as suggested by recent studies of galaxy-absorber inclinations, then their high metal abundance suggests re-accretion of recently ejected material rather than first-time infall from the metal-poor IGM, even at early times.

Subject headings: Galaxies: evolution—Galaxies: halos—Galaxies: high-redshift—Infrared: general—intergalactic medium—quasars: absorption lines

1. INTRODUCTION

For decades, Mg II quasar absorption lines have been used to probe the gas distribution in $z < 2.3$ galactic haloes in a largely dust extinction and luminosity-independent manner (e.g., Weymann et al. 1979; Lanzetta et al. 1987; Tytler et al. 1987; Sargent et al. 1988; Steidel & Sargent 1992; Nestor et al. 2005; Prochter et al. 2006; Lundgren et al. 2009). Despite this rich literature, the spatial structure and dynamical history of the gas giving rise to Mg II absorption are not fully understood. Several important clues have surfaced through the aforementioned studies, and (broadly speaking) they point to two plausible mechanisms. The first possibility is that Mg II traces cool clumps embedded in hot galactic outflows (e.g., Zibetti et al. 2007; Bouché et al. 2007; Weiner et al. 2009; Gauthier et al. 2009; Lundgren et al. 2009; Rubin et al. 2010; Noterdaeme et al. 2010; Ménard et al. 2011). The second postulates that Mg II absorbing structures are a manifestation of gravitational and gas accretion processes, perhaps even through recycled and metal-enriched winds (e.g., Chen et al. 2010a,b; Lovegrove & Simcoe 2011; Kacprzak et al. 2011).

The outflow hypothesis is supported by low redshift studies showing a connection between Mg II absorp-

tion and star formation. For example, Zibetti et al. (2007) demonstrated that strong absorber $W_0^{\lambda 2796}$ correlates with blue host galaxy color, using a sample of 2800 strong Mg II systems ($W_0^{\lambda 2796} > 0.8 \text{ \AA}$) at low redshifts ($0.37 < z < 1.0$), a result later corroborated by Lundgren et al. (2009).

More directly, Weiner et al. (2009) observe blueshifted (and hence outflowing) foreground Mg II absorption in the stacked spectra of star forming galaxies. Follow up work by Rubin et al. (2010) verifies this trend and establishes a correlation between Mg II rest-frame equivalent width and star formation rate (SFR). Nestor et al. (2011) studied two ultra-strong Mg II absorbers ($W_0^{\lambda 2796} = 3.63$ and 5.6 \AA) in detail, finding that they were associated with galaxies of unusually high specific star formation rate at their respective masses and redshifts.

Further evidence of a Mg II-wind connection may be found from studying statistical clustering of Mg II systems relative to nearby galaxies. Gauthier et al. (2009), following up on the work of Bouché et al. (2006) and Lundgren et al. (2009), find a 1σ anti-correlation between Mg II rest-frame equivalent width and galaxy halo mass by cross-correlating luminous red galaxies with $W_0^{\lambda 2796} \gtrsim 1.0 \text{ \AA}$ Mg II absorbing systems from SDSS-DR5 at $z \sim 0.5$. Although the anti-correlation is weak, in conjunction with studies showing a strong correlation between $W_0^{\lambda 2796}$ and velocity spread (Ellison 2006; Matejek & Simcoe 2012) it suggests that the individual Mg II systems are not virialized.

While these and other studies (e.g., Bouché et al. 2007; Noterdaeme et al. 2010; Ménard et al. 2011) have

¹ This paper includes data gathered with the 6.5 meter Magellan Telescopes located at Las Campanas Observatory, Chile

² MIT-Kavli Institute for Astrophysics and Space Research, Massachusetts Institute of Technology, 77 Massachusetts Ave., Cambridge, MA 02139, USA

³ NSF Astronomy & Astrophysics Postdoctoral Fellow

advocated outflows as a mechanism for creating Mg II absorption, there is also evidence suggesting that many Mg II systems do not originate in winds. For example, Chen et al. (2010a) find little evidence for correlation between absorber strength and galaxy colors using a galaxy-selected sample of Mg II systems, in direct contrast to Zibetti et al. (2007). Similar galaxy-selected samples of weaker absorbers confirm this result (Lovegrove & Simcoe 2011; Kacprzak et al. 2011). Moreover, Chen et al. (2010b) demonstrate with a sample of 47 weaker (mostly $W_0^{\lambda 2796} < 1 \text{ \AA}$) systems at $z < 0.5$ that the extent of the Mg II halo correlates only weakly with specific star formation rate and increases with galaxy stellar mass. The authors suggest that this may be evidence that Mg II absorbers reside in infalling clouds that later fuel star formation.

Recently, Bordoloi et al. (2011) and Kacprzak et al. (2011) have explored the connection between absorber strength and galaxy-absorber projected inclination, finding evidence for both co-planar and bipolar distributions of absorbing gas. While the outflow hypothesis naturally predicts winds escaping perpendicular to galactic disks as found by Bordoloi et al. (2011), the analysis of Kacprzak et al. (2011) indicates that co-planar gas exists around some systems, as might be found in accreting streams and filaments.

Collectively, these studies seem to suggest that Mg II absorbers fall into at least two categories, as outlined in Kacprzak & Churchill (2011). Loosely speaking, weaker absorbers $W_0^{\lambda 2796} \lesssim 1 \text{ \AA}$ are more likely to possess disk-like kinematics and trace infalling or recycled material. The stronger absorbers $W_0^{\lambda 2796} \gtrsim 1 \text{ \AA}$ have non-gravitational kinematics and are more likely to trace winds. However all of these results were derived from relatively low redshift ($z < 2$) systems that postdate the star formation peak of the universe at $z \sim 2.5 - 3$. Since star formation plays an important role in this discussion, the evolution of Mg II absorbers through the rise and fall of the SFR history provides a diagnostic tool for evaluating the two-sample paradigm. But Mg II absorption at these higher redshifts falls into the near infrared, where atmospheric OH emission and telluric absorption make large systematic surveys much more difficult.

In Matejek & Simcoe (2012; hereafter, Paper I), we presented the first statistically characterized sample of Mg II absorption lines at $z > 2.5$, taken from the spectra of 46 QSO sightlines observed with Magellan/FIRE. We located 110 intervening Mg II systems (plus one proximate system) ranging in rest equivalent width from $W_0^{\lambda 2796} = 0.08 \text{ \AA}$ to $W_0^{\lambda 2796} = 5.58 \text{ \AA}$ and in redshift from $z = 1.98$ to $z = 5.33$. The weaker $W_0^{\lambda 2796} < 1 \text{ \AA}$ systems' linear density dN/dX is statistically consistent with no evolution from $z = 0.4$ to $z = 5.5$ (a span of over 8 Gyr). In contrast, the stronger $W_0^{\lambda 2796} > 1 \text{ \AA}$ systems' linear density increases three-fold until $z \sim 3$ before declining again towards higher redshifts. The evolutionary behavior of these strong systems suggests that there may indeed be a connection between star formation and the strong end of the Mg II population.

The present study follows up the initial survey of Paper I by studying the full properties of each individual $z > 2$ Mg II system in detail. Combination of our data with multiple low redshift samples yields a longitudinal

view of H I and metals in Mg II-selected absorbers over a wide baseline in redshift. For the $z > 2$ sample, we also benefit from the shifting of vacuum ultraviolet lines including H I, C IV, and other baseline metal transitions into optical wavelengths. This allows us to leverage a large assortment of ground based measurements to study the systems' chemistry and ionization.

Our goals in investigating the internal properties of individual Mg II systems over a wide time baseline are: (1) to determine whether the lack of evolution in dN/dX for weak systems (found in Paper I) reflects a truly non-evolving population or rather masks internal evolution that is manifested in other observables; (2) to determine whether the dichotomy between outflowing and infalling Mg II is revealed in properties other than $W_0^{\lambda 2796}$, such as chemical composition or H I column density; and (3) to develop a taxonomy for high redshift systems and determine how these relate to low-redshift classes of Mg II systems and in what proportions.

Section 2 describes our sample data. In Section 3, we describe our data analysis techniques, detailing our calculations of metal rest equivalent widths, column densities, metallicities, and velocity spreads. In Section 4, we present our main science results, including all measured values, correlations, and Kaplan-Meier/K-S test results.

In Section 5, we discuss the implications of these results to the broader question of Mg II absorption. In particular, in Section 5.1 we apply a quantitatively derived taxonomy based upon that in Churchill et al. (2000b) and study the evolution of various classes. In Section 5.2, we compare the Mg II-selected DLA population to the full population. In Section 5.3 we discuss possible interpretations resulting from our chemical composition study.

Throughout this paper we use a Λ CDM cosmology with $\Omega_m = 0.3$, $\Omega_\Lambda = 0.7$, and $H_0 = 70 \text{ km s}^{-1} \text{ Mpc}^{-1}$.

2. DATA SAMPLE

Our overall analysis contains a large number of heterogeneous subsamples both observed by our group and collected from the literature, yielding a total sample of over 17,500 absorbers ranging from $0 < z < 5.3$. In Sections 2.1 and 2.2 we describe the infrared and optical observations of the $z > 2$ systems obtained by our group for the primary survey. Section 2.3 and associated subsections describe the numerous samples collected from the literature that serve as our low redshift control.

2.1. The FIRE Mg II sample

Paper I provides the full details of the acquisition and reduction of this data. Briefly, we observed 46 QSO sightlines with Magellan/FIRE (Simcoe et al. 2008, 2010), between 2010 June and 2011 April. FIRE is a single object, prism cross-dispersed infrared spectrometer with a FWHM spectral resolution of $\sim 50 \text{ km s}^{-1}$. The survey quasars have emission redshifts between 3.55 and 6.28, and were predominantly chosen from the SDSS DR7 quasar catalog (Schneider et al. 2010), although some bright, well-known objects not in the SDSS catalog were also included.

We reduced the data using a custom-developed IDL pipeline named FIREHOSE that evolved from the optical echelle reduction software package MASE (Bochanski et al. 2009). We corrected for telluric absorption features by obtaining spectra of A0V stars at

comparable observing times, air masses and sky positions as our observed QSOs and employing the xtelcor software package (Cushing et al. 2004). The final spectra ranged in median signal-to-noise ratio per pixel from 4.0 to 47.2, with a median value of 12.9.

Using automated techniques with interactive verification, we identified 110 isolated Mg II absorbers ranging in rest equivalent width from $W_0^{\lambda 2796} = 0.08 \text{ \AA}$ to $W_0^{\lambda 2796} = 5.58 \text{ \AA}$ and in redshift from $z = 1.98$ to $z = 5.33$. We carefully characterized both the sample's completeness as a function of $W_0^{\lambda 2796}$ and also its expected false positive rate, adjusting our linear density dN/dX calculations accordingly. Using the supporting optical data compiled for the present paper, we have identified two systems from Paper I likely to fall among these false positives, discussed below. As expected, they are among the weakest systems in the original sample ($W_0^{\lambda 2796} < 0.20 \text{ \AA}$). These absorbers are left out of statistical analysis for both papers because of incompleteness at $< 0.3 \text{ \AA}$; they are also identified accordingly in all tables presented here.

2.2. Supporting Optical Spectra

Rest-frame UV transitions such as Ly α and numerous carbon, silicon, and aluminum transitions are redshifted into the optical window for $z > 1.7$ absorption systems, making these measurements easily accessible from the ground. We obtained new or archival optical spectra for 39 of the 46 QSO sightlines in our survey using data from four different instruments. Table 1 provides a full description of the optical data, including exposure times and wavelength coverages. We limited our metal line search to regions redward of each QSO's Ly α emission peak, and only searched for Ly α absorption redward of the Lyman break for the highest redshift Lyman limit absorber. These requirements set the minimum search wavelength in all our spectra even when the data extended further to the blue.

2.2.1. Magellan/MagE - 15 spectra

We obtained optical spectra of 15 objects with Magellan/MagE, a single-object echellette (Marshall et al. 2008), between 2009 March and 2011 January. We used a 0.7" slit and observed mostly at low airmass in 0.6" to 0.8" seeing. The spectra were reduced using the MASE pipeline (Bochanski et al. 2009). The 1D spectra range in signal-to-noise per pixel redward of the Ly α Forest from 3.5 to 38.5, have a resolution of $\Delta v = 62.1 \text{ km s}^{-1}$, and span $\lambda \sim 3050 \text{ \AA}$ to 10280 \AA .

Representative regions of the MagE spectrum for Q0000-26 are shown at the upper left of Figure 1, which displays all metal lines detected at a 3σ level in the FIRE and MagE spectra at $z = 3.390$. The MagE spectrum for this object has a median signal-to-noise ratio of ~ 23 per pixel redward of the Ly α forest.

In the same MagE spectrum, we did not find a 0.162 \AA Mg II absorber at $z = 2.184$, where the FIRE and the MagE spectra overlap, as reported in Paper I. Since the MagE spectrum has a higher signal-to-noise ratio in this region, we now regard this as a false positive.

2.2.2. MIKE - 2 spectra

For two sample quasars (BR0353-3820 and BR0418-5723) we had high-resolution optical spectra available from previous studies of C IV for other programs (Simcoe 2011). These were taken with the Magellan Inamori Kyocera Echelle (MIKE, Bernstein et al. 2003), between 2004 and 2006. The MIKE spectra have a resolution of 14 km s^{-1} , span the wavelength range $\sim 4900 \text{ \AA}$ to 9400 \AA , and have median signal-to-noise ratios per pixel of ~ 43 for BR0353-3820 and ~ 32 for BR0418-5723.

The upper right set of plots in Figure 1 displays all metal lines detected at a 3σ level for the $z = 2.754$ absorbing system along BR0353-3820, and includes representative samples of the BR0353-3820 MIKE spectrum.

2.2.3. HIRES - 1 spectrum

Q1422+2309 is a well known gravitationally lensed quasar.¹ We obtained a high (~ 40) SNR HIRES (Vogt et al. 1994) optical spectrum of it from A. Songaila's spectral archive at the University of Hawaii². The spectrum, originally published in Ellison et al. (2000), has a resolution of 6.6 km s^{-1} and covers the wavelength range $\sim 4000 \text{ \AA}$ to 7300 \AA . All metal lines detected at a 3σ level for the $z = 3.540$ system along Q1422+2309 found in both its FIRE and HIRES spectra are shown in the bottom left set of plots in Figure 1. The high SNR and resolution of this HIRES spectrum allow us to detect Si II 1304 absorption of only 7 m \AA . It also revealed a greater velocity width for this system than previously reported in Paper I. The updated $W_0^{\lambda 2796}$ and $W_0^{\lambda 2803}$ values used in this study are provided in Table 2. (These adjustments do not effect the dN/dX calculations from Paper I because this system was missed by our automated finder, and therefore was left out of those calculations to avoid overcompensating for incompleteness.)

2.2.4. SDSS - 21 spectra

We downloaded optical counterparts for 21 of the remaining 28 QSO sightlines from the DR7 spectral archives³ of the Sloan Digital Sky Survey (SDSS, Newman et al. 2004). These spectra have a resolution of $\sim 150 \text{ km s}^{-1}$, a wavelength range of ~ 3800 to 9250 \AA , and signal-to-noise ratios per pixel that range from 3.2 to 30.1. The lower right set of plots in Figure 1 includes representative samples of the SDSS spectrum of SDSSJ011351 (signal-to-noise ~ 14), displaying all metal lines detected at a 3σ level for the $z = 3.617$ absorption system found in both its SDSS and FIRE spectra. In general the SDSS spectra are sensitive only to the stronger metal-line systems, but they are very useful for measuring H I column densities.

2.3. Comparison Samples

Since our primary goal is to study the redshift evolution of Mg II-selected systems, we must also establish a local control sample. For this purpose we consider

¹ The lensing galaxy falls at $z = 0.338$ (Kundic et al. 1997), well below the redshift search range for our study. The inclusion of this quasar therefore does not bias our results in this work or in Paper I.

² http://www.ifa.hawaii.edu/users/acowie/spectra/spectra_hires.html

³ <http://das.sdss.org/www/html/>

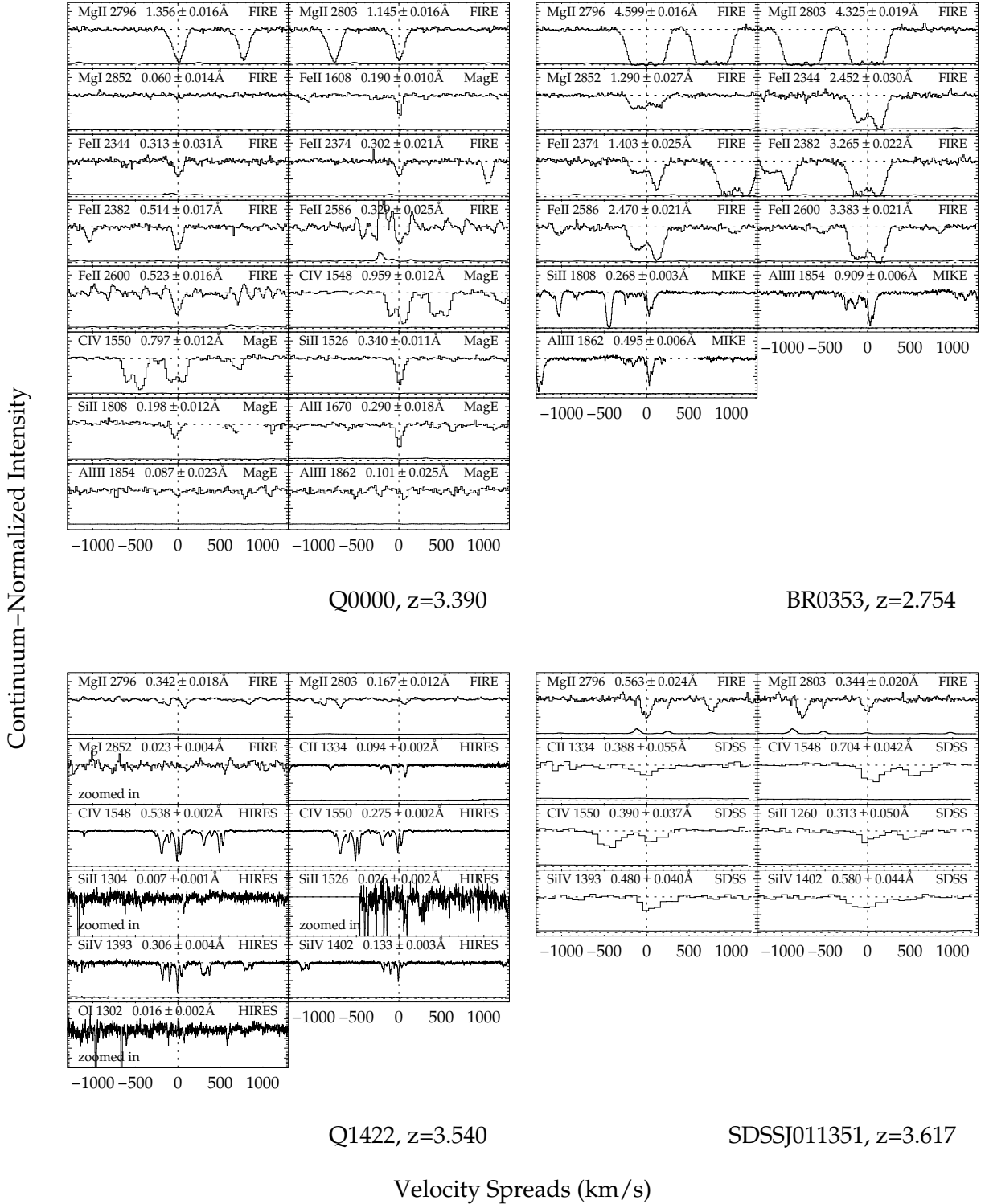


Figure 1. Samples of all absorption lines detected at a 3σ level for 4 of the Mg II-selected systems, with the normalized errors overplotted. The horizontal dotted lines lie at zero flux and at the normalized continuum, and the vertical dotted line coincides with the zero velocity point of the Mg II 2796 transition. The median signal-to-noise ratios per pixel for the FIRE spectra are $\sim 20, 26, 47,$ and 12 from left to right, top to bottom. For the optical counterparts, the corresponding signal-to-noise ratios redward of the Ly α emissions from the QSOs are $\sim 23, 43, 40,$ and 14 . The approximate resolutions of the instruments are 50 km s^{-1} for FIRE, 62.1 km s^{-1} for MagE, 14 km s^{-1} for MIKE, 6.6 km s^{-1} for HIRES, and $\sim 150 \text{ km s}^{-1}$ for SDSS. The Mg I 2852, Si II 1304, Si II 1526, and O I 1302 plots for the $z = 3.540$ Q1422 system are zoomed-in so that the bottom edge lies at 80% of the continuum level. Nearby lines from other systems were masked when deemed distracting.

four comparison sets: a compilation of previously published low redshift metal absorption lines, new measurements of metal lines from a Mg II-selected sample of the SDSS DR7, a low redshift *HST* sample including $N(\text{H I})$ measurements for Mg II-selected systems, and a damped Ly α (DLA) selected metallicity sample from the literature.

2.3.1. Low Redshift Literature Compilation

We conducted an extensive compilation of low redshift ($z < 2.5$) metal absorption lines previously reported in the literature to complement our high redshift survey (Young et al. 1979; Sargent et al. 1979; Young et al. 1982a,b; Wright et al. 1982; Sargent et al. 1982a,b; Robertson & Shaver 1983; Foltz et al. 1986; Lanzetta et al. 1987; Tytler et al. 1987; Sargent et al. 1988, 1989; Steidel 1990; Petitjean & Bergeron 1990; Barthel et al. 1990; Steidel & Sargent 1992; Bahcall et al. 1993; Aldcroft et al. 1994; Petitjean & Bergeron 1994; Bahcall et al. 1996; Storrie-Lombardi et al. 1996; Jannuzi et al. 1998; Churchill et al. 1999, 2000a,b). For this exercise, we included only blind searches of QSOs not selected with any prior knowledge about absorption properties. Because we are studying multiple metal and H I transitions for each Mg II system, we favored surveys that reported all detected transitions, and not simply Mg II (or Mg II and Fe II). In many cases the same object was observed in multiple surveys covering different wavelengths and transitions. To avoid duplication in such instances, we considered absorption systems whose redshifts matched within 250 km s^{-1} to be the same.

For consistency, we converted all absorption features detected at less than a 5σ significance to upper limits and adjusted all reported 3σ and 4σ upper limits to a 5σ level. Unfortunately, most of these surveys do not list upper limits at the expected locations of undetected transitions. This omission becomes important when we attempt to build distribution functions of W_r for each transition using survival analysis. To capture this information in a very conservative way, we estimated upper limits for all unreported transitions that could have been detected in each spectrum given its wavelength bounds. This process is necessarily crude because we did not have access to the original data, but ignoring the effect would bias our W_r distributions to the high side. For each non-detection, we simply assigned an upper limit equal to 5 times the largest error listed for an identified absorption line in that QSO's spectrum. All lines flagged as blends were also treated as upper limits. These blended upper limits, however, violate the principle of random censorship because their values are dependent upon the actual line strengths, and were therefore omitted from survival statistics (Feigelson & Nelson 1985).

In all, we located 2705 unique absorption systems across the surveys listed above. Of these, 393 had Mg II 2796 absorption lines detected at more than a 5σ significance. Within this Mg II subset, we threw out 66 $z \sim 0$ systems and 14 proximate systems (which we defined as residing within $10,000 \text{ km s}^{-1}$ of the QSO). This left us with 313 isolated, Mg II-selected systems in our compilation set. These systems range in redshift from 0.01 to 2.44 and in rest equivalent width

from 0.030\AA to 5.796\AA . Table 3 contains measurements for a selection of these transitions on a system by system basis.

2.3.2. SDSS DR7 Mg II sample

To augment our low redshift data from the literature, we also searched for multiple metal line transitions coincident with Mg II systems identified in spectra from the SDSS DR7 (Seyffert, et al., in prep). Many previous Mg II absorption studies (Nestor et al. 2005; Prochter et al. 2006; Quider et al. 2011) have worked with SDSS spectra, making this a nice comparison set. The SDSS DR7 parent sample includes over 65,000 Mg II systems discovered by an automated continuum fitting and search algorithm and then interactively inspected for final approval. The details of this process may be found in Seyffert, et al. (in prep) and Cooksey et al. (2012).

We only considered the subset of systems from this full set which had the highest possible user-rating on a 4-point scale and $W_0^{\lambda 2796}$ observed at a 5σ significance. Using these redshifts, we re-fit a selection of metal transitions in an automated fashion, and recorded upper limits where no absorption was detected. The final subset included 17,296 Mg II absorption systems with $0.366 \leq z \leq 2.223$ and $0.19\text{\AA} \leq W_0^{\lambda 2796} \leq 7.98\text{\AA}$.

Although this sample contains many more systems than the low redshift compilation discussed last section, the SDSS spectra typically have lower signal-to-noise ratios and are largely incomplete for rest equivalent widths $\lesssim 1.0\text{\AA}$. In addition, the automated determination of metal line rest equivalent widths leaves the sample vulnerable to continuum errors, blended lines, and other effects typically spotted and adjusted for during interactive inspection. For these reasons we use the DR7 sample as a supplement to the low redshift comparison set rather than its replacement, despite its large number of systems.

2.3.3. HST Mg II-selected $N(\text{H I})$ Sample

One of our chief aims is to characterize the H I properties of Mg II systems, but at low redshift only a small fraction of all known Mg II absorbers have H I measurements since the Ly α transition may only be observed from space. Rao et al. (2006) present the largest such sample, with $N(\text{H I})$ measurements of 197 systems taken with the *Hubble Space Telescope* (*HST*), as part of a search for low redshift DLAs. Their survey pre-selects based on Mg II strength of known absorbers identified from a broad literature search (the full list is given in their Table 1). Special preference was given to systems with large Fe II 2600 equivalent width to maximize the yield of DLAs. These Mg II-selected systems range from $z = 0.116$ to 1.645 and $W_0^{\lambda 2796} = 0.300$ to 3.264\AA . The $\log N(\text{H I})$ measurements range from 18.18 to 21.71 cm^{-2} with a mean error across the sample of 0.087 cm^{-2} .

Because this sample was selected specifically to maximize the probability of uncovering DLAs, it is not a statistically representative collection of random Mg II systems. However, it is the largest H I+Mg II compilation known. So, we adopt it below and correct the distribution in postprocessing to make it statistically equivalent to a randomly drawn Mg II population (Section 3.3.3).

2.3.4. Metallicity sample

Another topic of interest is whether the metallicities of Mg II-selected systems differ from the general population at high redshift. Since most Mg II-selected systems are DLAs or sub-DLAs, we use Prochaska et al. (2007) as a comparison set. The authors provide abundance measurements on 86 DLAs found along 42 QSO sightlines taken with HIRES/Keck and 65 QSO sightlines taken with the $R = 13,000$ echellette on the Echellette Spectrograph and Imager (ESI, Sheinis et al. 2002). The DLA absorption redshifts range from 0.613 to 4.282 with a mean of 3.019. These systems were not selected for Mg II, but constitute a high redshift abundance reference.

3. ANALYSIS

3.1. Mg II Line Identification

Paper I contains details of the Mg II line identification algorithm applied to our FIRE data. Briefly, we used an automated continuum fitting algorithm, and then ran a matched filter search using a double Gaussian separated by the Mg II doublet spacing as a kernel. To mitigate the high false positive rate caused by intermittent telluric absorption features and missubtracted emission lines, we subjected each Mg II candidate to a set of consistency checks (e.g., $W_0^{\lambda 2796} \geq W_0^{\lambda 2803}$ within errors). Finally, the surviving candidates underwent a visual inspection before ultimate acceptance. We fit rest equivalent widths to each doublet using boxcar summation between user-defined limits.

3.2. Measurements

3.2.1. Calculating H I Column Densities

For our high-redshift Mg II systems with H I coverage, we manually fit H I column densities with Voigt profiles using the `x_fitdla` routine in the XIDL library.¹ Since all our measured systems turned out to be either DLAs or sub-DLAs (i.e., above the flat portion of the H I curve of growth), our final fits were not sensitive to the b value, and we fixed it at 30 km s^{-1} . This decision was largely a practical consideration, since the QSOs' high redshifts made it highly likely that unassociated Lyman limit absorbers would obscure the measurements of Ly β or higher order transitions.

Toward the low end of the $N(\text{H I})$ range in our sample, the effect of an uncertain b becomes more pronounced, so we account for this in the quoted $N(\text{H I})$ errors for these systems. The resolution of our optical spectra was typically too low to identify individual subcomponents in each absorption system, so we fit only one H I component except for our HIRES spectrum of Q1422 and two complex systems with wide velocity spreads. Even in these cases, the resolution did not allow us to fit unique H I column densities to the individual components. Lyman limit absorption from systems at higher redshift obscured even the Ly α transitions for the majority of our absorption systems; we excluded these from the H I sample.

In all, we were able to measure H I column densities for 33 of the 110 Mg II systems in Paper I. Plots of these Ly α profiles are shown in Figure 2 with their fitted

Voigt profiles overplotted. Table 4 lists all the measured H I column densities.

Some surveys from the literature only quote H I equivalent widths, and we wished to compare our results with these as well. We calculated rest equivalent widths $W_0^{\lambda 1215}$ by integrating the area under the best fit Voigt profiles. Errors on $W_0^{\lambda 1215}$ were conservatively calculated by employing a boxcar summation of the normalized error array where the best fit Voigt profile fell below 10% of the continuum. These rest equivalent widths are stored in Table 5.

As part of this process, we discovered that the putative Mg II system at $z = 2.825$ toward SDSS0113-0935 (reported in Paper I) exhibited no Ly α in its SDSS spectrum even though the data quality and flux level should have allowed such a detection. We therefore consider this system (with $W_0^{\lambda 2796} = 0.194 \text{ \AA}$) a false positive.

3.2.2. Metals

In addition to the Mg II 2796 and Mg II 2803 rest equivalent widths calculated in Paper I, we searched redward of the QSOs' Ly α emission peaks in the FIRE and optical spectra for metal transitions at the locations predicted by the Mg II doublet redshifts. We employed a boxcar method to calculate rest equivalent widths for these lines using interactively-defined limits set to where the flux met the continuum. In some cases, no clear absorption lines existed at the expected locations. In these cases, we estimated an upper limit by boxcar summation of pixels. We made no attempt to disentangle blended lines, treating such collisions as upper limits.

In this way we fit a large assortment of metal transitions including: Mg II 2796, Mg II 2803, and Mg I 2852 (Table 2); Fe II 1608, Fe II 2344, Fe II 2374, Fe II 2382, Fe II 2586, and Fe II 2600 (Table 6); Si II 1260, Si II 1304, Si IV 1393, Si IV 1402, Si II 1526, and Si II 1808 (Table 7); C II 1334, C IV 1548, and C IV 1550 (Table 8); Al II 1670, Al III 1854, and Al III 1862 (Table 8); and O I 1302 (Table 5).

3.2.3. Kinematic Measurements

We fit velocity spreads Δv for all detected metal lines, except those measured with SDSS spectra (which we omitted because of their low resolution). These velocity spreads were calculated by considering the minimum and maximum wavelengths of the absorption line (as determined by the user-defined equivalent width limits, where the absorption line meets the continuum) and correcting for the instrumental resolution of the spectra. We conservatively set the errors on these velocity spreads to be the greater of 10% and the pixel width divided by $\sqrt{2}$.

We also measured the "kinematic spread" ω for each transition, following the analysis of Churchill et al. (2000b). This quantity is defined as the square root of the optical depth-weighted second moment of the velocity difference from the centroid (their Equation 1). Table 9 contains all measured kinematic and velocity spreads for the Mg II 2796, Fe II 2600, and C IV 1548 transitions for the FIRE sample. We substituted measurements for other transitions when possible if the main transition could not be measured (e.g., Fe II 2586 for Fe II 2600).

¹ <http://www.ucolick.org/~xavier/IDL/index.html>

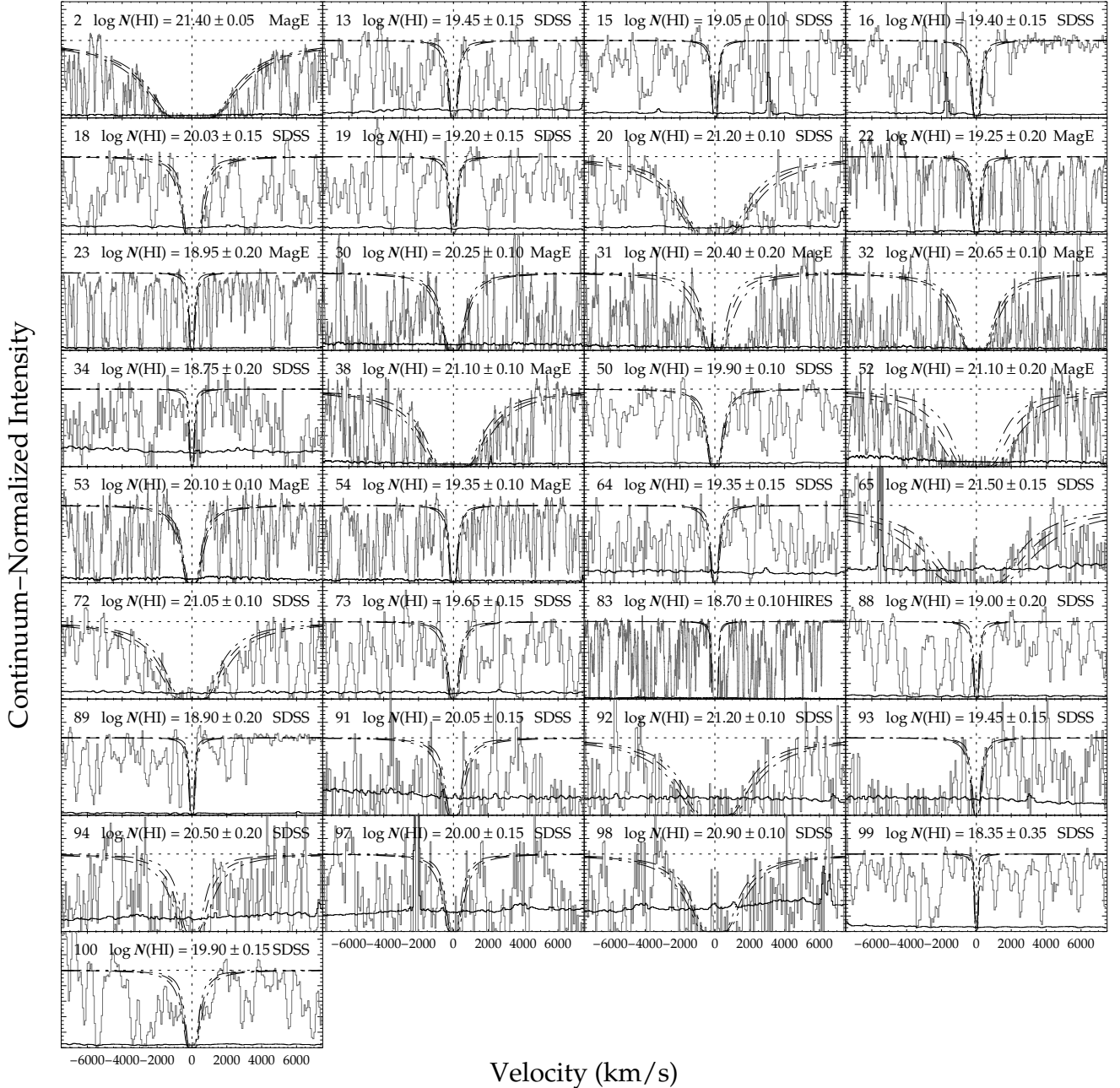


Figure 2. Ly α absorption profiles for the 33 Mg π -selected high redshift systems with $N(\text{H I})$ coverage. The gray line is the continuum normalized intensity, and the solid line is the normalized error. The numbers in the upper left are the system index numbers, as listed in Table 2. For reference, the horizontal dotted line is normalized continuum, and the vertical dotted line rests at the zero velocity point of the H I profile. The three overplotted lines represent the best fit Voigt profile (dashed) and the upper and lower 1σ error lines (dashed-dotted), calculated using the method described in Section 3.2.1. The instrument used in each case is given in the upper right.

We calculated metallicity values or lower limits for the 33 absorption systems with measured H I column densities (Table 4). First, we estimated column densities for all detected metal absorption lines using the apparent optical depth (AOD) method of Savage & Sembach (1991), although the corresponding values represent lower limits on column densities for saturated lines. To determine whether an absorption line was saturated, we estimated the rest equivalent width at which the curve of growth becomes non-linear for each metal transition (conservatively setting $b = 5 \text{ km s}^{-1}$). Since we gener-

ally do not resolve the absorption complexes into their constituent subcomponents, we used this rest equivalent width threshold as the barrier between saturation (stronger absorption) and non-saturation (weaker). This may overestimate the likelihood of saturation for lines with significant velocity substructure, but it provides the most robust possible lower limit.

For each ion (e.g., Fe II), we used the average column densities of all non-saturated transitions (e.g., Fe II 1608, 2344, 2374, 2382, 2586, and 2600) and divided by $N(\text{H I})$ as determined above. When all metal transitions were

saturated, we used the highest value of the lower limit. Finally we normalized to the solar abundance scale of Asplund et al. (2009). We did not apply ionization corrections to the metallicity estimates. This approximation is suitable for DLAs, but may lead to errors at the 0.1-0.3 dex level for lower $N(\text{H I})$ systems in our sample that would be classified as sub-DLAs (P eroux et al. 2007, see also Section 4.4).

3.3. Normalizing Mg II Samples for Statistical Comparison

Given the heterogeneous nature of our high redshift and control samples, we exercised special care to create selected subsamples for statistical comparisons. Our goal is to isolate effects that are intrinsically evolving in the source population, and reduce our sensitivity to observational and/or selection biases that differ between samples.

3.3.1. Generating Low and High Redshift Samples

First, we divided the total set of all Mg II-selected systems from FIRE and the literature compilation with Mg II 2796 detected at a 5σ level into a low redshift and a high redshift sample, separated at $z = 2$. The low redshift compilation set from the literature is predominantly $z < 2$ systems and the FIRE set is predominantly $z > 2$ systems, so these two samples are roughly exclusive. We formed a separate $0.36 < z < 2$ low redshift set from the SDSS data.

Figure 3 shows the cumulative distribution function (CDF) of Mg II 2796 rest equivalent width for our low redshift sample (top panel), high redshift sample (middle panel), and the SDSS sample (bottom panel). In each panel, the light gray line includes all identified Mg II systems, and the dashed black line represents the analytic CDF for an exponential equivalent width distribution ($dN/dW \propto \exp(-W/W_*)$), with W_* appropriate for each respective epoch. For high redshifts we set $W_* = 0.824$, the completeness-corrected value measured in Paper I. For both the low redshift and SDSS DR7 sample, the overplotted exponentials have $W_* = 0.702$, which is the completeness-corrected value from Nestor et al. (2005), measured from the SDSS Early Data Release sample. The large underabundance of systems with small rest equivalent width is an indication of incompleteness.

Following past convention from Paper I, we can minimize incompleteness effects by restricting our analysis to $W_0^{\lambda 2796} \geq 0.3 \text{ \AA}$ systems. The dark gray lines in Figure 3 display the CDFs for this cut, while the solid black curves represent the same analytically calculated CDFs as before, but with this lower limit imposed. The analytic and observed distributions show good agreement for the high and low redshift subsamples. The SDSS DR7 sample still suffers from incompleteness issues below $\sim 1 \text{ \AA}$. Rather than slicing all data to $W_0^{\lambda 2796} \geq 1.0 \text{ \AA}$ (which would result in very few systems at high redshift), we instead forced the SDSS set to fit the analytic CDF by drawing an appropriately weighted subsample from the SDSS parent population. The resulting CDF of this subset is overplotted in Figure 3 as a dotted, dark gray line.

Figure 4 displays histograms of the redshift (upper panel) and rest-frame equivalent width (lower panel)

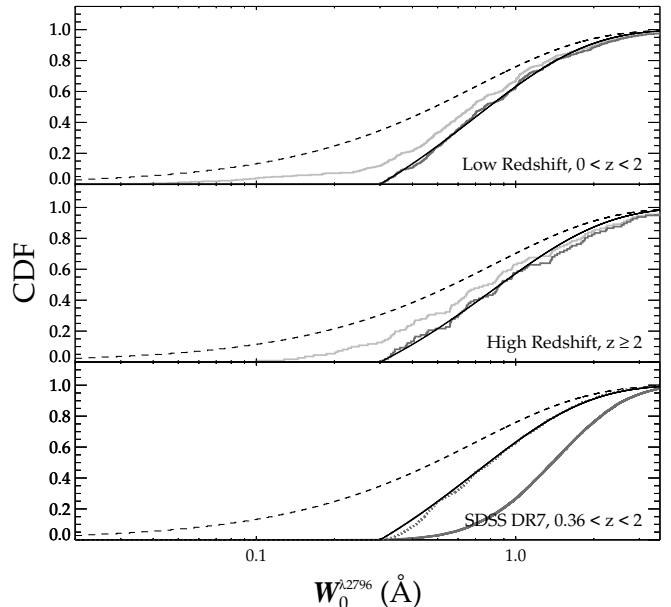


Figure 3. The CDFs for Mg II rest-frame equivalent width for the low redshift ($0 < z < 2$; upper panel), high redshift ($z \geq 2$; middle panel), and SDSS DR7 ($0.36 < z < 2$; lower panel) samples, as described in Section 3.3.1. The light gray lines are CDFs including all Mg II systems, and the dark gray lines are those under the restriction $W_0^{\lambda 2796} \geq 0.3 \text{ \AA}$. The black lines are analytically derived CDFs assuming an exponential frequency distribution $dN/dW = \exp(-W/W_*)$ for all (dashed) and $W_0^{\lambda 2796} \geq 0.3 \text{ \AA}$ (solid) systems. The critical scaling parameters W_* are taken from completeness-corrected maximum likelihood estimates in Paper I (for the high redshift sample) and Nestor et al. (2005, for the low redshift and SDSS samples). Making a $W_0^{\lambda 2796} \geq 0.3 \text{ \AA}$ cut eliminates the incompleteness evident when considering all systems in the low and high redshift samples. Also plotted as a dotted, dark gray line for the SDSS plot is the CDF for the subsample drawn to mimic the analytical CDF with $W_0^{\lambda 2796} \geq 0.3 \text{ \AA}$.

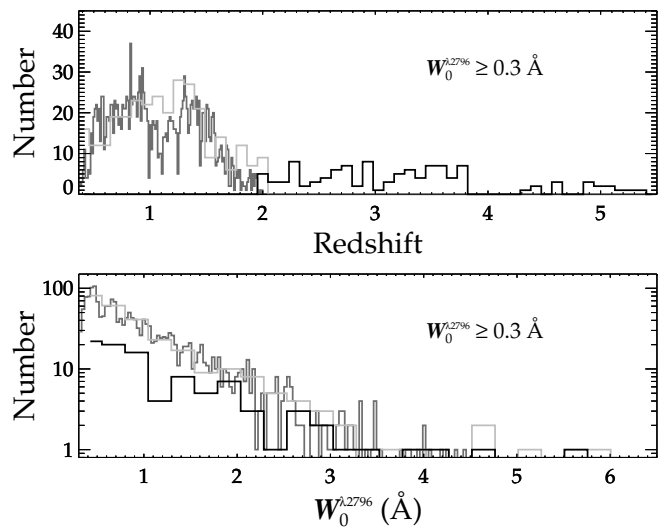


Figure 4. Histograms in redshift (upper panel) and $W_0^{\lambda 2796}$ (lower panel) for the final $0 < z < 2$ low redshift (light gray line), $z \geq 2$ high redshift (black line), and $0.36 < z < 2$ SDSS DR7 (dark gray line) samples. The bin density for the SDSS DR7 sample is eight times larger in order to facilitate overplotting. Section 3.3.1 details the creation of these samples, which are restricted to $W_0^{\lambda 2796} \geq 0.3 \text{ \AA}$.

for these lower redshift (light gray line), higher redshift (black line), and SDSS DR7 (dark gray line) samples. The bins for the SDSS DR7 sample are eight times smaller in order to facilitate overplotting. The low z , high z , and SDSS samples contain 272, 97, and 1975 systems at mean redshifts of 1.128, 3.184, and 1.064, respectively. Table 10 lists the mean redshift, number of detections and upper limits, and minimum and maximum rest-frame equivalent widths for a selection of metal transitions in each sample.

Because our low/high redshift cut was motivated chiefly by observational setup (optical versus IR Mg II measurement), the designations are arbitrary with respect to any physical evolution. To test another prescription, we generated a second redshift classification with three bins at $0 < z < 1.5$, $1.5 \leq z < 3$, and $z \geq 3$ using identical methods. The final low, mid, and high z samples contained 217, 100, and 52 systems at mean redshifts of 0.968, 2.092, and 3.780, respectively. Table 11 contains a breakdown of the mean redshift, number of detections and upper limits, and minimum and maximum rest frame equivalent widths for various metal transitions for each of these three redshift groups.

3.3.2. Generating Weak and Strong $W_0^{\lambda 2796}$ Samples

In Paper I, we presented evidence of differential evolution for strong versus weak Mg II absorbers. For the weak systems with $0.3\text{\AA} < W_0^{\lambda 2796} < 1.0\text{\AA}$, dN/dX is statistically consistent with no evolution, but for strong $W_0^{\lambda 2796} > 1.0\text{\AA}$ absorbers it rises until $z \sim 2 - 3$ and then falls again. For this paper we form separate weak and strong $W_0^{\lambda 2796}$ samples to investigate whether the full chemical compositions of weak and strong absorbers also differ.

We began with the 272 low redshift and 97 high redshift systems from the comparison samples described in Section 3.3.1. We wanted to avoid our final subsamples containing disproportionately more low redshift systems, so we only included a subset of 97 of these low redshift systems in our final absorption strength samples. (This subset has a greater than 99.99% K-S probability of being drawn from the same $W_0^{\lambda 2796}$ distribution as the full low redshift sample; i.e., it is not an unusual draw). The final result is a weak Mg II absorber sample with $0.3\text{\AA} \leq W_0^{\lambda 2796} \leq 1.0\text{\AA}$ containing 119 systems, and a strong Mg II absorber sample with $W_0^{\lambda 2796} > 1.0\text{\AA}$ containing 75 systems. Table 12 contains a breakdown of the mean redshift, number of detections and upper limits, and minimum and maximum rest-frame equivalent widths for these weak and strong Mg II samples.

We additionally constructed a series of four subsamples split along both redshift and Mg II absorption strength (high/low redshift, weak/strong equivalent width) with the goal of studying the redshift evolution of weak and strong Mg II absorbers. We created these four subsamples by dividing the representative low ($0 < z < 2$) and high ($z \geq 2$) redshift samples of Section 3.3.1 into two groups each, comprising weak ($0.3\text{\AA} \leq W_0^{\lambda 2796} \leq 1.0\text{\AA}$) and strong ($W_0^{\lambda 2796} > 1.0\text{\AA}$) absorbers. Table 13 contains the analogous sample count information for this set.

3.3.3. Normalizing Biases in the $N(\text{H I})$ Sample

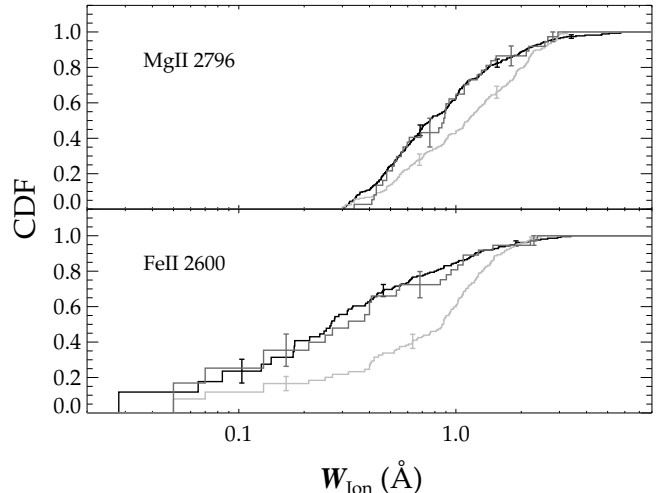


Figure 5. Cumulative distribution functions in rest-frame equivalent width for Mg II 2796 (upper panel) and Fe II 2600 (lower panel). The black lines are for the low redshift sample ($0 < z < 2$, $W_0^{\lambda 2796} \geq 0.3\text{\AA}$) described in Section 3.3.1, and the light gray lines are for the *HST* sample of Rao et al. (2006). The *HST* sample has an overabundance of strong Mg II 2796 and Fe II 2600 absorbers relative to the low redshift sample. The CDFs for the subsample of 37 *HST* systems chosen to match the low redshift sample’s Mg II 2796 and Fe II 2600 distributions are overplotted with dark gray lines. A few representative error bars have been overplotted.

We use the *HST* $N(\text{H I})$ measurements of Rao et al. (2006) as a low redshift H I control sample, but these authors’ primary goal was to locate DLAs, and Mg II measurements mostly served as a means to this end. Rao & Turnshek (2000) previously showed that 11 of 12 DLAs in their sample had $W_0^{\lambda 2796} > 0.6\text{\AA}$, and more than half of all absorbers with $W_0^{\lambda 2796} > 0.5\text{\AA}$ and $W_0^{\lambda 2600} > 0.5\text{\AA}$ yielded DLAs. Accordingly Rao et al. (2006) preferentially observed systems with both strong Mg II and Fe II. Notably, the only $W_0^{\lambda 2796} < 0.6\text{\AA}$ systems included in this sample were those already observed in Rao & Turnshek (2000), or those serendipitously along the same QSO sightlines as other systems with strong Mg II and Fe II.

Figure 5 shows the cumulative distribution functions for $W_0^{\lambda 2796}$ (upper panel) and $W_0^{\lambda 2600}$ (lower panel) for the full low redshift $z < 2$ sample described in Section 3.3.1 (black lines) and the *HST* H I sample (light gray lines). We derived the CDFs for Fe II 2600, which include upper limits, from the Kaplan-Meier estimator using the Astronomy Survival Analysis (ASURV) package (Lavalley et al. 1992), which implements the methods of Feigelson & Nelson (1985). The CDFs show how, by construction, the *HST* sample systematically favors high rest equivalent width systems in both Mg II and Fe II, relative to a randomly selected population of intervening absorbers.

For statistical analysis, we therefore extracted a subset of the *HST* sample to match the $W_0^{\lambda 2796}$ and $W_0^{\lambda 2600}$ distributions of the low redshift sample. First, we made an estimate of the number of *HST* systems required in each of 4 logarithmically-spaced $W_0^{\lambda 2796}$ bins in order to match the distribution of the low redshift sample. We then ran a Monte Carlo simulation that provided 2500 possible realizations with this broad-stroke binning property. For each of these realizations, we calcu-

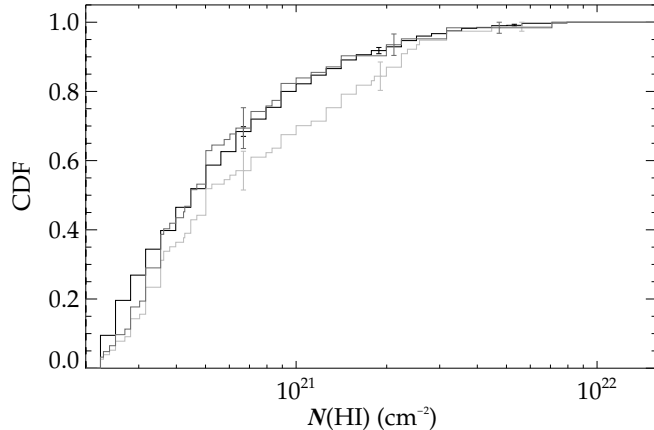


Figure 6. Cumulative distribution functions in $N(\text{H I})$ for systems in the Prochaska et al. (2007) sample (light gray line) and the SDSS DR5 DLA sample (black line) with $z \geq 2$ and $\log N(\text{H I}) \geq 20.3 \text{ cm}^{-2}$ (with a few representative error bars overplotted). The Prochaska et al. (2007) sample shows a preference for stronger $N(\text{H I})$ systems relative to the SDSS survey, possibly a sign of observer bias in selecting targets. The dark gray line represents the unbiased Prochaska et al. (2007) DLA subsample with 62 systems derived using the process described in Section 3.3.4.

lated the two-sample logrank, Gehan, and Peto-Prentice probabilities that the low redshift and *HST* samples were drawn from the same distribution for *both* the Mg II and Fe II distributions using the ASURV package. The final subsample exhibited the highest geometric mean of these six probabilities.

The CDFs for this final subsample are shown as the dark gray lines in Figure 5. The final subsample contains 37 systems ranging in redshift from 0.430 to 1.645, with a mean redshift of $\bar{z} = 0.927$. The geometric mean of the three two-sample tests performed is 82.1% for the $W_0^{\lambda 2796}$ distributions and 71.1% for $W_0^{\lambda 2600}$ distributions. Clearly this procedure has effectively eliminated the bias towards stronger Mg II and Fe II systems.

Our high redshift Mg II-selected $N(\text{H I})$ sample should not suffer from similar selection bias since the Mg II systems were selected randomly and H I measurements were obtained for all systems not blocked by an intervening Lyman limit. To verify this expectation, we performed a Kolmogorov-Smirnov test, finding a 96.7% probability that the $W_0^{\lambda 2796}$ distribution for our H I-measured subset is drawn from the same distribution as the full high redshift sample.

3.3.4. Normalizing biases in the Metallicity Sample

As accounted by the authors, the Prochaska et al. (2007) sample of DLA abundance measurements represents an inclusive compilation of observed DLAs at the time of publication, but it is not a statistically characterized random sample (mostly likely due to observer selection bias towards stronger $N(\text{H I})$ systems). This is evident in Figure 6, where the $N(\text{H I})$ CDF for this sample (light gray line) is shown against that of a DLA survey from the SDSS DR5, as provided by Prochaska & Wolfe (2009, black line; taken to be a statistically random sample). Both samples in this plot are limited to $z \geq 2$ and $\log N(\text{H I}) \geq 20.3 \text{ cm}^{-2}$ systems, for which the Prochaska et al. (2007) sample contains 77 systems and the DR5 sample contains 1029 systems.

We created our final high redshift metallicity compar-

ison set from the Prochaska et al. (2007) systems using the SDSS DR5 DLA sample as a comparison set and a procedure similar to that used in Section 3.3.3. Our Monte Carlo simulation generated 2500 possible comparison samples that met the broad-scale binning requirements in $\log N(\text{H I})$ set by the SDSS DR5 DLA $z \geq 2$ sample. For each of these realizations, we calculated the two-sample logrank and Gehan probabilities that the sample was drawn from the same distribution as the SDSS DR5 DLA sample. (The Peto-Prentice test is redundant with the Gehan test in the absence of upper limits, and was therefore excluded.) We chose the final sample to be that with the highest geometric mean of these two probabilities.

The final high redshift metallicity sample consists of 62 DLAs, ranging in redshift from 2.076 to 4.244, with a mean redshift of $\bar{z} = 3.273$. This distribution and the SDSS $z \geq 2$ DR5 DLA distribution had two-sample logrank and Gehan probabilities of 98.2% and 69.8% of being drawn from the same parent distribution. The CDF of the final DLA/abundance control sample is shown in Figure 6 as the dark gray line.

4. RESULTS

Figure 7 displays scatter plots of all metal rest equivalent widths from the low redshift literature compilation, FIRE, and SDSS DR7 samples (not just those included in the unbiased subsamples). The black and light gray dots represent systems with $z \geq 2$ and $z < 2$, respectively, from the FIRE and literature compilation samples, and the dark gray dots represent measurements from the SDSS DR7 sample.

The scatter plots for individual transitions indicate that for most elements, the loci occupied by low and high redshift points are largely overlapping. The major exception is for H I, which is clearly higher for the high redshift sample. There are hints of offsets in Al III and select transitions of Fe II. But the influence of upper limits and saturation are not at first clear in this view. To better quantify these effects, we have therefore constructed CDFs (accounting for upper limits) for each ion ratio relative to Mg II and performed two-sample tests to discern whether evolutionary trends may be extracted from the scatter.

4.1. H I Evolution in Mg II-selected Systems

Figure 8 displays the CDFs of $N(\text{H I})$ for the $W_0^{\lambda 2796} \geq 0.3 \text{ \AA}$ Mg II-selected systems in the low ($z < 2$; thick, light gray line) and high ($z \geq 2$; thick, black line) redshift samples. Every such Mg II system at $z \geq 2$ is optically thick to H I, with 11 of 27 exhibiting DLA column densities ($40.7_{-9.2}^{+9.8}\%$). The Mg II-selected sample at $z > 2$ has a mean log column density (20.16 cm^{-2}) that nearly meets the DLA threshold.

From this plot, it is also clear that Mg II absorbers are associated with stronger $N(\text{H I})$ absorption at high redshifts. In spite of the relatively small sample sizes, a Kolmogorov-Smirnov test gives only a 0.008 percent probability that the two samples were drawn from the same distribution. Also overplotted (thin, light gray lines) are the 2nd, 3rd, and 4th best-matched low redshift $N(\text{H I})$ samples from the MC simulation discussed in Section 3.3.3. These also provide K-S probabilities of

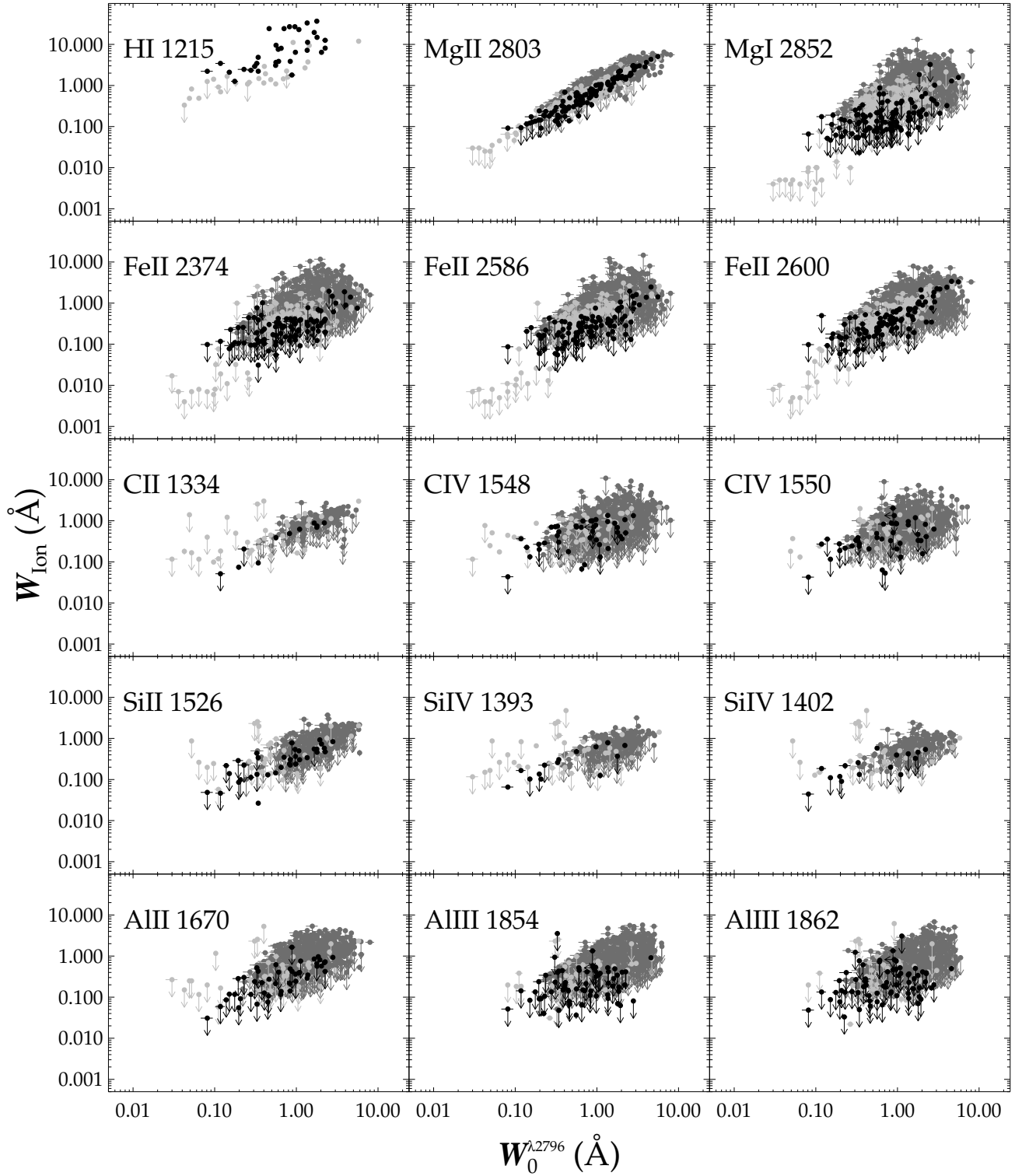


Figure 7. Rest-frame equivalent widths for various ions versus $W_0^{\lambda 2796}$. The dark gray points are from the full SDSS DR7 sample ($0.36 < z < 2.23$), and the light gray points and black points are the low ($0 < z < 2$) and high ($z \geq 2$) redshift systems, respectively, for the full literature compilation and FIRE sets (not the completeness-corrected samples). All of the FIRE measurements are listed in Tables 2, 5, 6, 7, and 8. A subset of the literature compilation measurements are listed in Table 3.

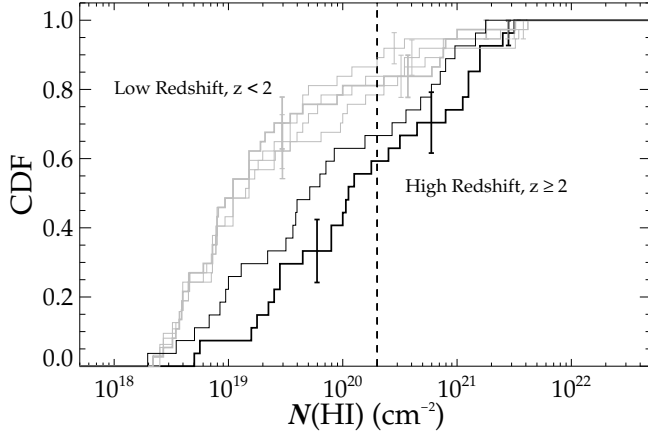


Figure 8. Cumulative distribution functions for $N(\text{H I})$ for the unbiased, $W_0^{\lambda 2796} \geq 0.3 \text{ \AA}$ low redshift ($z < 2$; thick, light gray line) and high redshift ($z \geq 2$; thick, black line) samples described in Section 3.3.3 (overplotted with a few representative error bars). The Mg II absorbers from the high redshift sample are typically associated with much larger H I column densities. A K-S test provided only a 0.008% probability that the two samples were drawn from the same distribution. Also overplotted are the 2nd, 3rd, and 4th best-matched low redshift $N(\text{H I})$ samples (thin, light gray lines) from the MC simulation discussed in Section 3.3.3. These also provide K-S probabilities of $< 0.1\%$, suggesting that this result is robust to the exact sample chosen. The thin, black line represents the high redshift sample, but with $\log N(\text{H I})$ values 3σ lower than calculated. This distribution has only a 2.0% K-S probability of deriving from the same parent distribution as the low redshift sample, suggesting that our results are robust to large, systematic overestimates of $\log N(\text{H I})$ as well.

$< 0.1\%$, suggesting that this result is robust to the exact sample chosen. In addition, the overplotted thin, black line represents the CDF for the high redshift sample, but with all measurements shifted 3σ lower than calculated. This distribution has only a 2.0% K-S probability of deriving from the same parent distribution as the low redshift sample, suggesting that our results are also robust to large, systematic overestimates of $\log N(\text{H I})$.

Only $16.7^{+7.1}_{-5.3}\%$ of the low redshift sample systems are associated with DLAs, as compared to $40.7^{+9.8}_{-9.2}\%$, or about than 2 in 5, in the high redshift sample. Figure 9 shows the percentage of Mg II systems in the low (light gray line) and high (black line) redshift samples exhibiting DLA column densities for $0.3 \text{ \AA} \leq W_0^{\lambda 2796} \leq W_{0,\text{max}}$ and varying values of $W_{0,\text{max}}$.

Figure 10 more directly illustrates the redshift evolution in $N(\text{H I})$ by plotting the H I column densities for all systems in the representative subsets against redshift. The solid line represents an iterative sigma-clipped linear fit $\log N(\text{H I}) = (0.359 \pm 0.081)z + (18.966 \pm 0.153) \text{ cm}^{-2}$. The dotted lines are the one sigma limits. The evolution is significant at a $> 4\sigma$ level, with the best fit line increasing from $\log N(\text{H I}) \sim 19$ at $z \sim 0$ to above the DLA threshold (dashed line) for $z > 4$.

4.2. Chemical Evolution in Mg II-selected Systems

Figure 11 provides CDFs—calculated using the Kaplan-Meier estimator—of the equivalent width for each heavy element ion we measured, after normalizing by $W_0^{\lambda 2796}$. Separate curves are shown for the low redshift sample ($z < 2$; light gray lines), the high redshift sample ($z \geq 2$; black lines), and the SDSS sam-

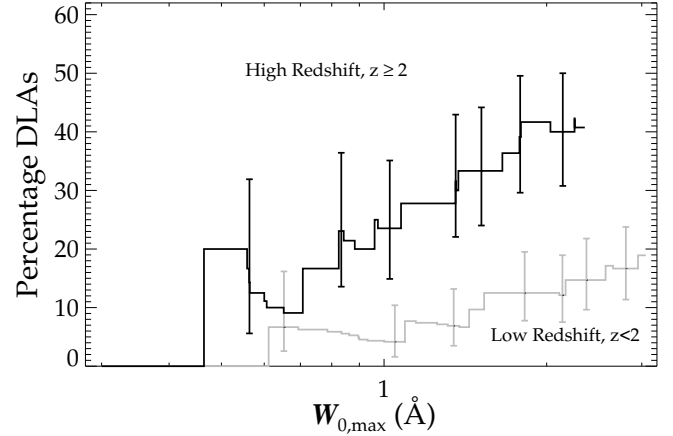


Figure 9. Percentage of Mg II absorbers with strengths in the range $0.3 \text{ \AA} \leq W_0^{\lambda 2796} \leq W_{0,\text{max}}$ associated with DLAs for the low ($z < 2$; light gray) and high ($z \geq 2$; black) redshift samples described in Section 3.3.3 (with a few representative error bars overplotted). The DLA percentage at large $W_0^{\lambda 2796}$ is significantly higher for the high redshift sample ($40.7^{+9.8}_{-9.2}\%$) than for the low redshift sample ($16.7^{+7.1}_{-5.3}\%$).

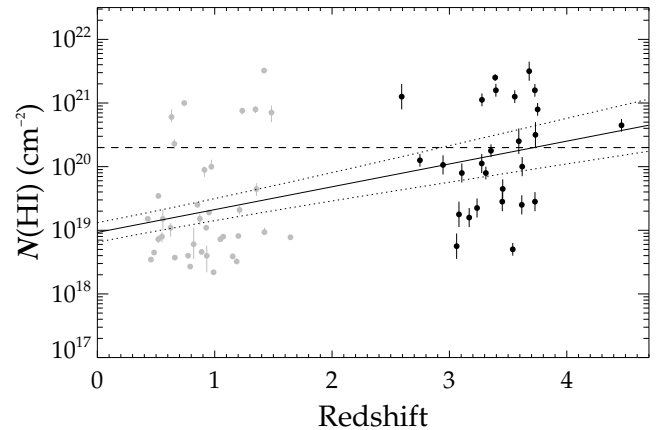


Figure 10. $N(\text{H I})$ column density as a function of absorber redshift for Mg II-selected systems for the *HST* sample (light gray) and high redshift FIRE sample (black) described in Section 3.3.3. The horizontal dashed line is at the damped Ly α cutoff, $N(\text{H I}) = 2e20 \text{ cm}^{-2}$. The higher redshift sample contains higher H I column densities and more DLAs, consistent with the results of Figures 8 and 9. The solid line is the sigma-clipped linear fit $\log N(\text{H I}) = (0.359 \pm 0.081)z + (18.966 \pm 0.153) \text{ cm}^{-2}$. The dotted lines are the one sigma limits.

ple ($0.36 < z < 2$; dark gray lines). Table 14 lists the sample median for each ratio considered. For H I, $W_0^{\lambda 1215}/W_0^{\lambda 2796}$ values derived from the *HST* sample of Section 3.3.3 (using a curve of growth analysis with $b = 30 \text{ km s}^{-1}$) are substituted for the SDSS DR7 sample (which contains no $W_0^{\lambda 1215}$ measurements). For each transition, we performed two-sample tests to assess the probability that the low and high redshift CDFs derive from a common parent population. We used three separate tests, which each account for upper limits, to generate these probabilities (stored in Table 14): the logrank P_{LR} , Gehan P_G , and Peto-Prentice P_{PP} tests.

Figure 12 and Table 15 provide the analogous CDFs, median ratios, and two-sample test results with three redshift bins instead of two. In Figure 12, the low and

high redshift samples (now at $0 < z < 1.5$ and $z \geq 3$) are still drawn in light gray and black, respectively, with a new mid-range redshift sample ($1.5 \leq z < 3$) depicted in dark gray. (No SDSS data are included in this plot). In Table 15, the L , M , and H subscripts on the two-sample probabilities denote which two of the low, mid-range, and high redshift samples were used in the calculation.

The H I equivalent width distributions confirm the trend seen in Figure 8, that the high redshift systems have markedly more neutral hydrogen for a given Mg II absorption strength. The mean ratio $W_0^{\lambda 1215}/W_0^{\lambda 2796}$ increases from 2.82 in the low redshift sample to 8.86 at high redshift. All three two-sample tests yield a $< 1\%$ probability that the low and high redshift distributions are alike. Figure 13, a scatter plot of $W_0^{\lambda 1215}/W_0^{\lambda 2796}$ versus redshift for the representative low and high redshift samples, highlights this evolution. The solid line is the robust linear fit $W_0^{\lambda 1215}/W_0^{\lambda 2796} = (2.783 \pm 0.706)z + (1.980 \pm 1.434)$. The dotted lines are one sigma limits.

For heavy element transitions, however, the difference between the high and low redshift samples is much less pronounced. For the singly ionized species in particular (see C II, Al II, Si II) the CDFs are nearly indistinguishable, and the two-sample tests often produce high probabilities of a draw from the same parent population ($> 50-95\%$) and never produce low $< 10\%$ probabilities. The median values of Al II and Si II only vary by 0.01-0.03 in ratio. Those of C II vary by slightly more (0.08), but this ion suffers from considerably fewer counts.

For Fe II, the samples are also very similar, though the exact degree depends on the multiplet transition used. The 1608, 2344, 2382, and 2600Å lines show no statistically significant difference between low and high redshift, while the 2374 and 2586 appear statistically smaller (by 0.05-0.1 in ratio) at high redshift. The latter two lines show a $\lesssim 5\%$ chance of deriving from the same parent population at high $z \geq 2$ and low $z < 2$ redshifts.

Although not directly testable at our data's resolution, this difference could naturally arise from a combination of line saturation and small number counts. Saturation would affect the 2344, 2382, and 2600Å transitions because of their large oscillator strengths, so even a substantial change in $N(\text{Fe II})$ would yield little change in equivalent width, particularly if the velocity spread is similar to that of Mg II (which we normalize out by taking the equivalent width ratio). The lower oscillator strengths of the 2374 and 2586 lines may leave them unsaturated, increasing their sensitivity to evolution. The 1608Å line does not fit into this story as its oscillator strength is also low, but our statistics on this transition are relatively poor compared to the redder transitions, so the significance is less strong.

In contrast to the singly ionized species, C IV, Si IV and especially Al III do appear to evolve, in the sense that the highly ionized lines are weaker toward high redshift. For a given $W_0^{\lambda 2796}$, the median Al III line ratio $W_0^{\lambda 1854}/W_0^{\lambda 2796}$ decreases from 0.18 at low redshift to 0.04 at high redshift for the two bin samples. All three two-sample distribution tests suggest a very small $\lesssim 0.1\%$ probability of no evolution between the highest redshift set and the other two.

Likewise the C IV ratio is reduced toward higher red-

shift, with the 1550Å component showing a more statistically significant change (again, possibly a saturation effect) and low $\lesssim 10\%$ probabilities are being drawn from the same distribution. This C IV evolution is most pronounced when dividing the sample into three redshift bins. With these divisions, we find very high 40 – 60% probabilities that the C IV 1550 mid and high redshift distributions are the same, suggesting that the most significant changes occur at $z < 1.5$.

Among the multiply ionized species, Si IV alone seems not to evolve: the two-sample tests yield probabilities of $\sim 35 - 65\%$ that the high and low redshift samples are drawn from the same distribution, although this could be a result of low counts.

Finally, the $W_0^{\lambda 2852}/W_0^{\lambda 2796}$ ratio between Mg I and Mg II decreases in a statistically significant manner as redshift increases for the two redshift sample scenario, with all three two-sample distribution tests giving a $\lesssim 0.1\%$ probability that the ratios are drawn from the same distribution. The SDSS DR7 sample confirms the low redshift sample's relative strength in Mg I absorption. The CDFs and analogous two-sample tests with three redshift bins suggest that the strongest evolution occurred before $z = 3$. The downward evolution in Mg I is slightly surprising given the basically unchanging nature of the other low-ionization lines.

4.3. Chemical Composition in Weak and Strong Mg II-selected Systems

Figure 14 gives the Kaplan-Meier derived CDFs for various ions relative to Mg II, but now divided into two samples by $W_0^{\lambda 2796}$ rather than redshift. The light gray line represents weak systems ($0.3\text{Å} \leq W_0^{\lambda 2796} \leq 1.0\text{Å}$), while the black line represents strong systems ($W_0^{\lambda 2796} > 1.0\text{Å}$). Table 16 provides the median ratios and logrank P_{LR} , Gehan P_G , and Peto-Prentice P_{PP} two-sample test probabilities for each ion. Figure 15 and Table 17 provide the analogous information as Figure 14 and Table 16, respectively, but now with the weak and strong absorber classes further divided by redshift as well. In Figure 15, the dotted and solid lines represent weak and strong absorbers, respectively, and the light gray and black lines represent low ($z < 2$) and high ($z \geq 2$) redshifts, respectively.

One noticeable feature is that the Ly α CDF appears identical for the strong and weak Mg II samples: The median ratio of $W_0^{\lambda 1215}/W_0^{\lambda 2796}$ is higher for the weak Mg II absorbers (6.89 vs. 5.44), but the two-sample tests find any differences to be statistically insignificant. Moreover, Figure 15 shows that both weak and strong Mg II systems evolve very similarly (both strongly) with redshift.

In contrast to H I, the two-sample tests all suggest a very small probability ($\lesssim 5\%$) that Mg I 2852 absorption is the same between weak and strong Mg II systems, with a tendency towards more relative amounts of Mg I in stronger Mg II systems as expected. The other low ionization species' (C II, Fe II, Si II, and Al II) ratios display much greater similarity between weak and strong Mg II systems, and none of their CDFs show significant qualitative differences. Although some of these distributions possess statistically significant differences (e.g., Fe II 2600, which has probabilities $\lesssim 1\%$ of having ratios

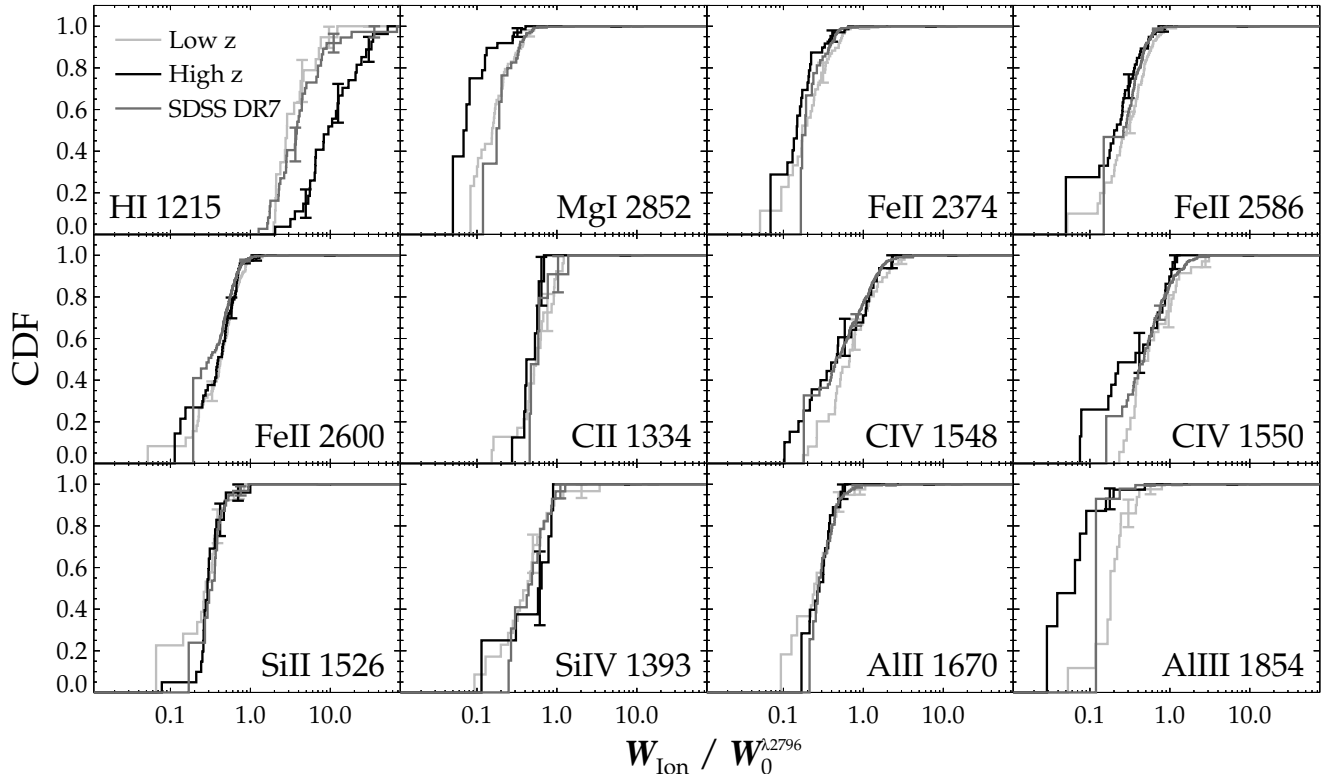


Figure 11. Kaplan-Meier cumulative distribution functions for the ratios of the rest equivalent widths of various ions with $W_0^{\lambda 2796}$ for the low redshift ($0 < z < 2$; light gray), high redshift ($z \geq 2$; black), and SDSS DR7 ($0.36 < z < 2$; dark gray) samples described in Section 3.3.1. For H I 1215, the *HST* sample from Section 3.3.3 (with $W_0^{\lambda 1215}$ from a curve of growth analysis with $b = 30 \text{ km s}^{-1}$) is used in place of the SDSS sample (which contains no $W_0^{\lambda 1215}$ measurements). Detailed statistics associated with this figure and the sub-samples are given in Tables 10 and 14. A few representative error bars have been overplotted. While the CDFs for a few of the ions (Mg I, Al III. . .) show signs of evolution, only the ratio of $W_0^{\lambda 1215}/W_0^{\lambda 2796}$ shows clear signs of strong evolution.

with weak and strong absorbers drawn from the same distribution), the evolution detected even in these cases is quite weak.

The higher ionization lines C IV and Si IV, however, decrease significantly in strength as $W_0^{\lambda 2796}$ increases (0.97 to 0.29 for C IV 1548, for example). The two-sample tests suggest a very small probability that these samples are drawn from the same distributions for weak and strong absorbers ($\lesssim 3\%$). This may result from H I-shielding, since the strong absorbers have larger *absolute* amounts of H I, even though their relative amounts are nearly identical. The strong Mg II systems have low $\lesssim 4\%$ two-sample probabilities that their low and high redshift subsets have $W_0^{\lambda 1548}/W_0^{\lambda 2796}$ and $W_0^{\lambda 1550}/W_0^{\lambda 2796}$ ratios drawn from the same distribution, while the weak Mg II systems have high $\sim 30 - 75\%$ probabilities of no redshift evolution. Interestingly, the Si IV distributions hint at the reverse, although the evidence for redshift evolution for the weak absorbers is not statistically strong. Not much may be deduced from the Al III distributions since this ion suffers from small counts among weak Mg II systems.

4.4. Metallicity of Mg II-selected Systems at High Redshift

Figure 16 gives the Fe, C, Si, and Al metallicities for the Mg II-selected high redshift FIRE sample (black points) and the general high redshift Prochaska et al. (2007) metallicity subsample from Section 3.3.4 (gray

points). Triangular points for the FIRE data denote weak Mg II absorbers ($0.3\text{\AA} \leq W_0^{\lambda 2796} \leq 1.0\text{\AA}$) and the diamonds denote strong absorbers ($W_0^{\lambda 2796} > 1.0\text{\AA}$). Table 4 provides these metallicity measurements for the FIRE systems.

As previously stated, we have employed very conservative criteria for flagging saturated lines in our moderate resolution spectra. This explains why the black points are mostly lower limits in these metallicity measurements. Indeed all of the measurements made for DLAs (which may be directly compared to Prochaska et al. 2007) are lower limits. Despite this, the data still establish that Mg II-selected systems are not metal poor with respect to the general DLA population. (The possibility that Mg II absorbers are actually probing the full, underlying DLA population is addressed later in the Discussion, Section 5.2.)

In fact, the limits imply quite high abundances of 0.1 Solar or more for weak Mg II systems, which are predominantly optically thick sub-DLA absorbers as viewed in H I. Some caution is warranted for these points since we have not included ionization corrections. Detailed study of the ionization in $z \sim 3$ sub-DLAs by Péroux et al. (2007) suggests that such ionization corrections generally decrease the resulting metallicity. The magnitude of the effect depends on $N(\text{H I})$, with systems at $\log N(\text{H I}) \sim 19 \text{ cm}^{-2}$ requiring a ~ 0.3 dex correction, and stronger systems requiring less until the DLA

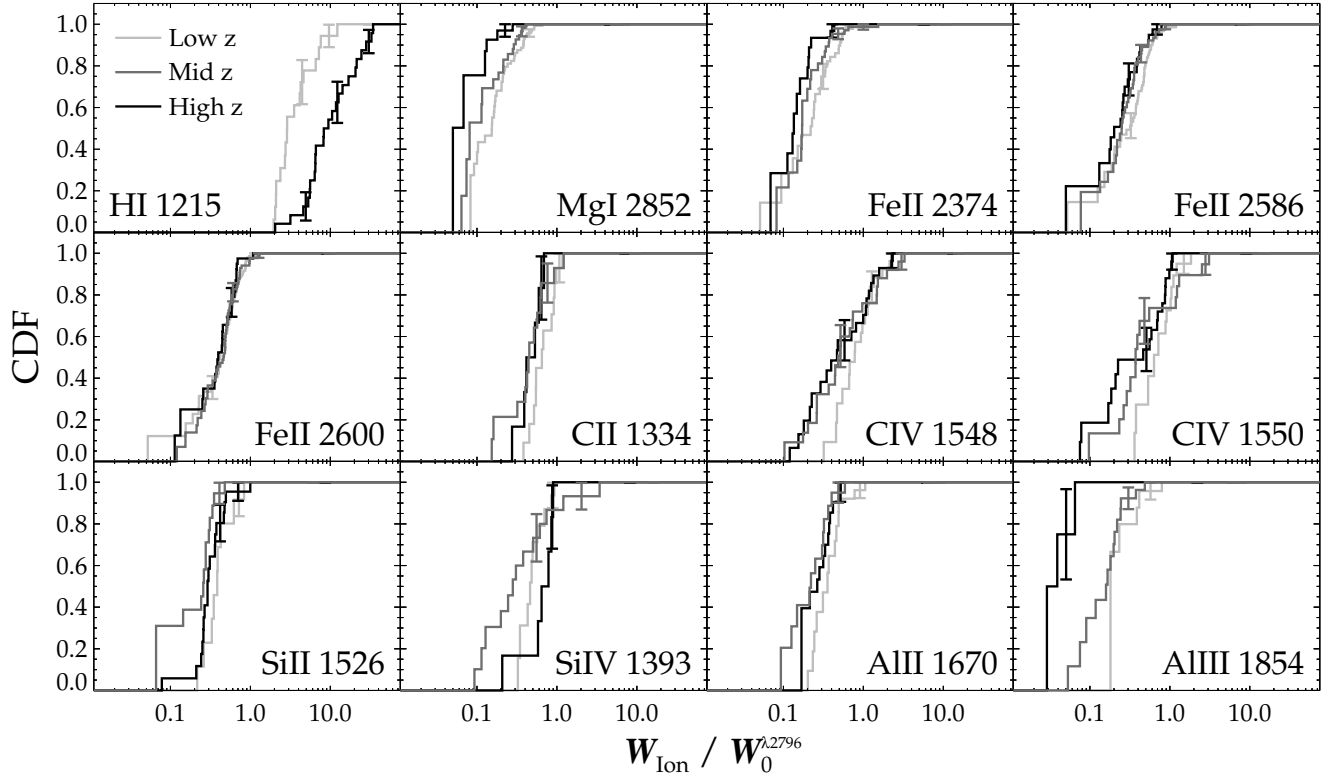


Figure 12. Analogous plot to Figure 11, but for the three redshift-binned low redshift ($0 < z \leq 1.5$; light gray), medium redshift ($1.5 \leq z < 3$; dark gray) and high redshift ($z \geq 3$; black) samples described in Section 3.3.1. (The medium redshift sample contained only a few $W_0^{\lambda 1215}$ measurements and is excluded from that panel). Detailed statistics associated with this figure and the sub-samples are given in Tables 11 and 15. A few representative error bars have been overlotted. The evolution of C IV appears strongest at $z < 1.5$.

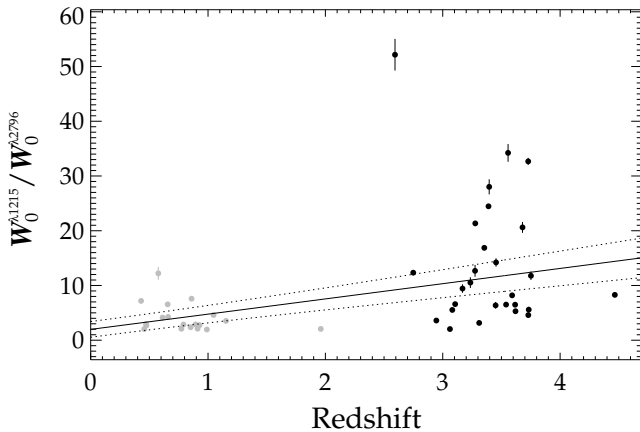


Figure 13. Relative absorption strength $W_0^{\lambda 1215}/W_0^{\lambda 2796}$ as a function of absorber redshift for the low redshift (light gray) and high redshift (black) samples described in Section 3.3.1. The higher redshift sample contains more H I absorption relative to Mg II, consistent with the results of Figure 11. The solid line is the robust linear fit $W_0^{\lambda 1215}/W_0^{\lambda 2796} = (2.783 \pm 0.706)z + (1.980 \pm 1.434)$. The dotted lines are the one sigma limits.

threshold is reached. Still, these limits would still fall near 10% solar for many of the Mg II sub-DLAs, which (like most sub-DLAs) appear to be much more metal rich than the IGM and may in fact be more enriched than classical DLAs.

5. DISCUSSION

5.1. Taxonomy and Evolution of Classes

Numerous studies in the literature have proposed that Mg II traces multiple physical environments. These are variously based on differential evolution in dN/dX (Paper I), statistical studies of Mg II host galaxy color (Zibetti et al. 2007; Lundgren et al. 2009), galaxy-Mg II clustering analysis (Bouché et al. 2006; Gauthier et al. 2009; Nestor et al. 2011), and studies of galaxy-absorber projected inclination (Bordoloi et al. 2011; Kacprzak et al. 2011). Some of these studies suggest that stronger Mg II systems are found near star forming galaxies and may be related to outflows. Indeed, models deriving strong $W_0^{\lambda 2796} > 1 \text{ \AA}$ absorption from star-forming disks and their associated outflowing interstellar material (e.g., Chelouche & Bowen 2010) show better agreement with the empirically measured $z > 2.5$ dN/dX than halo occupation models (e.g., Tinker & Chen 2010). However the connection between strong Mg II absorption and star formation is not universally found, and the use of $W_0^{\lambda 2796}$ alone to distinguish outflowing from accreting Mg II absorbers is almost certainly an oversimplification.

This motivates us to explore other schemes for classifying Mg II absorbers, since we have access to numerous high- and low-ionization transitions. We have adopted the methodology of Churchill et al. (2000b), who developed a classification taxonomy for Mg II absorbers based on a multivariate clustering analysis for Mg II systems at $z = 0.4 - 1.4$. The analysis incorporates measurements of equivalent width for Mg II, H I, Fe II, and C IV, as well as the kinematic spread for Mg II (denoted $\omega_{\lambda 2796}$).

Churchill et al. (2000b) contains details of the method-

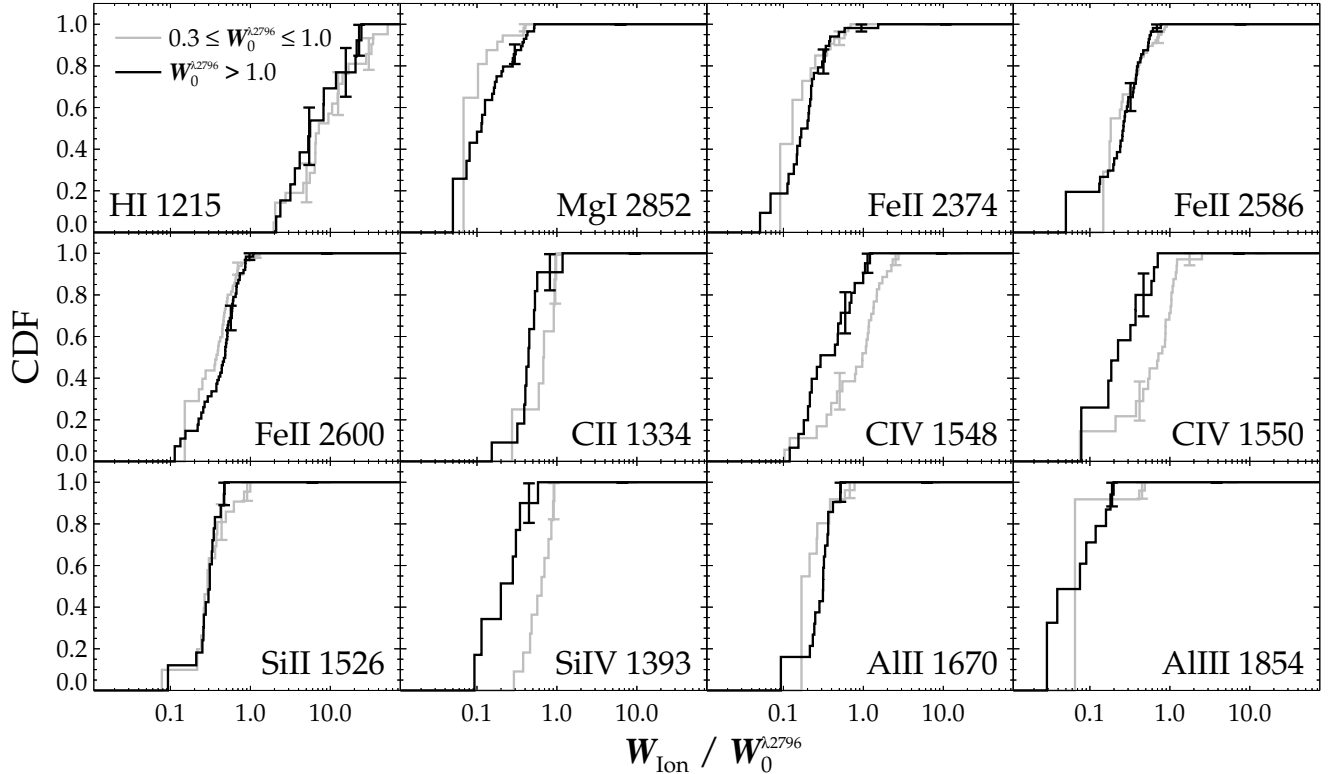


Figure 14. Analogous plot to Figure 11, but for the weak ($0.3 \leq W_0^{\lambda 2796} \leq 1.0$; light gray) and strong ($W_0^{\lambda 2796} > 1.0$; black) Mg II absorption samples described in Section 3.3.2. Detailed statistics associated with this figure and the sub-samples are given in Tables 12 and 16. A few representative error bars have been overplotted. The samples appear to contain the same amount of H I *relative to* Mg II, but the strong absorbers contain less C IV and Si IV, perhaps because of their larger absolute amounts of H I shielding these ions.

ology. Briefly, one must first “standardize” the distributions for these five properties into an $N(0,1)$ Gaussian form, and then implement a K -means clustering algorithm that moves systems between clusters until the variability within clusters is minimized and across clusters is maximized. The 45 Mg II systems grouped in this way segregated into five statistically distinct classes.

Churchill et al. (2000b) named the five classes as follows:

1. *classic systems* (24%), which have $W_0^{\lambda 2796}$, $W_0^{\lambda 2600}$, $W_0^{\lambda 1548}$, $W_0^{\lambda 1215}$, and $\omega_{\lambda 2796}$ within 0.5σ of the overall normalized sample mean.
2. *C IV-deficient systems* (18%), which are otherwise identical to classic systems but have significantly less $W_0^{\lambda 1548}$: the mean in standardized units is more than 1.5 less.
3. *DLA/H I-rich systems* (13%), which have stronger $W_0^{\lambda 2796}$ and much stronger $W_0^{\lambda 2600}$ and $W_0^{\lambda 1215}$ than classic systems, but similar $\omega_{\lambda 2796}$ and weaker $W_0^{\lambda 1548}$.
4. *double systems* (7%), which have larger equivalent width and velocity spread than classic systems, including much stronger ($> 2\times$) $W_0^{\lambda 2796}$, $W_0^{\lambda 1548}$, and $\omega_{\lambda 2796}$. The naming convention for this class was inspired by the work of Bond et al. (2001), who identified such systems as double-troughed absorbers in HIRES spectra.

5. *single/weak systems* (38%), which are single component, narrow lines with the means of $W_0^{\lambda 2796}$ and $W_0^{\lambda 1548}$ in standardized units weaker by ~ 1 compared to classic systems.

For reasons of completeness in the FIRE sample, we limit our discussion to systems with $W_0^{\lambda 2796} > 0.3\text{\AA}$, effectively eliminating the single/weak systems from consideration. This leaves four classification bins for the high redshift systems.

We first explored direct application of Churchill’s method using the low redshift standardization parameters, to see how the population evolves relative to an absolute benchmark. This exercise was less illuminating than anticipated: the typical system at high redshift has slightly weaker Mg II (see Figure 15 in Paper I regarding the evolution of the typical system size W_*), which would imply a classic or weak classification, but Figure 8 shows that $N(\text{H I})$ in the corresponding absorbers is higher, suggesting a DLA or double classification. In other words, the high redshift systems would require a separate class altogether which possesses less heavy elements than the low redshift classes, but contains more H I absorption.

Next, we attempted a new classification where each absorber was standardized to the properties of the typical system at its respective redshift. This requires a slightly different interpretation but produces a more well-defined taxonomy.

We produced standardization distributions for three redshift bins ($z < 3$, $3 \leq z < 4$, and $z \geq 4$), using

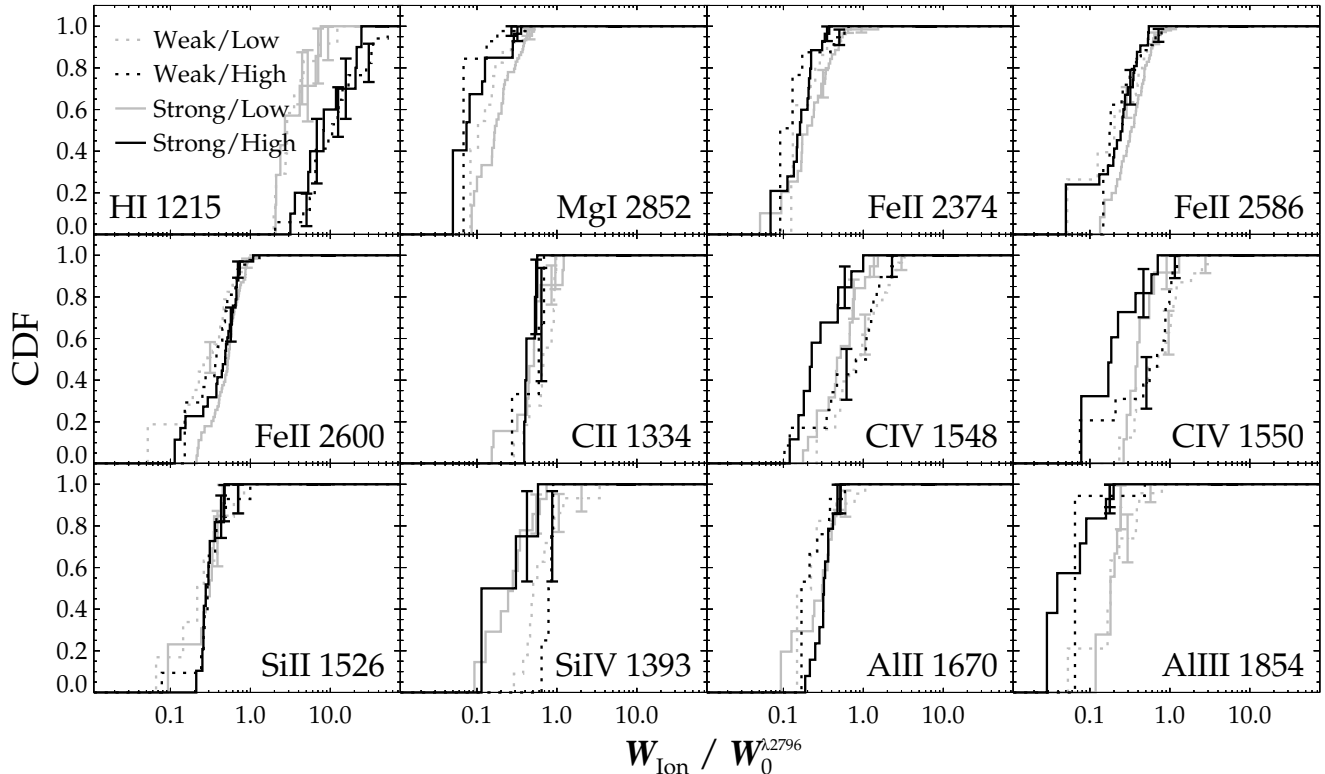


Figure 15. Analogous plot to Figure 15, but with the weak ($0.3 \leq W_0^{\lambda 2796} \leq 1.0$; dotted lines) and strong ($W_0^{\lambda 2796} > 1.0$; solid lines) Mg II absorption samples divided into low ($z < 2$; gray lines) and high ($z \geq 2$; black lines) redshift parts as well. Detailed statistics associated with this figure and the sub-samples are given in Tables 13 and 17. A few representative error bars have been overplotted. The distribution of $W_0^{\lambda 1215}/W_0^{\lambda 2796}$ appears the same between the weak and strong samples for both the low and high redshift cuts.

the high redshift sample of Section 3.3.1. The actual standardization, which maps the observed CDF onto a standard normal distribution, is accomplished using

$$y_i = \begin{cases} -\sqrt{2}\text{erfc}^{-1}(P(x_i)) & P(x_i) \leq 0.5 \\ \sqrt{2}\text{erf}^{-1}(2P(x_i) - 1) & P(x_i) > 0.5, \end{cases} \quad (1)$$

where x_i is the original absorption value, y_i is the standardized value, $P(x)$ is the CDF, $\text{erf}^{-1}(x)$ and $\text{erfc}^{-1}(x)$ are the inverse error and complementary error functions, and the index i indicates each system considered. This exercise is repeated for each redshift bin and absorption property used for classification. Since our highest redshift bin ($z \geq 4$) contains only one measured value for $W_0^{\lambda 1215}$, we pooled the $W_0^{\lambda 1215}$ values from the two largest redshift bins when calculating their $W_0^{\lambda 1215}$ CDFs.

A full treatment would then require re-calculation of the K -means clustering algorithm and generation of new classes for each redshift bin. But this is not practical for the high redshift sample because for many systems we can only measure 2 or 3 of the 5 classification observables. This is partly a consequence of the QSO sightline selection for the FIRE survey, for which we prioritized high redshift objects to maximize pathlength and Mg II sample size, thereby minimizing dN/dX errors at $z > 3$. While accomplishing these goals, the FIRE sample is not ideally suited for a $z > 2$ classification analysis. In particular, by choosing QSOs at high emission redshift one increases the likelihood that C IV and H I measurements at $z \sim 2 - 2.5$ will be lost due to absorption from the

Ly α forest and/or higher redshift Lyman limit systems. In practice, the lowest redshift for which we have $W_0^{\lambda 1548}$ and $W_0^{\lambda 1215}$ measurements in the FIRE statistical sample are $z = 2.749$ and $z = 2.593$, respectively. The ideal classification sample would have contained more background objects at $z_{QSO} = 2.5 - 3$ to avoid this paucity of $W_0^{\lambda 1548}$ and $W_0^{\lambda 1215}$ measurements at intermediate redshift. Because of these short comings, we therefore focus on determining which of Churchill’s existing classes best represents the measured properties of each absorber, in a quantitative sense, instead of running K -means clustering tests from scratch.

To this end, we calculated a matching “score” that rates how well each class represents a particular system, with low scores indicating higher quality matches. The score for a given class is the sum of the squared (standardized) deviation between the absorber in question and zero (the standardized mean, by construction) for each parameter’s distribution—qualitatively similar to a χ^2 .

We assigned each system to the class that minimized its match score. In many cases, we measured only a subset of the nominal five classification observables. Since we are calculating a “best” match for each system rather than an absolute match, we simply excluded those properties from that system’s score sum. In many cases this led to a classification degeneracy, particularly between classic and C IV-deficient systems where no C IV measurement was available (as was commonly the case; without C IV these classes are otherwise indistinguishable, see Churchill’s Figure 3). Where appropriate we used

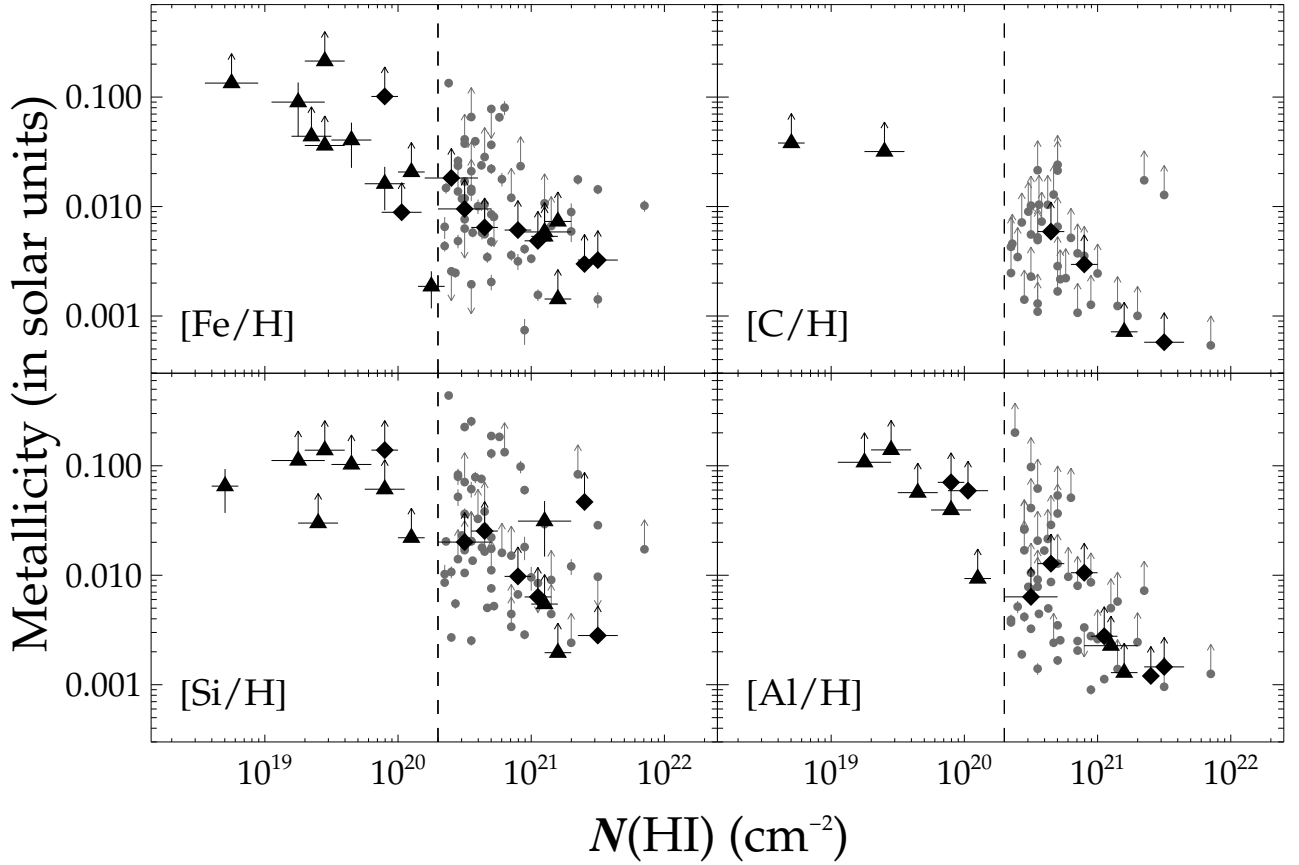


Figure 16. Metallicities (relative to solar) for the Mg II-selected (black) and non-Mg II-selected (light gray) high redshift samples ($z \geq 2$) described in Section 3.3.4. For Mg II-selected systems, weak Mg II absorbers ($0.3\text{\AA} \leq W_0^{\lambda 2796} \leq 1.0\text{\AA}$) are shown as triangles and strong ($W_0^{\lambda 2796} > 1.0\text{\AA}$) as diamonds. The dashed vertical line is at the DLA cut, $N(\text{H I}) = 2e20 \text{ cm}^{-2}$. All metallicities for Mg II-selected DLA systems are lower limits, making comparison difficult, but the Mg II-selected systems are not metal-poor compared to the general population of absorbers at these redshifts. No ionization corrections have been applied, potentially leading to overestimates of up to ~ 0.3 dex for the lower $N(\text{H I})$ systems’ metallicities in this plot (Péroux et al. 2007). Even with this correction, the lower limits of the lower $N(\text{H I})$ systems approach a tenth of solar.

C IV upper limits to break the degeneracy but in many cases we could only determine that the system belonged to one of these two classes.

One complication is that unlike here, Churchill et al. (2000b) included $W_0^{\lambda 2796} \ll 0.3\text{\AA}$ systems in their original standardization procedure. This reduces the zero point of the standardized distribution, which in turn increases the renormalized y_i value for each system above 0.3\AA .

To compensate for this effect, we re-calculated the standardized means for each absorption property and each class in the Churchill et al. (2000b) sample. Because our literature sample contained Churchill’s data, we could perform this both with and without a $W_0^{\lambda 2796} < 0.3\text{\AA}$ cut applied. For each parameter we then measured the offset between means of the cut and full low-redshift sample. Then, when classifying each high-redshift absorber we applied the same offsets in reverse, to capture in a rough sense the effect of missing systems below 0.3\AA .

Obviously this crude classification procedure does not account for the possibility that the classes themselves evolve differently in redshift, which would manifest as the mean standardized values changing in redshift. Our only aim is to provide an objective method for classifying

Mg II absorption systems that is robust to missing measurements and allows for a first-look study of taxonomy and evolution of various groupings.

Table 2 lists classifications for each system in the FIRE sample. If we combine the classic and C IV-deficient classes (because many FIRE systems have no $W_0^{\lambda 1548}$ measurements), we are left with three classes: classic+C IV-deficient, DLA/H I-rich, and double systems. The fraction of $W_0^{\lambda 2796} \geq 0.3\text{\AA}$ systems falling into each of these three categories is roughly similar at high and low redshift (Figure 17). Although the small number of systems suggests against reading too much into this agreement, the similarity hints that if these classes result from disparate physical mechanisms, then the fraction of intersected systems caused by these various mechanisms has not dramatically evolved over the large redshift range probed.

We next derived linear densities dN/dX for each absorber class in isolation. We did not attempt to adjust the error bars for misclassifications, which surely exist in non-negligible numbers since many systems have only two or three of the five absorption properties measured. We will discuss the ramifications of misclassification in more detail below.

Figure 18 illustrates dN/dX for $0.3\text{\AA} \leq W_0^{\lambda 2796} <$

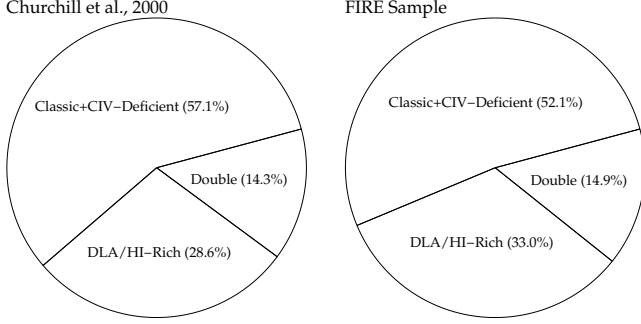


Figure 17. Percentage classification breakdowns for $W_0^{\lambda 2796} > 0.3 \text{ \AA}$ systems for both the low redshift ($0.4 < z < 1.4$) sample of Churchill et al. (2000b, 21 systems) and the high redshift ($z > 2$) FIRE sample (94 systems). The percentage cuts are remarkably similar given that the universe is in vastly different states in the two epochs, separated by ~ 4.8 Gyr.

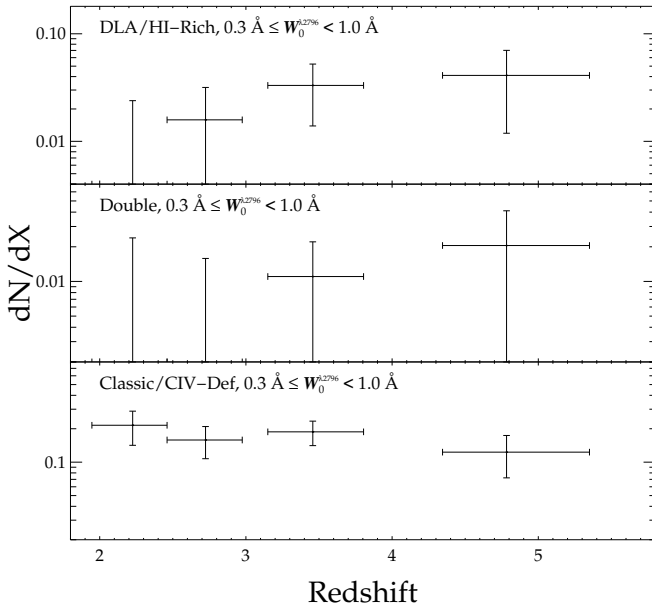


Figure 18. The linear density evolution of $0.3 \text{ \AA} \leq W_0^{\lambda 2796} < 1.0 \text{ \AA}$ systems for the DLA/H i-rich, double, and classic+C iv-deficient classes of absorbers defined in Churchill et al. (2000b). Classification depends upon $W_0^{\lambda 2796}$, $W_0^{\lambda 1215}$, $W_0^{\lambda 1548}$, $W_0^{\lambda 2600}$ and $\omega_{\lambda 2796}$, and is determined using the procedure of Section 5.1. An overwhelming majority (84.2%) of the systems in this $W_0^{\lambda 2796}$ range fall into the classic+C iv-deficient categories because of relatively weak Mg II absorption and low kinematic spreads. The DLA/H i-rich linear density slightly increases with redshift, perhaps a result of the rise of the overall DLA population with redshift (Figure 21), the increase in $W_0^{\lambda 1215}/W_0^{\lambda 2796}$ (Figure 11) leading to more DLAs becoming associated with $W_0^{\lambda 2796} \lesssim 1.0 \text{ \AA}$ systems, or both.

1.0 \AA systems, divided by classification. A large majority of systems in this $W_0^{\lambda 2796}$ range (84.2%) are classic+C iv-deficient. This is expected since the classification process considers $W_0^{\lambda 2796}$ and preferentially assigns strong systems as doubles or DLAH i-rich systems. But the classic+C iv-deficient set also includes many larger $W_0^{\lambda 2796}$ systems (including 11 with $W_0^{\lambda 2796} > 0.8 \text{ \AA}$) that have $W_0^{\lambda 2796}$ typical of double and DLAH i-rich systems, but were instead classified as classics on the basis of their small kinematic spreads. Since the overall population of absorbers of this strength shows no statistically sig-

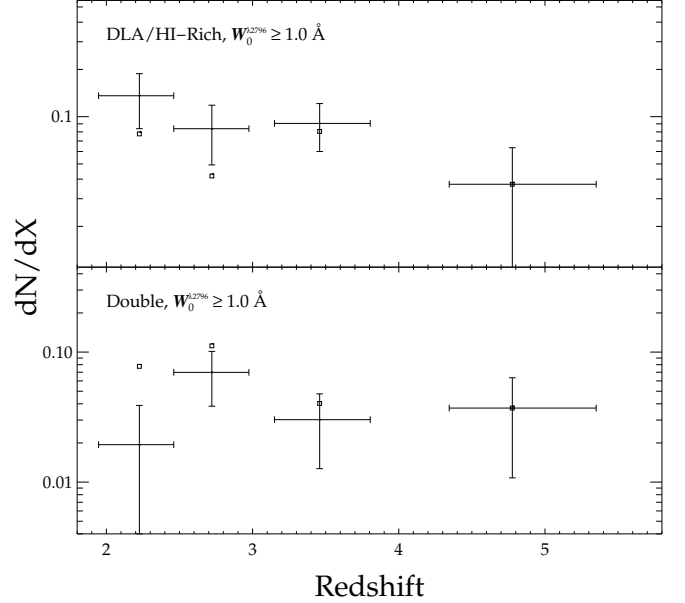


Figure 19. The linear density evolution of $W_0^{\lambda 2796} \geq 1.0 \text{ \AA}$ systems for the DLA/H i-rich and double classes of absorbers defined in Churchill et al. (2000b). The DLA/H i-rich linear density appears relatively constant until $z \sim 3.5$ before decreasing in the final bin. The double linear density rises by a factor of 3–4 from $z = 2$ to 3, and decreases until $z \sim 3.5$. The square points are at the new locations of dN/dX if the 8 $W_0^{\lambda 2796} > 2.75 \text{ \AA}$ systems are re-classified from DLA/H i-rich systems to double systems. This subset of absorbers, for which we do not have $W_0^{\lambda 1215}$ measurements, possesses both unusually large $W_0^{\lambda 2600}$ ($W_0^{\lambda 2600} = 2.26 \text{ \AA}$) and $\omega_{\lambda 2796}$ ($\omega_{2796} = 128.3 \text{ km s}^{-1}$). It is unclear whether they belong in the DLA/H i-rich class or double class, or whether they constitute an entirely new class of absorber associated with physical processes not prevalent at the low $z < 1.4$ redshift universe studied in Churchill et al. (2000b).

nificant evidence for evolution from $z \sim 0.4$ to $z \sim 5$ (Paper I) and most of these absorbers are classic+C iv-deficient, it is not surprising that the Mg II frequency for this combined class (bottom panel) also does not significantly evolve. Disentangling these two classes to determine their differential evolution requires more data containing a greater number of $W_0^{\lambda 1548}$ measurements.

The low incidence of Mg II-weak double systems (3) and high misclassification probability limit the conclusions we may draw about their evolution in this range (middle panel). Likewise the paucity of DLA systems in this range (6) merits caution, although it is interesting to speculate on the increase in dN/dX towards large redshift given that both the DLA linear density, most (if not all) of which appears to be associated with Mg II systems (as discussed later in Section 5.2), increases over this redshift range (Prochaska & Wolfe 2009), and the typical $W_0^{\lambda 1215}$ associated with a given $W_0^{\lambda 2796}$ increases with redshift (Figure 13). In particular, it would be interesting to know whether this increase with redshift outpaces that of the overall rise, such that a higher fraction of DLA systems are associated with smaller $W_0^{\lambda 2796} \lesssim 1 \text{ \AA}$ Mg II systems at high redshift. Substantially more data would be required to study this question in detail.

Figure 19 shows dN/dX for the stronger $W_0^{\lambda 2796} \geq 1.0 \text{ \AA}$ systems. Only one classic+C iv-deficient system falls in this range, so we excluded this class from the

figure. Apparently for absorbers with strong $W_0^{\lambda 2796}$ the frequency of DLA/H I-rich systems falls from $z = 2$ to 5. The full $W_0^{\lambda 2796} \geq 0.3\text{\AA}$ DLA/H I-rich dN/dX remains essentially constant over this redshift range.

In contrast, the Mg II frequency of double systems appears to increase by a factor of $\sim 3 - 4$ from $z = 2.2$ to 2.7 before falling until $z \sim 3.5$. Given both empirical evidence connecting large Mg II absorption to star formation and observations showing the star formation rate density rising until $z = 2 - 3$ and falling afterward (Bouwens et al. 2010, 2011), it is tempting to associate double systems with star formation based upon their dN/dX here. But without dN/dX data for doubles at low $z < 2$ redshifts it is unknown whether the frequency of doubles continues to fall as the SFR density falls towards $z \rightarrow 0$. Moreover the large error bars again indicate limitations of our sample size, such that these evolutionary trends are mostly suggestive and cannot yet be considered robust.

For example, systems in the lowest redshift bin for these plots contain no $W_0^{\lambda 1215}$ or $W_0^{\lambda 1548}$ measurements. As a result, this bin is particularly prone to misclassification since $W_0^{\lambda 1215}$ in particular is an important diagnostic. Some systems labeled as DLA/H I-rich in this bin are therefore marginal classifications based upon extremely strong Fe II absorption, but they also exhibited large kinematic spreads typical of doubles.

In fact all but one of the 8 $W_0^{\lambda 2796} \geq 2.75\text{\AA}$ systems in the FIRE sample (not just those in the lowest redshift bin) were classified as DLA/H I-rich systems based on their strong Fe II absorption ($\bar{W}_0^{\lambda 2600} = 2.26\text{\AA}$), but we have no $W_0^{\lambda 1215}$ measurements for any of these systems, and all of them have unusually large kinematic spreads ($\bar{\omega}_{\lambda 2796} = 128.3\text{ km s}^{-1}$). It may be that all of these are actually doubles, and the double class as a whole has evolved between lower redshifts and this epoch. Figure 20, which depicts the Mg II and Fe II kinematic spreads for all FIRE systems labeled as classic+C IV-deficient (light gray diamonds), DLA/H I-rich (dark gray circles), and doubles (black triangles), provides a case for reclassification: The large $W_0^{\lambda 2796}$ systems, depicted with open circles, occupy a region of $\omega_{\lambda 2796} - \omega_{\lambda 2600}$ space more heavily occupied by double systems. The square points on Figure 19 represent dN/dX with the classifications of the $W_0^{\lambda 2796} \geq 2.75\text{\AA}$ systems changed to double.

5.2. Connection with DLAs

We showed in Section 4.1 that $40.7_{-9.2}^{+9.8}\%$ of $W_0^{\lambda 2796} > 0.3\text{\AA}$ systems at high redshift ($\bar{z} = 3.402$) are associated with DLAs. We can invert this question and consider what fraction of high redshift DLAs are associated with Mg II systems. Prochaska et al. (2005) provide dN/dX measurements for the general DLA population at redshifts $z = 1.7$ to 5.5, which are represented by the gray points in Figure 21. The black points represent dN/dX of Mg II-DLAs, calculated by multiplying total dN/dX for Mg II by the fraction of Mg II systems exhibiting DLAs in each bin. For the lowest Mg II-selected DLA redshift bin, we have no $N(\text{H I})$ measurements so we simply used the fraction for the next highest bin. This is reasonably justified since the fraction of DLAs in this $z = 2.4609 - 2.9750$ redshift bin (4/12) is very similar to the fraction for the representative subsample of

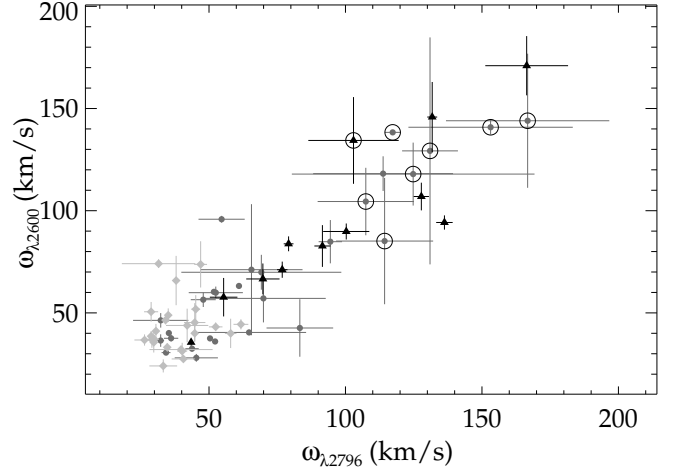


Figure 20. Mg II and Fe II kinematic spreads for the $W_0^{\lambda 2796} \geq 0.3\text{\AA}$ FIRE systems. The light gray diamonds, dark gray circles, and black triangles represent systems classified as classic+C IV-deficient, DLA/H I-rich, and double systems, respectively. The large $W_0^{\lambda 2796} \geq 2.75\text{\AA}$ systems (enclosed by larger black circles) dominate the upper right portion of the plot. The matching algorithm predominantly classified these systems as DLA/H I-rich because of strong $W_0^{\lambda 2600}$, but they also possess large $\omega_{\lambda 2796}$ and occupy a region of $\omega_{\lambda 2796} - \omega_{\lambda 2600}$ space more heavily occupied by double systems.

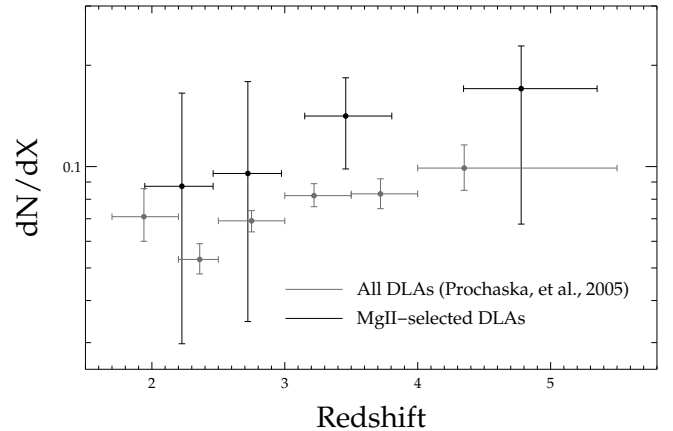


Figure 21. The linear densities dN/dX for the general high redshift DLA population (Prochaska et al. 2005, gray points) and the Mg II-selected DLA population (black points). We calculated the Mg II-selected DLA dN/dX by multiplying the $W_0^{\lambda 2796} > 0.3\text{\AA}$ dN/dX for the general Mg II population by the fraction of these systems with $N(\text{H I})$ measurements associated with DLAs in each bin. The first bin had no measurements, and used the fraction from the second. The largest redshift bin had only one $N(\text{H I})$ measurement (a DLA); the errors should be treated with caution. The plot suggests that an overwhelming majority, if not all, high redshift DLAs have corresponding Mg II absorption.

Rao et al. (2006) for $z = 1 - 1.5$ (4/13). The highest Mg II-selected bin has only one $N(\text{H I})$ measurement (a DLA), and is therefore very uncertain.

This exercise suggests that all (or nearly all) DLAs have accompanying $W_0^{\lambda 2796} > 0.3\text{\AA}$ Mg II absorption. This is to be expected since every observed $z > 2$ DLA exhibits low-ionization metal line absorption in rest-frame UV (Turnshek et al. 1989; Lu et al. 1993; Wolfe et al. 1993; Lu & Wolfe 1994). Moreover, Mg II absorption has been found in every high redshift

DLA for which it could have been observed (Wolfe et al. 2005). These statements are also true for low redshift $z < 2$ DLAs by construction, since most such DLAs were selected on the basis of strong Mg II and Fe II absorption (Rao et al. 2006). This result informs our interpretation of Figure 16 depicting gas-phase metallicities for the Mg II-selected (black) and H I-selected (light gray) absorption systems described in Section 3.3.4. In particular, the Mg II-selected metallicities for DLAs cannot be inconsistent with those of the general DLA population if these two groups are largely the same.

In the representative subsample at low redshifts ($\bar{z} = 0.927$) from Rao et al. (2006) described in Section 3.3.3, a smaller percentage of Mg II systems correspond to DLAs ($16.7_{-5.3}^{+7.1}\%$), and these systems are more commonly associated with Lyman limit systems and/or sub-DLAs.

It is noteworthy that numerous papers have associated Mg II systems—particularly the strong variety—with star formation and outflows (including in our Paper I), yet we find that this population overlaps very heavily with classical DLAs, which are generally not thought to result from outflows at all. Rather DLAs are often taken as building blocks of present day galaxies (Wolfe et al. 1993), either as the early progenitors of galactic disks (Prochaska & Wolfe 1997) or merging baryonic clumps embedded in dark matter haloes (Haehnelt et al. 1998; Pontzen et al. 2008).

The connection between strong Mg II absorption, winds (e.g., Zibetti et al. 2007; Rubin et al. 2010) and DLAs (e.g., Rao & Turnshek 2000) is particularly interesting because low redshift galaxy-absorber studies see $W_0^{\lambda 2796} > 0.3\text{\AA}$ absorption systems in extended haloes out to $D \sim 120h^{-1}$ kpc (Chen et al. 2010a), while Mg II-DLAs reside within $D \lesssim 15h^{-1}$ kpc (Steidel 1995) of their respective hosts. If the strong Mg II systems represent both winds *and* DLAs, then some fraction of the DLA population would reflect non-gravitational processes, and also the strong phase of Mg II-absorbing wind evolution would only fill the halo region nearest to the stellar disk. This picture may be incomplete since both dN/dX for the strong absorbers and empirically derived star formation rates fall from $z \sim 2 \rightarrow 6$ (Bouwens et al. 2010, 2011) while the DLA linear density increases until at least $z \sim 5.5$ (see Figure 21, or Prochaska et al. 2005). This suggests that there may be some Mg II-poor DLAs at $z > 5$; although such systems have not been identified, it may be an interesting area for further study.

One possible alternative is to invoke two populations of strong absorbers: one corresponding to classical DLAs, and one associated with star formation driven winds. This theory is inspired by the taxonomic classifications of Churchill et al. (2000b), and supported by Bond et al. (2001), who explore the possibility that strong, double-troughed Mg II absorbers trace winds. We see very faint evidence of evolution in our high redshift dN/dX for the double systems that is consistent with this interpretation, but cannot be considered proof on account of the small number statistics.

5.3. Chemical Evolution

Figure 11 illustrates how the relative abundance of H I at fixed $W_0^{\lambda 2796}$ increases toward higher redshift while the heavy elements lines remain largely unchanged.

One *might* interpret this as direct evidence of an increasing metallicity of Mg II systems toward the present day. However this picture is complicated by uncertainties in the degree of saturation in the metal lines. At $W_0^{\lambda 2796} = 0.3\text{\AA}$ and above one expects some degree of saturation, particularly for systems with small or unresolved kinematic spreads. This effect could in principle mask a decrease in the metal column densities that tracks the observed change in $N(\text{H I})$ from high to low redshifts.

We do estimate lower limits on the abundance directly for systems with measured H I, finding values consistent with the general DLA population, and even higher for lower $N(\text{H I})$, which correlates strongly with low $W_0^{\lambda 2796}$. We also demonstrated that there exists a large overlap between the DLA and Mg II population, and DLAs evolve in metallicity as a population, albeit weakly with a best-fit gradient of -0.26 ± 0.07 dex per unit redshift and large scatter (Prochaska et al. 2003).

The $W_0^{\lambda 1215}/W_0^{\lambda 2796}$ ratio is similar for weak and strong Mg II systems (Figure 14), and $W_0^{\lambda 1215}/W_0^{\lambda 2796}$ evolves similarly in redshift for both these sets (Figure 15). The only discernible difference in metal line absorption between weak and strong Mg II absorbers is a relative suppression of high ionization lines (Si IV, C IV) in the strong systems. This may be a straightforward result of ionization effects: the strong Mg II are more likely to be associated with neutral DLAs, which are comparatively high in singly ionized species.

The similar $W_0^{\lambda 1215}/W_0^{\lambda 2796}$ and high metallicities we measure for the weaker Mg II systems are difficult to reconcile with a scenario where these systems represent accretion of metal-poor gas from the IGM. These systems are at least as metal rich as the strong Mg II and possibly even more so. However it could follow naturally if the $0.3 \leq W_0^{\lambda 2796} \leq 1.0\text{\AA}$ absorbers represent the remnants of previously ejected material, possibly re-accreting as in a galactic fountain.

In this case the very flat evolution in dN/dX is somewhat surprising in the absence of fallback, since the cumulative deposition of winds into the circumgalactic environment should in time increase the Mg II cross section and hence incidence rate or characteristic abundance. At $z \sim 5.3$ the Hubble time is just long enough to permit galaxy formation, wind propagation, and fallback for a few generations. It will be interesting to test this at $z \gtrsim 6.2$ as Mg II re-emerges from the gap between the *H* and *K* bands. As one approaches $z \sim 7$ the timescales for outflow and fallback become challenging, and in this scenario one would expect the Mg II incidence rate to drop substantially.

6. CONCLUSION

We have presented a large study of chemical abundance properties for the $z > 2$ Mg II systems detected with FIRE in Paper I. We employ optical spectra from MagE, MIKE, HIRES and SDSS to measure vacuum ultraviolet lines such as H I and C IV, as well as singly ionized states of carbon, silicon, iron, and aluminum. By combining these observations with carefully constructed low-redshift control samples, we perform a longitudinal study of H I and metals in Mg II-selected systems from $0 < z < 5.33$, a period of > 12 Gyr. Our main findings are as follows:

1. The most significant difference in chemical evolution comes from H I, with higher redshift systems associated with much stronger H I column densities. A K-S test provided only a 0.008% probability that the low ($z < 2$, $\bar{z}=0.927$) and high ($z > 2$, $\bar{z}=3.402$) $N(\text{H I})$ samples were drawn from the same distribution. At high redshifts, the fraction of $W_0^{\lambda 2796} > 0.3\text{\AA}$ systems associated with DLAs ($40.7_{-9.2}^{+9.8}\%$) is much larger than at lower redshifts ($16.7_{-5.3}^{+7.1}\%$). All high redshift Mg II absorbers are associated with either DLAs or sub-DLAs.
2. Comparison between dN/dX for Mg II-selected DLAs and the general DLA population at $2 < z < 5$ shows that a large fraction (if not all) of high redshift DLAs have $W_0^{\lambda 2796} > 0.4\text{\AA}$ absorption. The metallicities for both populations are not inconsistent with the hypothesis that the two groups are one and the same.
3. Mg II systems associated with sub-DLAs at high redshifts are quite metal rich, with some systems possessing lower limits greater than one-tenth solar in iron, silicon, and aluminum.
4. Besides H I and Mg I, there is no evidence for strong chemical evolution in redshift for Mg II-selected systems. The best candidates for moderate chemical evolution are among the high ionization states (Si IV 1393, Al III 1854, and C IV 1548,1550) with stronger absorption at lower redshifts (plausibly from less H I shielding), but it is unclear that this evolution is not the result of small number counts.
5. Weak $0.3\text{\AA} \leq W_0^{\lambda 2796} \leq 1.0\text{\AA}$ and strong $W_0^{\lambda 2796} > 1.0\text{\AA}$ systems have $W_0^{\lambda 1215}/W_0^{\lambda 2796}$ ratios that are similar in both distribution and redshift evolution. There is some evidence that strong absorbers are associated with weaker high ionization states (Si IV, Al III, C IV), potentially from shielding caused by their higher H I column densities.
6. Applying the taxonomy defined in Churchill et al. (2000b) to the FIRE systems, we find that an overwhelming majority of $0.3\text{\AA} \leq W_0^{\lambda 2796} < 1.0\text{\AA}$ systems are classic+C IV-deficient systems (84.2%). The linear density of this class does not significantly evolve between $2 < z < 5$. Strong $W_0^{\lambda 2796} \geq 1.0\text{\AA}$ systems divide into the DLA/H I-rich and double classes. The strong double dN/dX rises between $z = 2$ and 3 and then falls. The strong DLA/H I-rich dN/dX falls from $z = 2$ to 5; the full $W_0^{\lambda 2796} \geq 0.3\text{\AA}$ DLA/H I-rich dN/dX remains essentially constant over this redshift range.
7. The strongest Mg II systems ($W_0^{\lambda 2796} > 2.75\text{\AA}$; 8 in total) possess unusually strong Fe II absorption and Mg II kinematic spreads (no $W_0^{\lambda 1215}$ or $W_0^{\lambda 1548}$ measurements are available for these systems). These systems do not fall nicely into any of the five system classes defined in Churchill et al. (2000b). It is unclear whether they represent

DLA/H I-rich systems (as they were typically classified), double systems, or an entirely new class generated by physical mechanisms not prevalent at $z < 1.4$.

The FIRE QSO sample was assembled with the goal of maximizing the redshift pathlength at higher redshifts $z > 3$ in order to provide better dN/dX estimates in this range. While the sample accomplished this stated goal, the high QSO redshifts (typically $z_{QSO} > 4$) also greatly increased the probability that the rest-frame UV and near UV transitions (e.g., H I 1215 and C IV 1548) of $z \sim 2$ systems would rest blueward of the Lyman break limit of at least one higher redshift absorber. As a result, our lowest $W_0^{\lambda 1548}$ and $W_0^{\lambda 1215}$ measurements for this $W_0^{\lambda 2796} \geq 0.3\text{\AA}$ FIRE sample are $z = 2.749$ and $z = 2.593$, respectively. In addition to targeting high redshift QSOs to add information on high redshift systems, a new QSO spectroscopic sample looking to improve upon this study should include more QSOs with $z_{QSO} \lesssim 3$ to better establish the chemical compositions of $z = 2 - 2.5$ Mg II systems. It should be possible to use the SDSS DR7 sample to obtain a list of lower redshift QSOs with multiple strong H I systems in this redshift range to strategically observe QSOs with high probabilities of finding Mg II systems. If the H I distribution of these indicators follow that of the general population, then this selection process should not bias the chemical evolution study.

We are extremely grateful to the staff of the Magellan Telescopes and Las Campanas Observatory for their assistance in obtaining the data presented herein. This work also benefitted from discussions with C. Churchill during a brief visit to MIT. RAS also recognizes the culturally significant role of the A.J. Burgasser Chair in Astrophysics. We gratefully acknowledge financial support from the NSF under grants AST-0908920 and AST-1109115. ENS was supported by the MIT Undergraduate Research Opportunity Program (UROP).

REFERENCES

- Aldcroft, T. L., Bechtold, J., & Elvis, M. 1994, *ApJS*, 93, 1
- Asplund, M., Grevesse, N., Sauval, A. J., & Scott, P. 2009, *ARA&A*, 47, 481
- Bahcall, J. N., et al. 1993, *ApJS*, 87, 1
- . 1996, *ApJ*, 457, 19
- Barthel, P. D., Tytler, D. R., & Thomson, B. 1990, *A&AS*, 82, 339
- Bernstein, R., Sheckman, S. A., Gunnels, S. M., Mochnacki, S., & Athey, A. E. 2003, in *Society of Photo-Optical Instrumentation Engineers (SPIE) Conference Series*, Vol. 4841, *Society of Photo-Optical Instrumentation Engineers (SPIE) Conference Series*, ed. M. Iye & A. F. M. Moorwood, 1694–1704
- Bochanski, J. J., et al. 2009, *PASP*, 121, 1409
- Bond, N. A., Churchill, C. W., Charlton, J. C., & Vogt, S. S. 2001, *ApJ*, 562, 641
- Bordoloi, R., et al. 2011, *ApJ*, 743, 10
- Bouché, N., Murphy, M. T., Péroux, C., Csabai, I., & Wild, V. 2006, *MNRAS*, 371, 495
- Bouché, N., Murphy, M. T., Péroux, C., Davies, R., Eisenhauer, F., Förster Schreiber, N. M., & Tacconi, L. 2007, *ApJ*, 669, L5
- Bouwens, R. J., et al. 2010, *ApJ*, 725, 1587
- . 2011, *ApJ*, 737, 90
- Chelouche, D., & Bowen, D. V. 2010, *ApJ*, 722, 1821
- Chen, H.-W., Helsby, J. E., Gauthier, J.-R., Sheckman, S. A., Thompson, I. B., & Tinker, J. L. 2010a, *ApJ*, 714, 1521

- Chen, H.-W., Wild, V., Tinker, J. L., Gauthier, J.-R., Helsby, J. E., Shectman, S. A., & Thompson, I. B. 2010b, *ApJ*, 724, L176
- Churchill, C. W., Mellon, R. R., Charlton, J. C., Jannuzi, B. T., Kirhakos, S., Steidel, C. C., & Schneider, D. P. 2000a, *ApJS*, 130, 91
- . 2000b, *ApJ*, 543, 577
- Churchill, C. W., Rigby, J. R., Charlton, J. C., & Vogt, S. S. 1999, *ApJS*, 120, 51
- Cooksey, K. L., Kao, M. M., Simcoe, R. A., O'Meara, J. M., & Prochaska, J. X. 2012, *ArXiv e-prints*
- Cushing, M. C., Vacca, W. D., & Rayner, J. T. 2004, *PASP*, 116, 362
- Ellison, S. L. 2006, *MNRAS*, 368, 335
- Ellison, S. L., Songaila, A., Schaye, J., & Pettini, M. 2000, *AJ*, 120, 1175
- Feigelson, E. D., & Nelson, P. I. 1985, *ApJ*, 293, 192
- Foltz, C. B., Weymann, R. J., Peterson, B. M., Sun, L., Malkan, M. A., & Chaffee, Jr., F. H. 1986, *ApJ*, 307, 504
- Gauthier, J., Chen, H., & Tinker, J. L. 2009, *ApJ*, 702, 50
- Haehnelt, M. G., Steinmetz, M., & Rauch, M. 1998, *ApJ*, 495, 647
- Jannuzi, B. T., et al. 1998, *ApJS*, 118, 1
- Kacprzak, G. G., & Churchill, C. W. 2011, *ArXiv e-prints*
- Kacprzak, G. G., Churchill, C. W., Evans, J. L., Murphy, M. T., & Steidel, C. C. 2011, *MNRAS*, 416, 3118
- Kundic, T., Hogg, D. W., Blandford, R. D., Cohen, J. G., Lubin, L. M., & Larkin, J. E. 1997, *AJ*, 114, 2276
- Lanzetta, K. M., Turnshek, D. A., & Wolfe, A. M. 1987, *ApJ*, 322, 739
- Lavalley, M., Isobe, T., & Feigelson, E. 1992, in *Astronomical Society of the Pacific Conference Series*, Vol. 25, *Astronomical Data Analysis Software and Systems I*, ed. D. M. Worrall, C. Biemesderfer, & J. Barnes, 245
- Lovegrove, E., & Simcoe, R. A. 2011, *ApJ*, 740, 30
- Lu, L., & Wolfe, A. M. 1994, *AJ*, 108, 44
- Lu, L., Wolfe, A. M., Turnshek, D. A., & Lanzetta, K. M. 1993, *ApJS*, 84, 1
- Lundgren, B. F., et al. 2009, *ApJ*, 698, 819
- Marshall, J. L., et al. 2008, in *Society of Photo-Optical Instrumentation Engineers (SPIE) Conference Series*, Vol. 7014, *Society of Photo-Optical Instrumentation Engineers (SPIE) Conference Series*
- Matejek, M. S., & Simcoe, R. A. 2012, *ArXiv e-prints*
- Ménard, B., Wild, V., Nestor, D., Quider, A., Zibetti, S., Rao, S., & Turnshek, D. 2011, *MNRAS*, 417, 801
- Nestor, D. B., Johnson, B. D., Wild, V., Ménard, B., Turnshek, D. A., Rao, S., & Pettini, M. 2011, *MNRAS*, 412, 1559
- Nestor, D. B., Turnshek, D. A., & Rao, S. M. 2005, *ApJ*, 628, 637
- Newman, P. R., et al. 2004, in *Society of Photo-Optical Instrumentation Engineers (SPIE) Conference Series*, Vol. 5492, *Society of Photo-Optical Instrumentation Engineers (SPIE) Conference Series*, ed. A. F. M. Moorwood & M. Iye, 533–544
- Noterdaeme, P., Srianand, R., & Mohan, V. 2010, *MNRAS*, 403, 906
- Péroux, C., Dessauges-Zavadsky, M., D'Odorico, S., Kim, T.-S., & McMahon, R. G. 2007, *MNRAS*, 382, 177
- Petitjean, P., & Bergeron, J. 1990, *A&A*, 231, 309
- . 1994, *A&A*, 283, 759
- Pontzen, A., et al. 2008, *MNRAS*, 390, 1349
- Prochaska, J. X., Gawiser, E., Wolfe, A. M., Castro, S., & Djorgovski, S. G. 2003, *ApJ*, 595, L9
- Prochaska, J. X., Herbert-Fort, S., & Wolfe, A. M. 2005, *ApJ*, 635, 123
- Prochaska, J. X., & Wolfe, A. M. 1997, *ApJ*, 487, 73
- . 2009, *ApJ*, 696, 1543
- Prochaska, J. X., Wolfe, A. M., Howk, J. C., Gawiser, E., Burles, S. M., & Cooke, J. 2007, *ApJS*, 171, 29
- Prochter, G. E., Prochaska, J. X., & Burles, S. M. 2006, *The Astrophysical Journal*, 639, 766
- Quider, A. M., Nestor, D. B., Turnshek, D. A., Rao, S. M., Monier, E. M., Weyant, A. N., & Busche, J. R. 2011, *AJ*, 141, 137
- Rao, S. M., & Turnshek, D. A. 2000, *ApJS*, 130, 1
- Rao, S. M., Turnshek, D. A., & Nestor, D. B. 2006, *ApJ*, 636, 610
- Robertson, J. G., & Shaver, P. A. 1983, *MNRAS*, 204, 69P
- Rubin, K. H. R., Weiner, B. J., Koo, D. C., Martin, C. L., Prochaska, J. X., Coil, A. L., & Newman, J. A. 2010, *ApJ*, 719, 1503
- Sargent, W. L. W., Boksenberg, A., & Young, P. 1982a, *ApJ*, 252, 54
- Sargent, W. L. W., Steidel, C. C., & Boksenberg, A. 1988, *ApJ*, 334, 22
- . 1989, *ApJS*, 69, 703
- Sargent, W. L. W., Young, P., & Schneider, D. P. 1982b, *ApJ*, 256, 374
- Sargent, W. L. W., Young, P. J., Boksenberg, A., Carswell, R. F., & Whelan, J. A. J. 1979, *ApJ*, 230, 49
- Savage, B. D., & Sembach, K. R. 1991, *ApJ*, 379, 245
- Schneider, D. P., et al. 2010, *AJ*, 139, 2360
- Sheinis, A. I., Bolte, M., Epps, H. W., Kibrick, R. I., Miller, J. S., Radovan, M. V., Bigelow, B. C., & Sutin, B. M. 2002, *PASP*, 114, 851
- Simcoe, R. A. 2011, *ApJ*, 738, 159
- Simcoe, R. A., et al. 2008, in *Society of Photo-Optical Instrumentation Engineers (SPIE) Conference Series*, Vol. 7014, *Society of Photo-Optical Instrumentation Engineers (SPIE) Conference Series*
- Simcoe, R. A., et al. 2010, in *Society of Photo-Optical Instrumentation Engineers (SPIE) Conference Series*, Vol. 7735, *Society of Photo-Optical Instrumentation Engineers (SPIE) Conference Series*
- Steidel, C. C. 1990, *ApJS*, 72, 1
- Steidel, C. C. 1995, in *QSO Absorption Lines*, ed. G. Meylan, 139
- Steidel, C. C., & Sargent, W. L. W. 1992, *ApJS*, 80, 1
- Storrie-Lombardi, L. J., McMahon, R. G., Irwin, M. J., & Hazard, C. 1996, *ApJ*, 468, 121
- Tinker, J. L., & Chen, H. 2010, *ApJ*, 709, 1
- Turnshek, D. A., Wolfe, A. M., Lanzetta, K. M., Briggs, F. H., Cohen, R. D., Foltz, C. B., Smith, H. E., & Wilkes, B. J. 1989, *ApJ*, 344, 567
- Tytler, D., Boksenberg, A., Sargent, W. L. W., Young, P., & Kunth, D. 1987, *ApJS*, 64, 667
- Vogt, S. S., et al. 1994, in *Society of Photo-Optical Instrumentation Engineers (SPIE) Conference Series*, Vol. 2198, *Society of Photo-Optical Instrumentation Engineers (SPIE) Conference Series*, ed. D. L. Crawford & E. R. Craine, 362
- Weiner, B. J., et al. 2009, *ApJ*, 692, 187
- Weymann, R. J., Williams, R. E., Peterson, B. M., & Turnshek, D. A. 1979, *ApJ*, 234, 33
- Wolfe, A. M., Gawiser, E., & Prochaska, J. X. 2005, *ARA&A*, 43, 861
- Wolfe, A. M., Turnshek, D. A., Lanzetta, K. M., & Lu, L. 1993, *ApJ*, 404, 480
- Wright, A. E., Morton, D. C., Peterson, B. A., & Jauncey, D. L. 1982, *MNRAS*, 199, 81
- Young, P., Sargent, W. L. W., & Boksenberg, A. 1982a, *ApJ*, 252, 10
- . 1982b, *ApJS*, 48, 455
- Young, P. J., Sargent, W. L. W., Boksenberg, A., Carswell, R. F., & Whelan, J. A. J. 1979, *ApJ*, 229, 891
- Zibetti, S., Ménard, B., Nestor, D. B., Quider, A. M., Rao, S. M., & Turnshek, D. A. 2007, *ApJ*, 658, 161

Table 1
Complimentary Optical Spectra

Object	z_{QSO}	Instrument	t_{exp} (s)	λ Range ^a (Å)	SNR ^b pix ⁻¹
Q0000-26	4.10	MagE	900	6197-10283	23.0
BR0004-6224	4.51	(none)
BR0016-3544	4.15	(none)
SDSS0106+0048	4.45	SDSS	2700	6624-9219	11.0
SDSS0113-0935	3.67	SDSS	3601	5674-9221	14.8
SDSS0127-0045	4.08	SDSS	5706	6178-9221	16.9
SDSS0140-0839	3.71	MagE	900	5729-10283	38.5
SDSS0203+0012	5.85	(none)
BR0305-4957	4.78	MagE	900	7026-10284	27.2
BR0322-2928	4.62	MagE	900	6832-10274	25.4
SDSS0332-0654	3.69	SDSS	2700	5706-9221	5.2
BR0331-1622	4.32	MagE	900	6467-10283	21.8
BR0353-3820	4.58	MIKE	1800	6783-9423	43.7
BR0418-5723	4.37	MIKE	2400	6528-9423	32.4
SDSS0818+1722	5.90	(none)
SDSS0836+0054	5.82	MagE	900	8290-10274	11.9
SDSS0949+0335	4.05	SDSS	5104	6139-9246	22.7
SDSS1020+0922	3.64	MagE	900	5640-10285	25.2
SDSS1030+0524	6.28	(none)
SDSS1110+0244	4.12	MagE	900	6224-10286	21.0
SDSS1305+0521	4.09	SDSS	4200	6187-9221	9.4
SDSS1306+0356	5.99	MagE	900	8497-10285	3.7
ULAS1319+0950	6.13	MagE	900	8667-10285	5.5
SDSS1402+0146	4.16	SDSS	2702	6272-9221	13.6
SDSS1408+0205	4.01	SDSS	2702	6090-9221	9.7
SDSS1411+1217	5.93	MagE	1800	8424-10284	3.5
Q1422+2309	3.65	HIRES	3000	5652-7306	40.8
SDSS1433+0227	4.72	SDSS	3601	6955-9221	11.3
CFQS1509-1749	6.12	MagE	1800	8655-10285	5.2
SDSS1538+0855	3.55	SDSS	2400	5531-9221	30.1
SDSS1616+0501	4.87	SDSS	2400	7138-9221	9.1
SDSS1620+0020	4.09	SDSS	5400	6187-9261	5.3
SDSS1621-0042	3.70	SDSS	5400	5713-9261	27.5
SDSS2147-0838	4.59	SDSS	2900	6792-9221	12.3
SDSS2228-0757	5.14	SDSS	9607	7466-9221	3.2
SDSS2310+1855	6.04	(none)
BR2346-3729	4.21	(none)

^a Minimum wavelength listed is Ly- α emission wavelength of QSO.

^b Median signal-to-noise ratio redward of Ly- α forest.

Table 2
Absorption Properties for the FIRE Mg II-Selected Sample: Mg Ions

Index #	Sightline	z	$W_0^{\lambda 2796}$ (Å)	$W_0^{\lambda 2803}$ (Å)	$W_0^{\lambda 2852a}$ (Å)	Class
1 ^b	Q0000–26	2.184	0.162 ± 0.031	0.112 ± 0.026	< 0.114
2	Q0000–26	3.390	1.356 ± 0.016	1.145 ± 0.016	0.060 ± 0.014	DLA/H I -Rich
3	BR0004–6224	2.663	0.260 ± 0.045	0.140 ± 0.036	< 0.079
4	BR0004–6224	2.908	0.596 ± 0.047	0.183 ± 0.028	< 0.133	Classic+C IV-Deficient
5	BR0004–6224	2.959	0.569 ± 0.063	0.669 ± 0.047	0.161 ± 0.043	Classic+C IV-Deficient
6	BR0004–6224	3.203	0.558 ± 0.029	0.548 ± 0.026	< 0.081	Classic+C IV-Deficient
7	BR0004–6224	3.694	0.236 ± 0.042	0.234 ± 0.019	< 1.030 ^c
8	BR0004–6224	3.776	1.045 ± 0.046	1.049 ± 0.043	...	DLA/H I -Rich
9	BR0016–3544	2.783	0.517 ± 0.027	0.305 ± 0.026	< 0.047	Classic+C IV-Deficient
10	BR0016–3544	2.819	4.028 ± 0.050	3.639 ± 0.053	0.325 ± 0.045	DLA/H I -Rich
11	BR0016–3544	2.949	0.157 ± 0.026	0.144 ± 0.035	< 0.067
12	BR0016–3544	3.757	1.559 ± 0.041	1.430 ± 0.050	...	Double
13	SDSS0106+0048	3.729	0.842 ± 0.016	0.673 ± 0.015	...	Double
14 ^b	SDSS0113–0935	2.825	0.194 ± 0.029	0.110 ± 0.029	< 0.055
15	SDSS0113–0935	3.544	0.228 ± 0.037	0.186 ± 0.035	0.053 ± 0.015
16	SDSS0113–0935	3.617	0.563 ± 0.024	0.344 ± 0.020	< 0.045	Classic
17	SDSS0127–0045	2.588	1.602 ± 0.025	1.164 ± 0.025	< 0.129	Double
18	SDSS0127–0045	2.945	2.253 ± 0.038	1.583 ± 0.037	0.139 ± 0.040	Double
19	SDSS0127–0045	3.168	0.309 ± 0.024	0.138 ± 0.016	< 0.032	Classic
20	SDSS0127–0045	3.728	0.824 ± 0.012	0.745 ± 0.012	< 0.055	DLA/H I -Rich
21	SDSS0140–0839	2.241	0.405 ± 0.031	0.686 ± 0.043	< 0.077	Classic+C IV-Deficient
22	SDSS0140–0839	3.081	0.558 ± 0.018	0.410 ± 0.027	0.070 ± 0.018	Classic
23	SDSS0140–0839	3.212	0.081 ± 0.014	0.092 ± 0.014	< 0.040
24	SDSS0203+0012	3.711	0.374 ± 0.038	0.250 ± 0.065	< 0.202	Classic+C IV-Deficient
25	SDSS0203+0012	4.313	0.849 ± 0.093	0.824 ± 0.080	< 0.062	Classic+C IV-Deficient
26	SDSS0203+0012	4.482	0.670 ± 0.183	0.623 ± 0.024	0.087 ± 0.026	Classic
27	SDSS0203+0012	4.978	0.886 ± 0.039	0.791 ± 0.056	< 0.114	DLA/H I -Rich
28	BR0305–4957	2.502	0.331 ± 0.024	0.169 ± 0.022	< 0.033	Classic+C IV-Deficient
29	BR0305–4957	2.629	1.113 ± 0.018	0.959 ± 0.023	0.083 ± 0.014	DLA/H I -Rich
30	BR0305–4957	3.354	0.564 ± 0.013	0.412 ± 0.012	< 0.032	Classic+C IV-Deficient
31	BR0305–4957	3.591	1.373 ± 0.017	1.207 ± 0.013	0.173 ± 0.011	DLA/H I -Rich
32	BR0305–4957	4.466	1.792 ± 0.017	1.478 ± 0.029	< 0.057	DLA/H I -Rich
33	BR0322–2928	2.229	0.618 ± 0.020	0.510 ± 0.021	< 0.056	Classic+C IV-Deficient
34	SDSS0332–0654	3.061	0.883 ± 0.084	0.608 ± 0.059	< 0.133	Classic+C IV-Deficient
35	BR0331–1622	2.295	1.836 ± 0.067	1.714 ± 0.056	< 0.137	DLA/H I -Rich
36	BR0331–1622	2.593	0.223 ± 0.019	0.185 ± 0.019	< 0.086
37	BR0331–1622	2.927	1.382 ± 0.039	1.098 ± 0.045	...	Double
38	BR0331–1622	3.557	0.707 ± 0.033	0.582 ± 0.033	0.127 ± 0.012	DLA/H I -Rich
39	BR0353–3820	1.987	3.131 ± 0.030	2.717 ± 0.026	0.358 ± 0.043	DLA/H I -Rich
40	BR0353–3820	2.696	0.381 ± 0.014	0.232 ± 0.014	< 0.036	Classic+C IV-Deficient
41	BR0353–3820	2.754	4.599 ± 0.016	4.325 ± 0.019	1.290 ± 0.027	DLA/H I -Rich
42	BR0418–5723	2.030	1.449 ± 0.072	1.009 ± 0.080	< 0.272	DLA/H I -Rich
43	BR0418–5723	2.978	1.850 ± 0.072	2.136 ± 0.099	< 1.106	DLA/H I -Rich
44	SDSS0818+1722	3.563	0.640 ± 0.072	0.427 ± 0.029	< 0.151	Classic+C IV-Deficient
45	SDSS0818+1722	4.431	0.457 ± 0.052	0.138 ± 0.010	< 0.055	Classic+C IV-Deficient
46	SDSS0818+1722	5.065	0.841 ± 0.061	0.533 ± 0.046	< 0.048	Classic+C IV-Deficient
47	SDSS0836+0054	2.299	0.455 ± 0.022	0.300 ± 0.021	...	Classic+C IV-Deficient
48	SDSS0836+0054	3.744	2.607 ± 0.024	1.992 ± 0.031	...	Double
49	SDSS0949+0335	2.289	2.852 ± 0.062	2.408 ± 0.054	1.016 ± 0.096	DLA/H I -Rich
50	SDSS0949+0335	3.310	2.033 ± 0.039	1.665 ± 0.033	0.257 ± 0.026	DLA/H I -Rich
51	SDSS1020+0922	2.046	0.406 ± 0.045	0.288 ± 0.047	< 0.077	Classic+C IV-Deficient
52	SDSS1020+0922	2.593	0.464 ± 0.026	0.499 ± 0.022	0.188 ± 0.036	DLA/H I -Rich
53	SDSS1020+0922	2.749	0.652 ± 0.023	0.518 ± 0.024	< 0.079	C IV-Deficient
54	SDSS1020+0922	3.479	0.118 ± 0.016	0.085 ± 0.019	< 0.105
55	SDSS1030+0524	2.188	0.317 ± 0.017	0.291 ± 0.017	< 0.115	Classic+C IV-Deficient
56	SDSS1030+0524	2.780	2.617 ± 0.069	1.855 ± 0.086	< 0.282	Double
57	SDSS1030+0524	4.583	1.857 ± 0.031	2.139 ± 0.127	< 0.118	Double
58	SDSS1030+0524	4.948	0.447 ± 0.017	0.278 ± 0.019	< 0.056	C IV-Deficient
59	SDSS1030+0524	5.130	0.138 ± 0.013	0.089 ± 0.023	< 0.031
60	SDSS1110+0244	2.119	3.041 ± 0.041	2.884 ± 0.042	0.354 ± 0.045	DLA/H I -Rich

Table 2
Absorption Properties for the FIRE Mg II-Selected Sample: Mg Ions (*Continued*)

Index #	Sightline	z	$W_0^{\lambda 2796}$ (Å)	$W_0^{\lambda 2803}$ (Å)	$W_0^{\lambda 2852a}$ (Å)	Class
61	SDSS1110+0244	2.223	0.205 ± 0.024	0.121 ± 0.029	< 0.090
62	SDSS1305+0521	2.302	1.993 ± 0.095	1.533 ± 0.095	< 0.321	DLA/H I -Rich
63	SDSS1305+0521	2.753	0.378 ± 0.040	0.319 ± 0.037	< 0.115	Classic+C iv-Deficient
64	SDSS1305+0521	3.235	0.328 ± 0.025	0.130 ± 0.025	< 0.118	C iv-Deficient
65	SDSS1305+0521	3.680	1.781 ± 0.068	1.583 ± 0.039	...	DLA/H I -Rich
66	SDSS1306+0356	2.533	3.307 ± 0.101	3.019 ± 0.088	< 0.126	DLA/H I -Rich
67	SDSS1306+0356	3.490	0.648 ± 0.031	0.526 ± 0.044	< 0.229	Classic+C iv-Deficient
68	SDSS1306+0356	4.615	0.983 ± 0.078	0.724 ± 0.038	0.076 ± 0.021	DLA/H I -Rich
69	SDSS1306+0356	4.865	2.798 ± 0.044	3.049 ± 0.087	< 0.256	Double
70	SDSS1306+0356	4.882	1.941 ± 0.079	2.276 ± 0.040	0.138 ± 0.035	DLA/H I -Rich
71	ULAS1319+0950	4.569	0.406 ± 0.062	0.177 ± 0.029	< 0.104	Classic+C iv-Deficient
72	SDSS1402+0146	3.277	1.075 ± 0.018	1.034 ± 0.028	0.065 ± 0.019	DLA/H I -Rich
73	SDSS1402+0146	3.454	0.341 ± 0.016	0.112 ± 0.018	< 0.076	C iv-Deficient
74	SDSS1408+0205	1.982	2.174 ± 0.056	1.769 ± 0.054	0.268 ± 0.079	DLA/H I -Rich
75	SDSS1408+0205	1.991	0.914 ± 0.041	0.555 ± 0.042	< 0.224	Classic+C iv-Deficient
76	SDSS1408+0205	2.462	1.385 ± 0.040	1.029 ± 0.035	< 0.129	DLA/H I -Rich
77	SDSS1411+1217	2.237	0.627 ± 0.041	0.334 ± 0.045	0.115 ± 0.035	Classic+C iv-Deficient
78	SDSS1411+1217	3.477	0.343 ± 0.016	0.179 ± 0.022	< 0.168	Classic+C iv-Deficient
79	SDSS1411+1217	4.929	0.644 ± 0.023	0.488 ± 0.018	< 0.096	Double
80	SDSS1411+1217	5.055	0.207 ± 0.013	0.092 ± 0.015	< 0.034
81	SDSS1411+1217	5.250	0.330 ± 0.013	0.190 ± 0.011	< 0.072	Classic
82	SDSS1411+1217	5.332	0.197 ± 0.013	0.241 ± 0.011
83 ^d	Q1422+2309	3.540	0.342 ± 0.018	0.167 ± 0.012	0.023 ± 0.004	Classic
84	SDSS1433+0227	2.772	0.735 ± 0.018	0.601 ± 0.024	< 0.051	Classic+C iv-Deficient
85	CFQS1509-1749	3.128	0.858 ± 0.093	0.773 ± 0.043	< 0.094	Double
86	CFQS1509-1749	3.266	0.896 ± 0.021	0.711 ± 0.023	< 0.079	Classic+C iv-Deficient
87	CFQS1509-1749	3.392	5.585 ± 0.071	5.082 ± 0.050	1.565 ± 0.039	DLA/H I -Rich
88	SDSS1538+0855	2.638	0.278 ± 0.027	0.206 ± 0.028	< 0.040
89	SDSS1538+0855	3.498	0.151 ± 0.011	0.122 ± 0.014	< 0.028
90	SDSS1616+0501	2.741	1.510 ± 0.044	0.923 ± 0.051	< 0.232	Classic+C iv-Deficient
91	SDSS1616+0501	3.275	0.600 ± 0.036	0.494 ± 0.110	< 0.367	Classic+C iv-Deficient
92	SDSS1616+0501	3.396	0.960 ± 0.036	0.631 ± 0.113	0.209 ± 0.050	DLA/H I -Rich
93	SDSS1616+0501	3.450	0.606 ± 0.033	0.557 ± 0.053	< 0.525	Classic+C iv-Deficient
94	SDSS1616+0501	3.733	2.252 ± 0.189	1.421 ± 0.068	...	DLA/H I -Rich
95	SDSS1620+0020	2.910	1.130 ± 0.058	1.063 ± 0.058	< 0.250	Double
96	SDSS1620+0020	3.273	0.965 ± 0.043	0.635 ± 0.052	< 0.129	Classic
97	SDSS1620+0020	3.620	1.357 ± 0.065	1.091 ± 0.042	0.090 ± 0.028	Double
98	SDSS1620+0020	3.752	1.656 ± 0.065	1.550 ± 0.095	...	DLA/H I -Rich
99	SDSS1621-0042	2.678	0.176 ± 0.017	0.135 ± 0.016	< 0.037
100	SDSS1621-0042	3.106	0.974 ± 0.011	1.011 ± 0.012	0.128 ± 0.017	Classic
101	SDSS2147-0838	2.286	0.977 ± 0.040	0.567 ± 0.033	< 0.220	Classic+C iv-Deficient
102	SDSS2228-0757	3.175	0.304 ± 0.037	0.243 ± 0.031	< 0.151	Classic+C iv-Deficient
103	SDSS2310+1855	2.243	1.441 ± 0.050	0.781 ± 0.049	< 0.090	Double
104	SDSS2310+1855	2.351	0.807 ± 0.042	0.492 ± 0.035	< 0.072	Classic+C iv-Deficient
105	SDSS2310+1855	2.643	0.863 ± 0.036	0.339 ± 0.059	0.077 ± 0.016	Classic+C iv-Deficient
106	SDSS2310+1855	3.300	0.665 ± 0.039	0.457 ± 0.034	< 0.046	Classic+C iv-Deficient
107	BR2346-3729	2.830	1.633 ± 0.049	1.421 ± 0.037	0.185 ± 0.060	DLA/H I -Rich
108	BR2346-3729	2.923	0.557 ± 0.030	0.636 ± 0.034	< 0.131	Classic+C iv-Deficient
109	BR2346-3729	3.619	0.412 ± 0.031	0.240 ± 0.019	0.055 ± 0.016	Classic+C iv-Deficient
110	BR2346-3729	3.692	0.385 ± 0.016	0.413 ± 0.046	< 0.089	Classic+C iv-Deficient

^a Upper limits are 3σ .

^b Suspected false positive.

^c Blended line.

^d $W_0^{\lambda 2796}$ and $W_0^{\lambda 2803}$ values adjusted relative to Paper I.

Table 3
The Low Redshift Compilation Sample^a

ID #	Sightline	z_{QSO}	z	$W_0^{\lambda 2796}$ (Å)	$W_0^{\lambda 1215b}$ (Å)	$W_0^{\lambda 1393b}$ (Å)	$W_0^{\lambda 1548b}$ (Å)	$W_0^{\lambda 2600b}$ (Å)	Ref. ^c
L1	0001+087	3.243	1.085	0.249 ± 0.034	< 0.264	1
L2	0001+087	3.243	1.416	0.584 ± 0.046	< 0.228	1
L3	0002+051	1.899	0.591	0.103 ± 0.000	< 0.012	2,3
L4	0002+051	1.900	0.851	1.043 ± 0.000	2.470 ± 0.080	< 0.918	1.260 ± 0.060	0.419 ± 0.022	2,4,5
L5	0002+051	1.900	0.956	0.052 ± 0.000	0.821 ± 0.003	< 0.869	0.509 ± 0.001	< 0.005	2,3,4
L6	0002-422	2.758	0.837	4.683 ± 0.381	2.940 ± 0.272	6,7
L7	0002-422	2.758	1.541	0.480 ± 0.043	0.710 ± 0.000	< 0.275	7
L8	0004+171	2.890	0.807	1.533 ± 0.061	1
L9	0009-0138	2.000	1.386	0.880 ± 0.084	0.457 ± 0.042	5
L10	0013-004	2.086	0.447	0.684 ± 0.069	8
L11	0013-004	2.086	1.967	2.662 ± 0.152	0.340 ± 0.034	0.698 ± 0.044	1.473 ± 0.071	5,8
L12	0013-004	2.086	1.972	4.709 ± 0.030	< 1.211 ^d	0.828 ± 0.037	2.459 ± 0.081	5,8
L13	0014+813	3.377	1.111	1.625 ± 0.001	0.880 ± 0.000	1,8
L14	0014+813	3.377	1.113	2.471 ± 0.043	2.140 ± 0.028	8
L15	0017+154	2.014	1.364	0.360 ± 0.072	< 0.141 ^e	9
L16	0017+154	2.014	1.626	1.420 ± 0.284	1.043 ± 0.209	0.830 ± 0.166	9
L17	0019+0107	2.134	1.828	1.612 ± 0.113	0.392 ± 0.046	5
L18	0027+0149	2.350	1.266	0.560 ± 0.062	< 0.309	5
L19	0029+073	3.259	1.176	0.685 ± 0.051	< 0.937 ^d	1
L20	0029+073	3.259	1.403	0.179 ± 0.033	< 0.250	1
L277	1836+511	2.827	0.756	0.837 ± 0.085	1
L278	1836+511	2.827	0.818	3.570 ± 0.182	< 0.908	1
L279	1836+511	2.827	0.864	0.901 ± 0.113	< 0.885	1
L280	1836+511	2.827	1.126	0.630 ± 0.071	< 0.776	1
L281	1857+566	1.573	0.715	0.647 ± 0.129	< 0.476 ^e	9
L282	1857+566	1.573	1.234	0.823 ± 0.165	0.555 ± 0.111	9
L283	1901+3155	0.635	0.390	0.453 ± 0.043	13
L284	2000-330	3.777	1.454	0.187 ± 0.020	< 0.110 ^d	10
L285	2003-025	1.457	1.211	2.654 ± 0.140	< 1.989	0.954 ± 0.099	13
L286	2038-012	2.783	0.795	1.404 ± 0.100	< 0.863	1
L287	2044-168	1.943	1.328	0.503 ± 0.069	7
L288	2048+196	2.364	1.116	1.517 ± 0.303	1.309 ± 0.262	9
L289	2048+312	3.185	1.348	0.775 ± 0.081	< 0.532	1
L290	2116-358	2.341	1.996	1.936 ± 0.103	1.172 ± 0.070	7
L291	2126-158	3.275	2.022	0.675 ± 0.096	0.990 ± 0.000	0.340 ± 0.000	7,15
L292	2128-123	0.501	0.430	0.406 ± 0.000	2.915 ± 0.003	0.196 ± 0.035	0.394 ± 0.001	0.266 ± 0.049	2,4,17,19
L293	2145+067	0.990	0.790	0.485 ± 0.000	1.391 ± 0.001	0.411 ± 0.003	1.129 ± 0.003	< 0.116	2,5,17,23
L294	2149+212	1.536	0.911	0.717 ± 0.143	< 0.947	9
L295	2149+212	1.536	1.002	2.457 ± 0.491	1.004 ± 0.201	9
L296	2206-199	2.559	0.752	0.930 ± 0.046	< 0.457	8
L297	2206-199	2.559	1.017	0.932 ± 0.069	0.560 ± 0.035	8
L298	2212-299	2.703	1.938	0.616 ± 0.082	0.595 ± 0.119	< 0.408	7,9
L299	2222+051	2.326	1.605	0.760 ± 0.152	0.319 ± 0.064	9
L300	2233+131	3.295	1.026	0.444 ± 0.074	< 0.370	1
L301	2233+136	3.209	1.096	0.324 ± 0.038	< 0.334	1
L302	2237-0607	4.558	1.672	1.347 ± 0.187	< 0.936	11
L303	2239-386	3.511	1.033	0.453 ± 0.064	10
L304	2248+192	1.793	1.270	1.031 ± 0.206	< 0.440 ^e	9
L305	2251+243	2.328	1.090	0.455 ± 0.091	< 0.694	< 0.694	9,13
L306	2341-235	2.822	1.076	0.458 ± 0.053	< 0.434	1
L307	2342+089	2.784	0.723	1.480 ± 0.046	8
L308	2342+089	2.784	0.838	0.316 ± 0.027	< 0.326	8
L309	2342+089	2.784	0.949	0.323 ± 0.031	< 0.308	8
L310	2354+144	1.813	1.576	1.071 ± 0.214	< 0.362	9
L311	2359+003	2.896	1.024	0.371 ± 0.069	< 0.544	1
L312	2359+003	2.896	1.344	0.776 ± 0.094	< 0.469	1
L313	2359+068	3.234	0.896	0.644 ± 0.037	1

^a This table is available in a machine-readable form in the online journal. A portion is shown here for guidance regarding its form and content.

^b Upper limits are 5σ .

^c REFERENCES.—(1) Sargent et al. (1989); (2) Churchill et al. (2000a); (3) Churchill et al. (1999); (4) Jannuzi et al. (1998); (5) Steidel & Sargent (1992); (6) Sargent et al. (1979); (7) Lanzetta et al. (1987); (8) Sargent et al. (1988); (9) Barthel et al. (1990); (10) Steidel (1990); (11) Storrie-Lombardi et al. (1996); (12) Sargent et al. (1982a); (13) Aldcroft et al. (1994); (14) Young et al. (1982b); (15) Petitjean & Bergeron (1994); (16) Wright et al. (1982); (17) Petitjean & Bergeron (1990); (18) Young et al. (1982a); (19) Tytler et al. (1987); (20) Foltz et al. (1986); (21) Robertson & Shaver (1983); (22) Bahcall et al. (1996); (23) Bahcall et al. (1993).

^d Blended line.

^e FeII 2382.

^f FeII 2586.

^g FeII 1608.

Table 4
 $N(\text{H I})$ and Metallicity Measurements, FIRE sample

Index #	Sightline	z	$\log N(\text{H I})$ ($\log \text{cm}^{-2}$)	[Fe/H] ^a	[C/H] ^b	[Si/H] ^c	[Al/H] ^d	[Mg/H] ^e
2	Q0000-26	3.390	21.40 ± 0.05	> -2.524	> -1.330	> -2.920	> -3.045
13	SDSS0106+0048	3.729	19.45 ± 0.15	> -1.442	> -0.858	> -0.855	> -1.379
15	SDSS0113-0935	3.544	19.05 ± 0.10	> -1.692
16	SDSS0113-0935	3.617	19.40 ± 0.15	> -1.497	> -1.523	> -1.731
18	SDSS0127-0045	2.945	20.03 ± 0.15	> -2.052	> -1.228	> -1.614
19	SDSS0127-0045	3.168	19.20 ± 0.15	> -1.889
20	SDSS0127-0045	3.728	21.20 ± 0.10	> -2.845	> -3.144	> -2.708	> -2.890	> -3.073
22	SDSS0140-0839	3.081	19.25 ± 0.20	-1.046 ± 0.312	> -0.952	> -0.968	> -1.453
23	SDSS0140-0839	3.212	18.95 ± 0.20	-1.266 ± 0.312	-1.735 ± 0.303	-1.923 ± 0.331
30	BR0305-4957	3.354	20.25 ± 0.10	-2.729 ± 0.201	> -2.469
31	BR0305-4957	3.591	20.40 ± 0.20	> -1.739	> -1.992
32	BR0305-4957	4.466	20.65 ± 0.10	> -2.191	> -2.229	> -1.596	> -1.894	> -2.170
34	SDSS0332-0654	3.061	18.75 ± 0.20	> -0.872	> -0.809
38	BR0331-1622	3.557	21.10 ± 0.10	> -2.272	> -2.263	> -3.108
50	SDSS0949+0335	3.310	19.90 ± 0.10	> -0.994	> -0.857	> -1.151	> -1.301
52	SDSS1020+0922	2.593	21.10 ± 0.20	> -2.232	-1.505 ± 0.324	> -2.644	> -3.204
53	SDSS1020+0922	2.749	20.10 ± 0.10	> -1.684	> -1.657	> -2.030	> -2.175
54	SDSS1020+0922	3.479	19.35 ± 0.10	-2.482 ± 0.214	-1.795 ± 0.213	-2.347 ± 0.219
64	SDSS1305+0521	3.235	19.35 ± 0.15	> -1.358	> -1.968
65	SDSS1305+0521	3.680	21.50 ± 0.15	> -2.489	> -3.239	> -2.551	> -2.837	> -2.914
72	SDSS1402+0146	3.277	21.05 ± 0.10	> -2.313	> -2.198	> -2.557	> -2.675
73	SDSS1402+0146	3.454	19.65 ± 0.15	-1.392 ± 0.254	> -0.988	> -1.245	> -2.291
83 ^f	Q1422+2309	3.540	18.70 ± 0.10	> -1.420	-1.186 ± 0.245	> -1.366
88	SDSS1538+0855	2.638	19.00 ± 0.20	> -1.434	> -1.035	> -1.572
89	SDSS1538+0855	3.498	18.90 ± 0.20	> -1.549	> -1.710
91	SDSS1616+0501	3.275	20.05 ± 0.15	> -2.003
92	SDSS1616+0501	3.396	21.20 ± 0.10	> -2.136	> -3.077
93	SDSS1616+0501	3.450	19.45 ± 0.15	> -0.671	> -1.518
94	SDSS1616+0501	3.733	20.50 ± 0.20	> -2.022	> -1.697	> -2.198	> -2.026
97	SDSS1620+0020	3.620	20.00 ± 0.15	> -1.785
98	SDSS1620+0020	3.752	20.90 ± 0.10	> -2.215	> -2.528	> -2.010	> -1.977	> -2.401
99	SDSS1621-0042	2.678	18.35 ± 0.35	> -1.134
100	SDSS1621-0042	3.106	19.90 ± 0.15	-1.792 ± 0.242	> -1.214	> -1.404	> -1.521

^a Fe II.

^b C II.

^c Si II.

^d Al II.

^e Mg II.

^f $[\text{O}/\text{H}] = -2.037 \pm 0.247$ (O I).

Table 5Absorption Properties for the FIRE Mg II-Selected Sample: H I 1215
and O I 1302

Index #	Sightline	z	$W_0^{\lambda 1215}$ (Å)	$W_0^{\lambda 1302^a}$ (Å)
2	Q0000-26	3.390	33.182 ± 0.093	...
13	SDSS0106+0048	3.729	3.863 ± 0.139	...
15	SDSS0113-0935	3.544	2.470 ± 0.068	< 0.142
16	SDSS0113-0935	3.617	3.651 ± 0.061	< 0.156
18	SDSS0127-0045	2.945	8.102 ± 0.176	...
19	SDSS0127-0045	3.168	2.916 ± 0.088	...
20	SDSS0127-0045	3.728	26.937 ± 0.357	...
22	SDSS0140-0839	3.081	3.086 ± 0.026	...
23	SDSS0140-0839	3.212	2.216 ± 0.014	...
30	BR0305-4957	3.354	9.520 ± 0.097	...
31	BR0305-4957	3.591	11.252 ± 0.062	...
32	BR0305-4957	4.466	14.851 ± 0.044	$< 0.488^b$
34	SDSS0332-0654	3.061	1.800 ± 0.169	...
38	BR0331-1622	3.557	24.205 ± 0.085	...
50	SDSS0949+0335	3.310	6.421 ± 0.079	...
52	SDSS1020+0922	2.593	24.207 ± 0.157	...
53	SDSS1020+0922	2.749	8.043 ± 0.074	...
54	SDSS1020+0922	3.479	3.452 ± 0.021	< 0.033
64	SDSS1305+0521	3.235	3.452 ± 0.189	...
65	SDSS1305+0521	3.680	36.708 ± 1.087	...
72	SDSS1402+0146	3.277	22.946 ± 0.294	...
73	SDSS1402+0146	3.454	4.842 ± 0.123	...
83	Q1422+2309	3.540	2.222 ± 0.002	0.016 ± 0.002
88	SDSS1538+0855	2.638	2.340 ± 0.034	...
89	SDSS1538+0855	3.498	2.101 ± 0.023	< 0.103
91	SDSS1616+0501	3.275	7.606 ± 0.459	...
92	SDSS1616+0501	3.396	26.912 ± 0.838	...
93	SDSS1616+0501	3.450	3.862 ± 0.296	...
94	SDSS1616+0501	3.733	12.572 ± 0.450	...
97	SDSS1620+0020	3.620	7.190 ± 0.491	...
98	SDSS1620+0020	3.752	19.499 ± 1.038	...
99	SDSS1621-0042	2.678	1.263 ± 0.039	...
100	SDSS1621-0042	3.106	6.420 ± 0.070	...

^a Upper limits are 3σ .^b Blended line.

Table 6
Absorption Properties for the FIRE Mg II-Selected Sample: Fe Ions

Index #	Sightline	z	$W_0^{\lambda 1608a}$ (Å)	$W_0^{\lambda 2344a}$ (Å)	$W_0^{\lambda 2374a}$ (Å)	$W_0^{\lambda 2382a}$ (Å)	$W_0^{\lambda 2586a}$ (Å)	$W_0^{\lambda 2600a}$ (Å)
1 ^b	Q0000–26	2.184	...	< 0.056	< 0.056	< 0.052	< 0.471 ^c	< 0.106
2	Q0000–26	3.390	0.190 ± 0.010	0.313 ± 0.031	0.302 ± 0.021	0.514 ± 0.017	0.329 ± 0.025	0.523 ± 0.016
3	BR0004–6224	2.663	...	< 0.236	< 0.266	< 0.334	< 0.258	< 0.264
4	BR0004–6224	2.908	...	< 0.241	< 0.277 ^c	< 0.199	< 0.118	< 0.131
5	BR0004–6224	2.959	...	0.318 ± 0.058	< 0.203	0.549 ± 0.084	< 0.293 ^c	0.557 ± 0.047
6	BR0004–6224	3.203	...	0.284 ± 0.054	< 0.099	0.463 ± 0.049	0.109 ± 0.031	< 0.588 ^c
7	BR0004–6224	3.694	...	< 0.081	< 0.180 ^c	< 0.335	< 0.133	< 0.090
8	BR0004–6224	3.776	...	0.683 ± 0.044	0.209 ± 0.031	0.730 ± 0.031	0.446 ± 0.044	0.697 ± 0.032
9	BR0016–3544	2.783	...	< 0.143	< 0.102	< 0.114	< 0.077	< 0.093
10	BR0016–3544	2.819	...	1.295 ± 0.058	0.893 ± 0.059	2.593 ± 0.089	1.387 ± 0.057	2.434 ± 0.048
11	BR0016–3544	2.949	...	< 0.082	< 0.136	...	< 0.152	< 0.084
12	BR0016–3544	3.757	0.204 ± 0.022	0.400 ± 0.020
13	SDSS0106+0048	3.729	< 0.448	0.150 ± 0.034	< 0.091	0.156 ± 0.016	0.133 ± 0.040	0.211 ± 0.013
14 ^b	SDSS0113–0935	2.825	...	< 0.087	< 0.152	< 0.181	< 0.100	< 0.091
15	SDSS0113–0935	3.544	< 0.148	< 0.115	< 0.064	< 0.086	< 0.045	< 0.042
16	SDSS0113–0935	3.617	< 0.135	< 0.040	< 0.068	< 0.065	< 0.062	< 0.111
17	SDSS0127–0045	2.588	...	0.131 ± 0.031	< 0.142	0.244 ± 0.044	0.093 ± 0.027	0.187 ± 0.039
18	SDSS0127–0045	2.945	...	0.137 ± 0.026	< 0.118	0.439 ± 0.036	< 0.104	0.346 ± 0.031
19	SDSS0127–0045	3.168	< 0.130	< 0.052	< 0.057	< 0.051	< 0.036	< 0.039
20	SDSS0127–0045	3.728	< 0.421	0.188 ± 0.017	< 0.074	0.549 ± 0.015	0.259 ± 0.026	0.472 ± 0.011
21	SDSS0140–0839	2.241	0.235 ± 0.008	0.491 ± 0.011	0.351 ± 0.031	0.524 ± 0.030
22	SDSS0140–0839	3.081	0.071 ± 0.009	< 0.088	0.081 ± 0.019	0.203 ± 0.021	0.112 ± 0.023	0.249 ± 0.027
23	SDSS0140–0839	3.212	< 0.031	< 0.101	< 0.059	< 0.064	< 0.052	< 0.059
24	SDSS0203+0012	3.711	...	< 0.309	< 0.303	< 0.398	< 0.215	< 0.186
25	SDSS0203+0012	4.313	...	0.230 ± 0.041	< 0.248	0.503 ± 0.094
26	SDSS0203+0012	4.482	...	0.369 ± 0.039	0.240 ± 0.071	0.406 ± 0.027
27	SDSS0203+0012	4.978	0.473 ± 0.034	0.612 ± 0.101
28	BR0305–4957	2.502	...	< 0.084	< 0.078	< 0.726 ^c	< 0.046	< 0.074
29	BR0305–4957	2.629	...	0.248 ± 0.029	0.061 ± 0.018	0.660 ± 0.017
30	BR0305–4957	3.354	...	0.058 ± 0.019	< 0.033	0.179 ± 0.014
31	BR0305–4957	3.591	0.246 ± 0.010	0.510 ± 0.010	0.202 ± 0.009	0.698 ± 0.010	0.409 ± 0.008	0.728 ± 0.009
32	BR0305–4957	4.466	0.162 ± 0.016	0.438 ± 0.016	0.123 ± 0.012	0.782 ± 0.017
33	BR0322–2928	2.229	0.391 ± 0.012	0.268 ± 0.022	0.425 ± 0.026
34	SDSS0332–0654	3.061	< 0.360	< 0.835	< 0.229	0.288 ± 0.076	< 0.225	< 0.257
35	BR0331–1622	2.295	...	1.306 ± 0.082	0.274 ± 0.045	0.935 ± 0.048	0.655 ± 0.108	1.075 ± 0.083
36	BR0331–1622	2.593	...	< 0.075	< 0.154	< 0.094	< 0.098	< 0.183
37	BR0331–1622	2.927	...	< 0.339 ^c	< 0.170	0.351 ± 0.059	< 0.105	0.201 ± 0.047
38	BR0331–1622	3.557	0.211 ± 0.012	0.438 ± 0.032	0.274 ± 0.020	0.527 ± 0.023	0.430 ± 0.022	0.460 ± 0.019
39	BR0353–3820	1.987	...	0.872 ± 0.006	0.364 ± 0.008	1.534 ± 0.007	0.908 ± 0.008	1.568 ± 0.008
40	BR0353–3820	2.696	...	< 0.050	< 0.070	< 1.238 ^c	< 0.047	< 0.044
41	BR0353–3820	2.754	...	2.452 ± 0.030	1.403 ± 0.025	3.265 ± 0.022	2.470 ± 0.021	3.383 ± 0.021
42	BR0418–5723	2.030	...	0.422 ± 0.007	< 0.291 ^c	0.715 ± 0.007	0.284 ± 0.007	0.717 ± 0.009
43	BR0418–5723	2.978	...	< 0.374	0.692 ± 0.133	0.750 ± 0.177	0.563 ± 0.149	0.953 ± 0.056
44	SDSS0818+1722	3.563	...	0.244 ± 0.023	< 0.178	0.294 ± 0.013	0.267 ± 0.011	0.285 ± 0.020
45	SDSS0818+1722	4.431	< 0.029	< 0.089	< 0.041	< 0.062
46	SDSS0818+1722	5.065	< 0.045	0.153 ± 0.015	0.333 ± 0.022
47	SDSS0836+0054	2.299	< 0.149	< 0.081 ^c
48	SDSS0836+0054	3.744	...	< 0.062	0.130 ± 0.015	0.346 ± 0.020
49	SDSS0949+0335	2.289	...	1.026 ± 0.070	0.616 ± 0.056	1.305 ± 0.054	0.998 ± 0.069	1.071 ± 0.086
50	SDSS0949+0335	3.310	0.271 ± 0.035	0.544 ± 0.031	0.326 ± 0.048	0.989 ± 0.040	0.408 ± 0.045	0.893 ± 0.023
51	SDSS1020+0922	2.046	...	0.106 ± 0.015	< 0.062	0.341 ± 0.022	< 0.060	0.187 ± 0.023
52	SDSS1020+0922	2.593	0.178 ± 0.009	0.325 ± 0.025	0.302 ± 0.042	0.340 ± 0.037	0.307 ± 0.020	...
53	SDSS1020+0922	2.749	0.051 ± 0.009	0.089 ± 0.027	0.112 ± 0.021	0.323 ± 0.020	0.210 ± 0.025	0.313 ± 0.029
54	SDSS1020+0922	3.479	...	< 0.056	< 0.070	< 0.072	...	< 0.298
55	SDSS1030+0524	2.188
56	SDSS1030+0524	2.780	...	< 1.457 ^c	< 2.287 ^c	< 0.977 ^c	< 0.207	0.766 ± 0.098
57	SDSS1030+0524	4.583	0.303 ± 0.013	0.501 ± 0.077	0.208 ± 0.032	0.834 ± 0.053
58	SDSS1030+0524	4.948	< 0.112	0.123 ± 0.030
59	SDSS1030+0524	5.130	< 0.083	< 0.123	< 0.056
60	SDSS1110+0244	2.119	...	1.732 ± 0.048	1.000 ± 0.035	2.141 ± 0.028	1.618 ± 0.046	2.245 ± 0.046

Table 6
Absorption Properties for the FIRE Mg II-Selected Sample: Fe Ions (*Continued*)

Index #	Sightline	z	$W_0^{\lambda 1608a}$ (Å)	$W_0^{\lambda 2344a}$ (Å)	$W_0^{\lambda 2374a}$ (Å)	$W_0^{\lambda 2382a}$ (Å)	$W_0^{\lambda 2586a}$ (Å)	$W_0^{\lambda 2600a}$ (Å)
61	SDSS1110+0244	2.223	...	< 0.061	< 0.095	< 0.084
62	SDSS1305+0521	2.302	...	1.112 ± 0.109	< 0.389	1.161 ± 0.147	0.480 ± 0.160	1.407 ± 0.099
63	SDSS1305+0521	2.753	...	< 0.311	< 0.123	< 0.116	< 0.093	< 0.141
64	SDSS1305+0521	3.235	< 0.181	0.146 ± 0.040	< 0.114	0.112 ± 0.037	< 0.101	< 0.141
65	SDSS1305+0521	3.680	0.443 ± 0.129	0.891 ± 0.048	0.367 ± 0.059	0.932 ± 0.050	0.691 ± 0.037	0.984 ± 0.042
66	SDSS1306+0356	2.533	0.910 ± 0.087	2.214 ± 0.088
67	SDSS1306+0356	3.490	...	< 0.104	< 0.110	0.154 ± 0.038	< 0.139	< 0.101
68	SDSS1306+0356	4.615	...	0.227 ± 0.028	< 0.097	0.332 ± 0.029
69	SDSS1306+0356	4.865	0.734 ± 0.036	1.829 ± 0.122
70	SDSS1306+0356	4.882	1.058 ± 0.027	2.098 ± 0.075
71	ULAS1319+0950	4.569	< 0.062	< 0.139	< 0.078	0.130 ± 0.026
72	SDSS1402+0146	3.277	< 0.161	0.554 ± 0.021	0.225 ± 0.024	0.743 ± 0.033	0.414 ± 0.033	0.725 ± 0.030
73	SDSS1402+0146	3.454	< 0.253 ^c	< 0.052	0.087 ± 0.022	< 0.079
74	SDSS1408+0205	1.982	...	0.780 ± 0.095	< 0.304	0.947 ± 0.104	0.643 ± 0.190	1.268 ± 0.315
75	SDSS1408+0205	1.991	...	< 0.279	< 0.963 ^c	< 0.297	< 0.401	< 0.455
76	SDSS1408+0205	2.462	...	< 0.506	< 0.466	0.808 ± 0.156	0.354 ± 0.035	0.670 ± 0.048
77	SDSS1411+1217	2.237
78	SDSS1411+1217	3.477	...	< 0.375 ^c	< 0.234	...	< 0.115	< 0.107
79	SDSS1411+1217	4.929	< 0.099	< 0.283	0.331 ± 0.024
80	SDSS1411+1217	5.055	< 0.083	< 0.083	< 0.059
81	SDSS1411+1217	5.250	< 0.052	...	< 0.461	< 0.296	< 0.033	< 0.045
82	SDSS1411+1217	5.332	< 0.078	< 0.085	< 0.064	< 0.155	< 0.036	< 0.035
83	Q1422+2309	3.540	...	< 0.028	< 0.019	< 0.017
84	SDSS1433+0227	2.772	...	0.260 ± 0.049	0.118 ± 0.030	0.530 ± 0.031	0.269 ± 0.022	0.518 ± 0.038
85	CFQS1509-1749	3.128	...	0.283 ± 0.029	< 0.160	0.308 ± 0.041	< 0.121	0.311 ± 0.052
86	CFQS1509-1749	3.266	...	0.240 ± 0.026	< 0.139	0.315 ± 0.040	0.158 ± 0.029	0.336 ± 0.049
87	CFQS1509-1749	3.392	...	1.967 ± 0.100	0.753 ± 0.056	3.328 ± 0.054	1.421 ± 0.083	3.298 ± 0.045
88	SDSS1538+0855	2.638	< 0.155	< 0.106	< 0.057	0.164 ± 0.018
89	SDSS1538+0855	3.498	< 0.073	< 0.040	< 0.047	< 0.046
90	SDSS1616+0501	2.741	...	0.541 ± 0.149	< 0.241	0.262 ± 0.056	0.248 ± 0.073	< 0.282
91	SDSS1616+0501	3.275	...	< 0.236	< 0.254	< 0.218	< 0.170	< 0.195
92	SDSS1616+0501	3.396	...	0.559 ± 0.052	0.414 ± 0.032	0.579 ± 0.062	0.755 ± 0.036	0.606 ± 0.048
93	SDSS1616+0501	3.450	< 0.148	< 0.120	< 0.205	0.287 ± 0.074	< 0.193	< 0.168
94	SDSS1616+0501	3.733	< 0.547	0.289 ± 0.086	< 0.245	< 0.214	< 0.170	< 0.449 ^c
95	SDSS1620+0020	2.910	...	< 0.402	< 0.238	0.626 ± 0.108	< 0.172	0.370 ± 0.081
96	SDSS1620+0020	3.273	< 0.343	< 0.217	< 0.187	0.224 ± 0.058	0.273 ± 0.069	0.279 ± 0.080
97	SDSS1620+0020	3.620	< 0.507	< 0.195	< 0.205	< 0.209	< 0.894 ^c	< 0.092
98	SDSS1620+0020	3.752	< 0.874	0.464 ± 0.084	< 0.207	0.570 ± 0.041	0.450 ± 0.080	0.748 ± 0.062
99	SDSS1621-0042	2.678	< 0.086	< 0.070	< 0.065	< 0.079
100	SDSS1621-0042	3.106	< 0.090	0.428 ± 0.020	0.126 ± 0.023	0.598 ± 0.022	0.250 ± 0.022	0.651 ± 0.025
101	SDSS2147-0838	2.286	...	< 0.211	< 0.198	< 0.226	< 0.157	0.233 ± 0.050
102	SDSS2228-0757	3.175	...	< 0.294	< 0.267	< 0.489	< 0.209	< 0.276
103	SDSS2310+1855	2.243
104	SDSS2310+1855	2.351	0.201 ± 0.024	0.396 ± 0.030
105	SDSS2310+1855	2.643	< 0.162	0.238 ± 0.045
106	SDSS2310+1855	3.300	...	< 0.061	< 0.302 ^c	...	< 0.059	< 0.060
107	BR2346-3729	2.830	...	0.295 ± 0.042	< 0.213	0.411 ± 0.083	0.275 ± 0.032	0.613 ± 0.036
108	BR2346-3729	2.923	...	< 0.182	< 0.159	< 0.211	< 0.114	0.196 ± 0.042
109	BR2346-3729	3.619	< 0.475 ^c	< 0.049 ^c	< 0.066	< 0.124
110	BR2346-3729	3.692	...	< 0.530 ^c	< 0.612	0.162 ± 0.030	< 0.138	0.137 ± 0.026

^a Upper limits are 3σ .

^b Suspected false positive.

^c Blended line.

Table 7
Absorption Properties for the FIRE Mg II-Selected Sample: Si Ions

Index #	Sightline	z	$W_0^{\lambda 1260}$ (Å)	$W_0^{\lambda 1304a}$ (Å)	$W_0^{\lambda 1393a}$ (Å)	$W_0^{\lambda 1402a}$ (Å)	$W_0^{\lambda 1526a}$ (Å)	$W_0^{\lambda 1808a}$ (Å)
2	Q0000-26	3.390	0.340 ± 0.011	0.198 ± 0.012
7	BR0004-6224	3.694	< 0.176
8	BR0004-6224	3.776	< 0.162
12	BR0016-3544	3.757	< 0.079
13	SDSS0106+0048	3.729	0.305 ± 0.060	< 0.080
14 ^b	SDSS0113-0935	2.825	< 0.173	< 0.161
15	SDSS0113-0935	3.544	$< 0.300^c$	< 0.136	0.138 ± 0.045	0.216 ± 0.036	< 0.134	< 0.204
16	SDSS0113-0935	3.617	0.313 ± 0.050	< 0.164	0.480 ± 0.040	0.580 ± 0.044	$< 0.200^c$	< 0.112
17	SDSS0127-0045	2.588	$< 0.340^c$
18	SDSS0127-0045	2.945	< 0.129
19	SDSS0127-0045	3.168	< 0.172
20	SDSS0127-0045	3.728	$< 0.603^c$	< 0.120	0.240 ± 0.034	$< 0.104^c$
21	SDSS0140-0839	2.241	0.038 ± 0.006
22	SDSS0140-0839	3.081	0.145 ± 0.008	< 0.035
23	SDSS0140-0839	3.212	0.065 ± 0.008	0.031 ± 0.009	0.039 ± 0.010	...
27	SDSS0203+0012	4.978	< 0.115
30	BR0305-4957	3.354	< 0.035
32	BR0305-4957	4.466	...	0.413 ± 0.008	...	$< 0.854^c$	0.463 ± 0.016	< 0.030
34	SDSS0332-0654	3.061	< 0.468	< 0.798
37	BR0331-1622	2.927	< 0.047
38	BR0331-1622	3.557	0.349 ± 0.009	$< 0.170^c$
41	BR0353-3820	2.754	0.268 ± 0.003
43	BR0418-5723	2.978	$< 0.233^c$
45	SDSS0818+1722	4.431	< 0.078
46	SDSS0818+1722	5.065	0.225 ± 0.019	< 0.033
48	SDSS0836+0054	3.744	$< 0.053^c$
50	SDSS0949+0335	3.310	0.732 ± 0.038	< 0.161
52	SDSS1020+0922	2.593	0.067 ± 0.013
53	SDSS1020+0922	2.749	0.197 ± 0.008	$< 0.156^c$
54	SDSS1020+0922	3.479	...	< 0.036	0.166 ± 0.012	0.185 ± 0.013	< 0.028	< 0.060
57	SDSS1030+0524	4.583	< 0.049
58	SDSS1030+0524	4.948	0.130 ± 0.018	< 0.115
59	SDSS1030+0524	5.130	< 0.131	< 0.070
63	SDSS1305+0521	2.753	< 0.373
64	SDSS1305+0521	3.235	< 0.262	< 0.365
65	SDSS1305+0521	3.680	< 0.221	< 0.277	0.551 ± 0.064	< 0.193
68	SDSS1306+0356	4.615	0.238 ± 0.012	< 0.100
69	SDSS1306+0356	4.865	0.835 ± 0.034	< 0.106
70	SDSS1306+0356	4.882	0.922 ± 0.029	< 0.099
71	ULAS1319+0950	4.569	< 0.073
72	SDSS1402+0146	3.277	0.500 ± 0.055	< 0.407
73	SDSS1402+0146	3.454	0.340 ± 0.046	< 0.373
76	SDSS1408+0205	2.462	< 0.374
79	SDSS1411+1217	4.929	$< 0.344^c$...
80	SDSS1411+1217	5.055	0.102 ± 0.012	< 0.054	< 0.059	< 0.074
81	SDSS1411+1217	5.250	0.259 ± 0.016	0.257 ± 0.032	< 0.080	< 0.143
82	SDSS1411+1217	5.332	0.090 ± 0.027	0.094 ± 0.024	< 0.051	< 0.130
83	Q1422+2309	3.540	$< 0.144^c$	0.007 ± 0.001	0.306 ± 0.004	0.133 ± 0.003	0.026 ± 0.002	...
88	SDSS1538+0855	2.638	0.113 ± 0.020	< 0.078
89	SDSS1538+0855	3.498	0.095 ± 0.028	< 0.101	< 0.062	< 0.066	< 0.084	< 0.110
91	SDSS1616+0501	3.275	< 0.320
92	SDSS1616+0501	3.396	< 0.415
93	SDSS1616+0501	3.450	< 0.281
94	SDSS1616+0501	3.733	0.474 ± 0.048	...
96	SDSS1620+0020	3.273	< 0.325	...
97	SDSS1620+0020	3.620	0.787 ± 0.082	0.398 ± 0.084
98	SDSS1620+0020	3.752	$< 1.507^c$	< 0.195	0.483 ± 0.111	< 0.215
99	SDSS1621-0042	2.678	< 0.113
100	SDSS1621-0042	3.106	0.626 ± 0.012	0.394 ± 0.017	0.365 ± 0.028	< 0.145
102	SDSS2228-0757	3.175	< 0.375
110	BR2346-3729	3.692	< 0.109

^a Upper limits are 3σ .

^b Suspected false positive.

^c Blended line.

Table 8
Absorption Properties for the FIRE Mg II-Selected Sample: C and Al Ions

Index #	Sightline	z	$W_0^{\lambda 1334a}$ (Å)	$W_0^{\lambda 1548a}$ (Å)	$W_0^{\lambda 1550a}$ (Å)	$W_0^{\lambda 1670a}$ (Å)	$W_0^{\lambda 1854a}$ (Å)	$W_0^{\lambda 1862a}$ (Å)
2	Q0000–26	3.390	...	0.959 ± 0.012	0.797 ± 0.012	0.290 ± 0.018	0.087 ± 0.023	0.101 ± 0.025
7	BR0004–6224	3.694	< 0.205	< 0.238
8	BR0004–6224	3.776	< 0.208	< 0.201
12	BR0016–3544	3.757	< 0.111	< 0.096
13	SDSS0106+0048	3.729	...	0.989 ± 0.106	0.879 ± 0.084	0.464 ± 0.097	0.089 ± 0.028	< 0.080
14 ^b	SDSS0113–0935	2.825	...	< 0.161	< 0.165	< 0.170	< 0.143	< 0.152
15	SDSS0113–0935	3.544	< 0.123	0.288 ± 0.036	0.203 ± 0.043	< 0.181	< 0.063	< 0.079
16	SDSS0113–0935	3.617	0.388 ± 0.055	0.704 ± 0.042	0.390 ± 0.037	< 0.370	< 0.095	< 0.075
17	SDSS0127–0045	2.588	0.184 ± 0.056	< 0.169
18	SDSS0127–0045	2.945	0.723 ± 0.052	< 0.472 ^c	< 0.236
19	SDSS0127–0045	3.168	...	0.718 ± 0.040	0.335 ± 0.039	< 0.144	< 0.140	< 0.160
20	SDSS0127–0045	3.728	0.489 ± 0.024	0.386 ± 0.077	< 0.197	0.218 ± 0.038	< 0.066	< 0.075
21	SDSS0140–0839	2.241	0.197 ± 0.035	< 0.429 ^c
22	SDSS0140–0839	3.081	...	0.746 ± 0.011	0.490 ± 0.011	0.213 ± 0.008	0.036 ± 0.007	...
23	SDSS0140–0839	3.212	...	< 0.026	< 0.026	0.023 ± 0.006	< 0.031	0.036 ± 0.010
26	SDSS0203+0012	4.482	...	0.428 ± 0.141	< 0.802	...	< 0.308	< 0.493
27	SDSS0203+0012	4.978	...	< 0.333	< 0.308	0.255 ± 0.085	< 0.351	< 0.279
30	BR0305–4957	3.354	< 1.744 ^c	< 0.046
31	BR0305–4957	3.591	...	0.211 ± 0.008	< 0.582 ^c	< 1.021 ^c	< 0.056	< 0.057
32	BR0305–4957	4.466	0.746 ± 0.010	0.521 ± 0.019	0.332 ± 0.019	0.565 ± 0.021	0.070 ± 0.011	< 0.042
34	SDSS0332–0654	3.061	...	< 0.599	< 1.214	< 0.985	< 0.803	< 0.808
36	BR0331–1622	2.593	0.040 ± 0.006	< 0.020
37	BR0331–1622	2.927	0.346 ± 0.010	0.219 ± 0.030	0.229 ± 0.026
38	BR0331–1622	3.557	...	0.085 ± 0.010	0.046 ± 0.011	...	< 0.086	< 0.105
41	BR0353–3820	2.754	0.909 ± 0.006	0.495 ± 0.006
43	BR0418–5723	2.978	0.139 ± 0.007	0.102 ± 0.007
45	SDSS0818+1722	4.431	0.082 ± 0.021	< 0.048	< 0.049
46	SDSS0818+1722	5.065	0.141 ± 0.016
48	SDSS0836+0054	3.744	< 0.500 ^c	0.168 ± 0.024
50	SDSS0949+0335	3.310	...	0.365 ± 0.028	0.158 ± 0.031	0.574 ± 0.034	< 0.243	< 0.247
51	SDSS1020+0922	2.046	0.239 ± 0.011
52	SDSS1020+0922	2.593	0.273 ± 0.012	< 0.041	0.041 ± 0.012
53	SDSS1020+0922	2.749	...	0.067 ± 0.011	0.042 ± 0.013	0.138 ± 0.010	< 0.039	< 0.039
54	SDSS1020+0922	3.479	0.039 ± 0.010	0.365 ± 0.010	0.271 ± 0.013	0.042 ± 0.012	< 0.086	< 0.080
57	SDSS1030+0524	4.583	0.964 ± 0.076	< 0.105	< 0.101
58	SDSS1030+0524	4.948	...	0.177 ± 0.021	0.208 ± 0.022	0.056 ± 0.015	< 0.086	< 0.065
59	SDSS1030+0524	5.130	...	0.226 ± 0.033	< 0.215	< 0.051
63	SDSS1305+0521	2.753	< 0.135	< 0.267	< 0.368
64	SDSS1305+0521	3.235	...	< 0.262	< 0.234	< 0.311	< 2.125	< 2.063 ^c
65	SDSS1305+0521	3.680	0.694 ± 0.045	< 0.411	< 0.281	0.426 ± 0.131	< 0.205	< 0.203
68	SDSS1306+0356	4.615	...	0.341 ± 0.014	0.206 ± 0.013	< 0.146	< 0.064	< 0.065
69	SDSS1306+0356	4.865	...	1.336 ± 0.045	0.628 ± 0.045	0.929 ± 0.055	0.061 ± 0.016	< 0.121
70	SDSS1306+0356	4.882	...	0.416 ± 0.038	0.329 ± 0.041	0.807 ± 0.040	< 0.038	< 0.054
71	ULAS1319+0950	4.569	< 0.076	0.139 ± 0.033	< 0.166
72	SDSS1402+0146	3.277	...	< 0.158	< 0.170	0.390 ± 0.057	< 0.225	< 0.312
73	SDSS1402+0146	3.454	...	< 0.180	< 0.143	0.288 ± 0.086	< 0.258	< 0.459
76	SDSS1408+0205	2.462	< 0.251	< 0.221
79	SDSS1411+1217	4.929	...	0.692 ± 0.048	0.359 ± 0.037	0.081 ± 0.023
80	SDSS1411+1217	5.055	< 0.055	< 0.055	< 0.087
81	SDSS1411+1217	5.250	...	0.739 ± 0.023	0.324 ± 0.022	0.061 ± 0.014	< 0.240	< 0.077
82	SDSS1411+1217	5.332	0.074 ± 0.010	< 0.121	< 0.112	< 0.033	< 0.054	< 0.046
83	Q1422+2309	3.540	0.094 ± 0.002	0.538 ± 0.002	0.275 ± 0.002	...	< 0.029	< 0.030
84	SDSS1433+0227	2.772	0.185 ± 0.043	0.139 ± 0.045
88	SDSS1538+0855	2.638	...	0.702 ± 0.020	0.244 ± 0.025	< 0.070	< 0.081	< 0.082
89	SDSS1538+0855	3.498	...	0.133 ± 0.022	< 0.070	< 0.071	< 0.050	< 0.052
91	SDSS1616+0501	3.275	< 0.312	< 0.437
92	SDSS1616+0501	3.396	< 1.147 ^c	0.259 ± 0.086	< 0.286
93	SDSS1616+0501	3.450	< 0.244	< 0.270	< 0.474
94	SDSS1616+0501	3.733	...	0.508 ± 0.079	< 0.247	0.266 ± 0.084	< 0.248	< 0.225
95	SDSS1620+0020	2.910	< 0.454	< 0.580 ^c	< 1.846
96	SDSS1620+0020	3.273	...	0.782 ± 0.109	0.854 ± 0.108	...	< 0.321	< 0.455
97	SDSS1620+0020	3.620	...	1.349 ± 0.085	0.956 ± 0.084	...	0.429 ± 0.104	0.247 ± 0.070
98	SDSS1620+0020	3.752	0.881 ± 0.041	< 0.523	< 0.712	0.849 ± 0.108	< 0.294	< 0.301
99	SDSS1621–0042	2.678	< 0.070	< 0.081	< 0.078
100	SDSS1621–0042	3.106	...	1.068 ± 0.035	0.846 ± 0.043	0.363 ± 0.031	< 0.191	0.199 ± 0.034
102	SDSS2228–0757	3.175	< 0.562	< 0.741
109	BR2346–3729	3.619	< 0.136	< 0.118
110	BR2346–3729	3.692	< 0.089	< 0.108

^a Upper limits are 3σ .^b Suspected false positive.^c Blended line.

Table 9
Kinematic Properties, FIRE sample

Index	Sightline	z	$\Delta v_{\lambda 2796}$ (km s ⁻¹)	$\omega_{\lambda 2796}$ (km s ⁻¹)	$\Delta v_{\lambda 2600}$ (km s ⁻¹)	$\omega_{\lambda 2600}$ (km s ⁻¹)	$\Delta v_{\lambda 1548}$ (km s ⁻¹)	$\omega_{\lambda 1548}$ (km s ⁻¹)
1 ^a	Q0000-26	2.184	175.2 ± 17.5	61.2 ± 8.6
2	Q0000-26	3.390	262.7 ± 26.3	52.2 ± 1.1	150.1 ± 15.0	36.0 ± 1.0	290.1 ± 29.0	78.7 ± 1.2
3	BR0004-6224	2.663	62.6 ± 8.8	34.1 ± 5.6
4	BR0004-6224	2.908	112.6 ± 11.3	40.1 ± 3.7
5	BR0004-6224	2.959	125.1 ± 12.5	26.4 ± 3.7	150.1 ± 15.0	36.7 ± 2.7
6	BR0004-6224	3.203	100.1 ± 10.0	29.1 ± 1.6	100.1 ± 10.0 ^b	29.8 ± 4.2 ^b
7	BR0004-6224	3.694	100.1 ± 10.0	32.7 ± 4.8
8	BR0004-6224	3.776	175.2 ± 17.5	43.8 ± 2.5 ^c	125.1 ± 12.5	32.5 ± 1.5
9	BR0016-3544	2.783	125.1 ± 12.5	39.6 ± 1.8
10	BR0016-3544	2.819	575.4 ± 57.5	153.2 ± 30.1	725.5 ± 72.6	140.8 ± 3.5
11	BR0016-3544	2.949	75.1 ± 8.8	26.5 ± 3.4
12	BR0016-3544	3.757	537.8 ± 53.8	136.3 ± 3.0	325.3 ± 32.5	94.2 ± 3.5
13	SDSS0106+0048	3.729	212.7 ± 21.3	43.4 ± 0.8	125.1 ± 12.5	35.6 ± 1.7
14 ^a	SDSS0113-0935	2.825	87.6 ± 8.8	34.9 ± 4.0
15	SDSS0113-0935	3.544	125.1 ± 12.5	45.8 ± 5.3
16	SDSS0113-0935	3.617	162.7 ± 16.3	41.5 ± 1.5
17	SDSS0127-0045	2.588	475.4 ± 47.5	131.8 ± 1.8	412.8 ± 41.3	145.8 ± 17.1
18	SDSS0127-0045	2.945	538.0 ± 53.8	127.8 ± 2.8	437.9 ± 43.8	106.9 ± 6.8
19	SDSS0127-0045	3.168	225.2 ± 22.5	73.9 ± 4.4
20	SDSS0127-0045	3.728	187.6 ± 18.8	35.3 ± 0.6	187.6 ± 18.8	40.1 ± 0.8
21	SDSS0140-0839	2.241	100.1 ± 10.0	30.0 ± 1.7	150.1 ± 15.0	37.1 ± 1.7
22	SDSS0140-0839	3.081	137.6 ± 13.8	30.6 ± 0.8	125.1 ± 12.5	41.1 ± 3.5	334.2 ± 33.4	86.4 ± 1.1
23	SDSS0140-0839	3.212	112.6 ± 11.3	36.0 ± 4.4
24	SDSS0203+0012	3.711	125.1 ± 12.5	37.2 ± 3.1
25	SDSS0203+0012	4.313	225.2 ± 22.5	44.8 ± 3.9	175.2 ± 17.5 ^d	45.3 ± 9.5 ^d
26	SDSS0203+0012	4.482	125.1 ± 12.5	39.8 ± 11.6	100.1 ± 10.0 ^d	32.1 ± 1.9 ^d	150.1 ± 15.0
27	SDSS0203+0012	4.978	137.6 ± 13.8	41.8 ± 2.1	125.1 ± 12.5	35.1 ± 2.4 ^b
28	BR0305-4957	2.502	137.6 ± 13.8	43.9 ± 2.6
29	BR0305-4957	2.629	237.7 ± 23.8	51.8 ± 0.8	250.2 ± 25.0 ^d	60.3 ± 1.3 ^d
30	BR0305-4957	3.354	150.1 ± 15.0	34.7 ± 0.7	137.6 ± 13.8 ^d	33.2 ± 2.0 ^d
31	BR0305-4957	3.591	287.7 ± 28.8	50.4 ± 0.8	200.2 ± 20.0	37.5 ± 0.5	224.1 ± 22.4	55.4 ± 1.5
32	BR0305-4957	4.466	312.7 ± 31.3	61.0 ± 0.9 ^c	262.7 ± 26.3 ^d	63.2 ± 0.9 ^d	400.3 ± 40.0	83.6 ± 2.4
33	BR0322-2928	2.229	112.6 ± 11.3	34.1 ± 1.2	212.7 ± 21.3	46.5 ± 2.0
34	SDSS0332-0654	3.061	150.1 ± 15.0	55.4 ± 12.8	112.6 ± 11.3 ^d	39.9 ± 7.1 ^d
35	BR0331-1622	2.295	412.8 ± 41.3	113.8 ± 25.6	400.3 ± 40.0	118.1 ± 8.5
36	BR0331-1622	2.593	75.1 ± 8.8	25.6 ± 1.7
37	BR0331-1622	2.927	350.3 ± 35.0	91.5 ± 2.9	312.7 ± 31.3	82.7 ± 10.2
38	BR0331-1622	3.557	137.6 ± 13.8	34.3 ± 1.6	162.6 ± 16.3	30.6 ± 0.9	136.0 ± 15.6	34.9 ± 2.8
39	BR0353-3820	1.987	525.4 ± 52.5	117.3 ± 2.9	491.3 ± 49.1	138.3 ± 0.9
40	BR0353-3820	2.696	187.7 ± 18.8	46.6 ± 1.3
41	BR0353-3820	2.754	625.4 ± 62.5	131.0 ± 10.2	525.4 ± 52.5	128.6 ± 1.7 ^b
42	BR0418-5723	2.030	250.2 ± 25.0	54.6 ± 8.5	191.1 ± 19.1	95.8 ± 1.6
43	BR0418-5723	2.978	262.8 ± 26.3	69.9 ± 22.8	300.3 ± 30.0	57.1 ± 11.7
44	SDSS0818+1722	3.563	162.6 ± 16.3	40.6 ± 4.3	125.1 ± 12.5	27.5 ± 1.4
45	SDSS0818+1722	4.431	125.1 ± 12.5	39.2 ± 4.6
46	SDSS0818+1722	5.065	212.7 ± 21.3	52.4 ± 2.5	150.1 ± 15.0	43.2 ± 2.1
47	SDSS0836+0054	2.299	137.6 ± 13.8	45.2 ± 1.8
48	SDSS0836+0054	3.744	487.9 ± 48.8	100.3 ± 8.5	325.3 ± 32.5	89.8 ± 3.9
49	SDSS0949+0335	2.289	425.3 ± 42.5	114.3 ± 17.8	225.2 ± 22.5	70.9 ± 16.4 ^b
50	SDSS0949+0335	3.310	375.3 ± 37.5	64.7 ± 20.9	125.1 ± 12.5	40.4 ± 1.3
51	SDSS1020+0922	2.046	112.6 ± 11.3	28.8 ± 2.6	114.0 ± 15.6	50.5 ± 4.8
52	SDSS1020+0922	2.593	175.2 ± 17.5	32.3 ± 1.2	100.1 ± 10.0 ^b	27.2 ± 1.4 ^b
53	SDSS1020+0922	2.749	187.7 ± 18.8	35.1 ± 1.1	200.2 ± 20.0	48.9 ± 3.3	158.0 ± 15.8	47.1 ± 6.0
54	SDSS1020+0922	3.479	87.6 ± 8.8	28.4 ± 2.8	224.2 ± 22.4	62.1 ± 1.3
55	SDSS1030+0524	2.188	137.7 ± 13.8	54.9 ± 2.1
56	SDSS1030+0524	2.780	587.9 ± 58.8	166.4 ± 15.2	550.4 ± 55.0	170.9 ± 14.5
57	SDSS1030+0524	4.583	387.8 ± 38.8	79.2 ± 1.8	387.8 ± 38.8 ^d	83.8 ± 3.6 ^d
58	SDSS1030+0524	4.948	150.1 ± 15.0	38.0 ± 1.2	200.1 ± 20.0	65.8 ± 12.1	150.1 ± 15.0	39.8 ± 2.9
59	SDSS1030+0524	5.130	75.1 ± 8.8	33.9 ± 2.3	212.7 ± 21.3	81.1 ± 8.7
60	SDSS1110+0244	2.119	462.9 ± 46.3	107.4 ± 17.6	444.2 ± 44.4	104.5 ± 16.5

Table 9
Kinematic Properties, FIRE sample (*Continued*)

Index	Sightline	z	$\Delta v_{\lambda 2796}$ (km s ⁻¹)	$\omega_{\lambda 2796}$ (km s ⁻¹)	$\Delta v_{\lambda 2600}$ (km s ⁻¹)	$\omega_{\lambda 2600}$ (km s ⁻¹)	$\Delta v_{\lambda 1548}$ (km s ⁻¹)	$\omega_{\lambda 1548}$ (km s ⁻¹)
61	SDSS1110+0244	2.223	137.6 ± 13.8	36.7 ± 3.1
62	SDSS1305+0521	2.302	237.7 ± 23.8	200.2 ± 20.0
63	SDSS1305+0521	2.753	162.6 ± 16.3	41.1 ± 3.3
64	SDSS1305+0521	3.235	125.1 ± 12.5	34.6 ± 2.0	150.2 ± 15.0 ^d	37.3 ± 9.5 ^d
65	SDSS1305+0521	3.680	387.9 ± 38.8	83.3 ± 12.2	175.1 ± 17.5	42.6 ± 14.1
66	SDSS1306+0356	2.533	587.9 ± 58.8	562.9 ± 56.3	117.9 ± 15.4
67	SDSS1306+0356	3.490	175.1 ± 17.5	45.8 ± 1.8	175.1 ± 17.5 ^d	51.3 ± 6.4 ^d
68	SDSS1306+0356	4.615	225.2 ± 22.5	45.4 ± 7.9	137.6 ± 13.8 ^d	28.0 ± 1.9 ^d	300.2 ± 30.0	59.9 ± 1.8
69	SDSS1306+0356	4.865	412.8 ± 41.3	102.9 ± 16.6	412.9 ± 41.3	134.4 ± 21.2	412.8 ± 41.3	132.0 ± 5.5
70	SDSS1306+0356	4.882	237.7 ± 23.8	69.5 ± 8.2	325.2 ± 32.5	81.9 ± 1.8 ^b	150.1 ± 15.0	90.9 ± 8.1
71	ULAS1319+0950	4.569	112.6 ± 11.3	33.2 ± 5.1	87.6 ± 8.8 ^d	24.0 ± 3.2 ^d
72	SDSS1402+0146	3.277	200.2 ± 20.0	36.1 ± 2.6	175.2 ± 17.5	37.6 ± 1.6
73	SDSS1402+0146	3.454	175.1 ± 17.5	57.9 ± 2.1	112.6 ± 11.3 ^e	40.0 ± 7.2 ^e
74	SDSS1408+0205	1.982	262.7 ± 26.3	65.6 ± 18.7
75	SDSS1408+0205	1.991	125.1 ± 12.5	38.5 ± 2.8 ^c
76	SDSS1408+0205	2.462	237.7 ± 23.8	47.9 ± 4.6	275.2 ± 27.5	56.5 ± 3.6
77	SDSS1411+1217	2.237	175.2 ± 17.5	44.2 ± 2.6
78	SDSS1411+1217	3.477	62.6 ± 8.8	25.4 ± 1.1
79	SDSS1411+1217	4.929	300.3 ± 30.0	76.8 ± 1.9	250.2 ± 25.0	71.1 ± 4.0	350.1 ± 35.0	111.4 ± 6.6
80	SDSS1411+1217	5.055	62.6 ± 8.8	25.5 ± 1.3
81	SDSS1411+1217	5.250	150.1 ± 15.0	33.8 ± 1.0	250.2 ± 25.0	70.4 ± 2.4
82	SDSS1411+1217	5.332	87.6 ± 8.8	22.7 ± 1.1
83	Q1422+2309	3.540	412.7 ± 41.3	154.8 ± 5.5	441.0 ± 44.1	172.0 ± 0.5
84	SDSS1433+0227	2.772	137.6 ± 13.8	28.8 ± 1.0	162.6 ± 16.3	38.6 ± 2.5
85	CFQS1509-1749	3.128	225.2 ± 22.5	69.7 ± 6.1	200.2 ± 20.0	66.6 ± 7.6
86	CFQS1509-1749	3.266	187.7 ± 18.8	44.8 ± 1.0	175.2 ± 17.5	40.0 ± 3.8
87	CFQS1509-1749	3.392	713.1 ± 71.3	166.7 ± 29.9	700.6 ± 70.1	115.6 ± 12.4 ^b
88	SDSS1538+0855	2.638	150.1 ± 15.0	36.3 ± 2.7	237.7 ± 23.8 ^d	100.8 ± 6.5 ^d
89	SDSS1538+0855	3.498	162.7 ± 16.3	60.9 ± 3.1
90	SDSS1616+0501	2.741	175.2 ± 17.5	40.2 ± 3.4 ^c	237.7 ± 23.8 ^b	113.5 ± 16.5 ^b
91	SDSS1616+0501	3.275	112.6 ± 11.3	42.1 ± 2.4
92	SDSS1616+0501	3.396	100.1 ± 10.0	32.3 ± 10.1 ^c	200.2 ± 20.0	46.3 ± 3.6
93	SDSS1616+0501	3.450	100.1 ± 10.0	33.1 ± 1.9	137.6 ± 13.8 ^d	60.5 ± 8.7 ^d
94	SDSS1616+0501	3.733	262.7 ± 26.3	64.6 ± 8.0 ^c	262.8 ± 26.3 ^f	99.9 ± 17.5 ^f
95	SDSS1620+0020	2.910	275.2 ± 27.5	55.4 ± 5.1	150.1 ± 15.0	57.7 ± 9.4
96	SDSS1620+0020	3.273	225.2 ± 22.5	42.0 ± 7.7	137.6 ± 13.8	43.9 ± 8.2
97	SDSS1620+0020	3.620	337.8 ± 33.8	81.9 ± 4.1
98	SDSS1620+0020	3.752	362.8 ± 36.3	94.5 ± 4.3	375.3 ± 37.5	84.8 ± 10.6
99	SDSS1621-0042	2.678	100.1 ± 10.0	30.3 ± 2.2
100	SDSS1621-0042	3.106	112.6 ± 11.3	37.9 ± 1.0 ^c	337.8 ± 33.8	74.1 ± 2.1
101	SDSS2147-0838	2.286	175.2 ± 17.5	46.9 ± 2.3	237.7 ± 23.8	73.7 ± 11.3
102	SDSS2228-0757	3.175	50.1 ± 8.8	21.9 ± 2.3
103	SDSS2310+1855	2.243	325.3 ± 32.5	82.2 ± 2.8
104	SDSS2310+1855	2.351	250.2 ± 25.0	61.7 ± 2.7	187.7 ± 18.8	44.4 ± 2.5
105	SDSS2310+1855	2.643	200.2 ± 20.0	45.1 ± 1.6	187.6 ± 18.8	51.8 ± 6.9
106	SDSS2310+1855	3.300	250.2 ± 25.0	59.8 ± 3.0
107	BR2346-3729	2.830	225.2 ± 22.5	52.5 ± 9.9	225.2 ± 22.5	59.9 ± 3.0
108	BR2346-3729	2.923	150.1 ± 15.0	40.2 ± 1.8	112.6 ± 11.3	31.3 ± 4.0
109	BR2346-3729	3.619	137.6 ± 13.8	41.0 ± 2.3
110	BR2346-3729	3.692	100.1 ± 10.0	29.8 ± 1.0	112.6 ± 11.3	35.6 ± 5.0

^a Suspected false positive.

^b FeII 2586.

^c MgII 2803.

^d FeII 2382.

^e FeII 2374.

^f FeII 2344.

Table 10
Comparison Samples Statistics: Two Redshift Bins

Ion	\bar{z}	Detections	Upper Limits ^{ab}	Min W_{Ion} (Å)	Max W_{Ion} (Å)
Low Redshift, $0 < z < 2$					
HI 1215	0.864	18	2 (1)	1.09 ± 0.000	11.95 ± 0.26
MgII 2796	1.128	272	0	0.30 ± 0.04	5.80 ± 0.08
MgI 2852	1.128	46	214 (5)	< 0.05	1.36 ± 0.11
FeII 2374	1.215	36	137 (5)	< 0.07	2.14 ± 0.08
FeII 2586	1.190	66	139 (3)	< 0.03	2.60 ± 0.14
FeII 2600	1.173	94	122 (5)	< 0.03	3.38 ± 0.11
CII 1334	1.211	23	9 (2)	< 0.14	3.00 ± 0.08
CIV 1548	1.255	36	12	0.13 ± 0.02	2.13 ± 0.11
CIV 1550	1.322	24	17 (5)	0.21 ± 0.02	1.53 ± 0.10
SiII 1526	1.276	17	20	< 0.07	2.04 ± 0.12
SiIV 1393	1.237	20	15 (2)	< 0.14	1.42 ± 0.07
SiIV 1402	1.366	14	13	< 0.12	1.02 ± 0.07
AlII 1670	1.117	17	32 (2)	0.12 ± 0.01	2.32 ± 0.20
AlIII 1854	1.209	13	37	< 0.05	0.66 ± 0.03
High Redshift, $z \geq 2$					
HI 1215	3.402	27	0	1.80 ± 0.17	36.71 ± 1.09
MgII 2796	3.184	97	0	0.30 ± 0.04	5.58 ± 0.07
MgI 2852	3.174	13	73	0.02 ± 0.004	1.57 ± 0.04
FeII 2374	3.123	22	59 (5)	< 0.03	1.40 ± 0.02
FeII 2586	3.130	36	47 (2)	< 0.06	2.47 ± 0.02
FeII 2600	3.147	49	32 (3)	< 0.07	3.38 ± 0.02
CII 1334	3.360	8	0	0.09 ± 0.002	0.89 ± 0.02
CIV 1548	3.647	24	8	0.07 ± 0.01	1.35 ± 0.08
CIV 1550	3.647	19	13 (1)	< 0.05	0.96 ± 0.08
SiII 1526	3.728	21	7 (2)	0.03 ± 0.002	0.92 ± 0.03
SiIV 1393	3.439	7	3 (2)	0.13 ± 0.02	0.79 ± 0.08
SiIV 1402	3.533	5	6 (1)	< 0.13	0.58 ± 0.04
AlII 1670	3.693	18	20 (2)	< 0.07	0.96 ± 0.08
AlIII 1854	3.438	7	49 (4)	0.04 ± 0.007	0.91 ± 0.01
SDSS, $0.36 < z < 2$					
MgII 2796	1.064	1975	0	0.30 ± 0.06	4.44 ± 0.69
MgI 2852	1.050	28	1900	< 0.16	3.47 ± 0.11
FeII 2374	1.128	37	1651	< 0.13	1.60 ± 0.31
FeII 2586	1.054	97	1747	0.16 ± 0.03	2.21 ± 0.27
FeII 2600	1.078	216	1702	< 0.17	3.83 ± 0.18
CII 1334	1.921	5	6	< 0.24	1.93 ± 0.33
CIV 1548	1.622	127	208	< 0.15	3.46 ± 0.28
CIV 1550	1.615	87	169	< 0.18	1.71 ± 0.15
SiII 1526	1.712	20	47	< 0.15	1.35 ± 0.18
SiIV 1393	1.867	16	13	0.20 ± 0.04	1.98 ± 0.28
SiIV 1402	1.861	6	14	< 0.16	0.95 ± 0.16
AlII 1670	1.430	42	346	0.14 ± 0.03	1.60 ± 0.14
AlIII 1854	1.292	5	596	< 0.05	1.21 ± 0.14

^a Upper Limits are 5σ .

^b Values in parentheses are upper limits derived from blended lines.

Table 11
Comparison Samples Statistics: Three Redshift Bins

Ion	\bar{z}	Detections	Upper Limits ^{ab}	Min W_{Ion} (Å)	Max W_{Ion} (Å)
Low Redshift, $0 < z < 1.5$					
HI 1215	0.752	17	1	1.09 ± 0.000	11.15 ± 1.09
MgII 2796	0.968	217	0	0.30 ± 0.04	4.68 ± 0.38
MgI 2852	0.973	37	172 (3)	< 0.05	1.36 ± 0.11
FeII 2374	1.008	26	101 (2)	< 0.07	1.09 ± 0.00
FeII 2586	0.997	47	107 (3)	< 0.03	1.90 ± 0.02
FeII 2600	0.985	67	97 (4)	< 0.03	2.94 ± 0.27
CII 1334	0.736	12	6	0.23 ± 0.001	1.50 ± 0.06
CIV 1548	0.857	17	10	< 0.13	1.60 ± 0.26
CIV 1550	0.887	12	9	0.21 ± 0.02	1.23 ± 0.00
SiII 1526	0.883	9	12	0.10 ± 0.01	1.01 ± 0.20
SiIV 1393	0.810	10	10	0.20 ± 0.03	0.70 ± 0.04
SiIV 1402	0.875	6	7	0.17 ± 0.02	0.30 ± 0.06
AlII 1670	0.834	12	22 (1)	0.12 ± 0.01	1.25 ± 0.21
AlIII 1854	0.883	5	27	0.16 ± 0.03	0.36 ± 0.02
Mid Redshift, $1.5 \leq z < 3$					
HI 1215	2.405	4	1 (1)	8.04 ± 0.07	24.21 ± 0.16
MgII 2796	2.092	100	0	0.32 ± 0.02	5.80 ± 0.08
MgI 2852	2.091	16	76 (2)	< 0.05	1.29 ± 0.03
FeII 2374	2.117	20	63 (6)	< 0.09	2.14 ± 0.08
FeII 2586	2.098	35	56 (1)	< 0.08	2.60 ± 0.14
FeII 2600	2.084	51	39 (2)	< 0.07	3.38 ± 0.02
CII 1334	1.851	13	3 (2)	< 0.14	3.00 ± 0.08
CIV 1548	1.839	22	3	0.07 ± 0.01	2.13 ± 0.11
CIV 1550	1.852	14	10 (5)	< 0.06	1.53 ± 0.10
SiII 1526	1.870	11	8	< 0.07	2.04 ± 0.12
SiIV 1393	1.834	12	5 (2)	0.13 ± 0.02	1.42 ± 0.07
SiIV 1402	1.851	9	7	< 0.12	1.02 ± 0.07
AlII 1670	2.059	11	12 (1)	< 0.12	2.32 ± 0.20
AlIII 1854	2.148	13	21 (2)	< 0.05	0.91 ± 0.01
High Redshift, $z \geq 3$					
HI 1215	3.482	24	0	1.80 ± 0.17	36.71 ± 1.09
MgII 2796	3.780	52	0	0.30 ± 0.04	5.58 ± 0.07
MgI 2852	3.787	6	39	0.02 ± 0.004	1.57 ± 0.04
FeII 2374	3.623	12	32 (2)	< 0.03	0.75 ± 0.06
FeII 2586	3.703	20	23 (1)	< 0.06	1.42 ± 0.08
FeII 2600	3.703	25	18 (2)	< 0.07	3.30 ± 0.04
CII 1334	3.797	6	0	0.09 ± 0.002	0.88 ± 0.04
CIV 1548	3.851	21	7	0.08 ± 0.01	1.35 ± 0.08
CIV 1550	3.851	17	11 (1)	< 0.05	0.96 ± 0.08
SiII 1526	3.902	18	7 (2)	0.03 ± 0.002	0.92 ± 0.03
SiIV 1393	3.786	5	3 (2)	0.26 ± 0.02	0.79 ± 0.08
SiIV 1402	3.862	4	5 (1)	0.13 ± 0.003	0.58 ± 0.04
AlII 1670	3.978	12	18 (2)	< 0.07	0.96 ± 0.08
AlIII 1854	3.793	2	38 (2)	0.04 ± 0.007	0.07 ± 0.01

^a Upper Limits are 5σ .

^b Values in parentheses are upper limits derived from blended lines.

Table 12
Weak and Strong $W_0^{\lambda 2796}$ Comparison Samples Statistics

Ion	\bar{z}	Detections	Upper Limits ^{a,b}	Min W_{Ion}^{λ} (\AA)	Max W_{Ion}^{λ} (\AA)
$0.3\text{\AA} \leq W_0^{\lambda 2796} \leq 1.0\text{\AA}$					
HI 1215	2.805	21	0	1.09 ± 0.000	26.94 ± 0.36
MgII 2796	2.129	119	0	0.30 ± 0.04	0.99 ± 0.00
MgI 2852	2.116	8	108 (2)	0.02 ± 0.004	0.32 ± 0.04
FeII 2374	2.283	11	77 (3)	< 0.03	0.59 ± 0.05
FeII 2586	2.204	24	70 (1)	< 0.06	0.75 ± 0.04
FeII 2600	2.188	36	58 (2)	< 0.07	0.65 ± 0.02
CII 1334	1.757	7	2	0.09 ± 0.002	0.84 ± 0.00
CIV 1548	2.519	27	9	0.07 ± 0.01	1.38 ± 0.03
CIV 1550	2.547	22	13 (1)	< 0.05	1.00 ± 0.10
SiII 1526	2.733	16	12 (2)	0.03 ± 0.002	0.40 ± 0.03
SiIV 1393	2.092	10	3 (1)	< 0.14	0.63 ± 0.01
SiIV 1402	2.291	8	3	0.13 ± 0.003	0.58 ± 0.04
AlII 1670	2.782	8	27 (1)	< 0.07	0.36 ± 0.03
AlIII 1854	2.744	3	42 (1)	0.04 ± 0.007	0.20 ± 0.04
$W_0^{\lambda 2796} > 1.0\text{\AA}$					
HI 1215	2.934	13	0	2.47 ± 0.08	36.71 ± 1.09
MgII 2796	2.191	75	0	1.01 ± 0.03	5.58 ± 0.07
MgI 2852	2.039	24	41	< 0.07	1.57 ± 0.04
FeII 2374	2.262	26	33 (2)	< 0.09	1.70 ± 0.15
FeII 2586	2.232	36	28 (2)	0.13 ± 0.02	2.47 ± 0.02
FeII 2600	2.180	48	18 (1)	< 0.15	3.38 ± 0.02
CII 1334	2.133	11	1 (1)	0.19 ± 0.000	1.50 ± 0.06
CIV 1548	2.720	17	4	< 0.13	1.60 ± 0.26
CIV 1550	2.810	10	10 (3)	< 0.13	1.23 ± 0.00
SiII 1526	2.645	15	4	< 0.12	1.01 ± 0.20
SiIV 1393	2.000	6	7 (2)	0.13 ± 0.02	0.79 ± 0.08
SiIV 1402	2.412	3	9 (1)	< 0.12	0.54 ± 0.02
AlII 1670	2.725	16	9 (3)	< 0.12	0.96 ± 0.08
AlIII 1854	3.008	7	23 (3)	< 0.06	0.91 ± 0.01

^a Upper Limits are 5σ .

^b Values in parentheses are upper limits derived from blended lines.

Table 13
Weak and Strong $W_0^{\lambda 2796}$ Comparison Samples Statistics

Ion	\bar{z}	Detections	Upper Limits ^{a,b}	Min W_{Ion}^{λ} (\AA)	Max W_{Ion}^{λ} (\AA)
$0.3\text{\AA} \leq W_0^{\lambda 2796} \leq 1.0\text{\AA}, z < 2$					
HI 1215	0.764	11	1	1.09 ± 0.000	11.15 ± 1.09
MgII 2796	1.069	170	0	0.30 ± 0.04	1.00 ± 0.06
MgI 2852	1.063	12	151 (4)	< 0.05	0.40 ± 0.07
FeII 2374	1.144	9	98 (4)	< 0.07	0.59 ± 0.05
FeII 2586	1.112	23	105 (2)	< 0.03	0.64 ± 0.13
FeII 2600	1.108	35	98 (4)	< 0.03	0.88 ± 0.04
CII 1334	0.991	10	6	< 0.14	0.84 ± 0.00
CIV 1548	1.160	19	10	0.13 ± 0.02	1.38 ± 0.03
CIV 1550	1.173	15	11 (2)	0.21 ± 0.02	1.07 ± 0.04
SiII 1526	1.086	7	15	< 0.07	0.40 ± 0.03
SiIV 1393	1.062	11	7	< 0.14	1.18 ± 0.04
SiIV 1402	1.083	7	8	< 0.14	0.38 ± 0.02
AlII 1670	1.031	6	23	0.12 ± 0.01	0.96 ± 0.00
AlIII 1854	1.114	7	24	< 0.05	0.36 ± 0.02
$0.3\text{\AA} \leq W_0^{\lambda 2796} \leq 1.0\text{\AA}, z \geq 2$					
HI 1215	3.300	17	0	1.80 ± 0.17	26.94 ± 0.36
MgII 2796	3.280	57	0	0.30 ± 0.04	0.98 ± 0.08
MgI 2852	3.289	4	51	0.02 ± 0.004	0.19 ± 0.04
FeII 2374	3.257	6	41 (3)	< 0.03	0.41 ± 0.03
FeII 2586	3.213	14	34 (1)	< 0.06	0.75 ± 0.04
FeII 2600	3.226	23	24 (2)	< 0.07	0.65 ± 0.02
CII 1334	3.628	3	0	0.09 ± 0.002	0.49 ± 0.02
CIV 1548	3.686	15	4	0.07 ± 0.01	1.07 ± 0.03
CIV 1550	3.686	12	7	< 0.05	0.88 ± 0.08
SiII 1526	3.820	11	6 (2)	0.03 ± 0.002	0.36 ± 0.03
SiIV 1393	3.848	4	1 (1)	0.26 ± 0.02	0.63 ± 0.01
SiIV 1402	3.848	4	1	0.13 ± 0.003	0.58 ± 0.04
AlII 1670	3.814	6	16 (1)	< 0.07	0.36 ± 0.03
AlIII 1854	3.451	2	30 (1)	0.04 ± 0.007	0.20 ± 0.04
$W_0^{\lambda 2796} > 1.0\text{\AA}, z < 2$					
HI 1215	1.013	7	1 (1)	2.47 ± 0.08	11.95 ± 0.26
MgII 2796	1.228	102	0	1.00 ± 0.20	5.80 ± 0.08
MgI 2852	1.236	34	63 (1)	< 0.09	1.36 ± 0.11
FeII 2374	1.330	27	39 (1)	< 0.10	2.14 ± 0.08
FeII 2586	1.319	43	34 (1)	0.17	2.60 ± 0.14
FeII 2600	1.279	59	24 (1)	0.24 ± 0.03	3.38 ± 0.11
CII 1334	1.432	13	3 (2)	0.16 ± 0.01	3.00 ± 0.08
CIV 1548	1.400	17	2	0.33 ± 0.000	2.13 ± 0.11
CIV 1550	1.580	9	6 (3)	0.39 ± 0.02	1.53 ± 0.10
SiII 1526	1.555	10	5	< 0.12	2.04 ± 0.12
SiIV 1393	1.422	9	8 (2)	< 0.14	1.42 ± 0.07
SiIV 1402	1.721	7	5	< 0.12	1.02 ± 0.07
AlII 1670	1.241	11	9 (2)	< 0.12	2.32 ± 0.20
AlIII 1854	1.366	6	13	0.15 ± 0.02	0.66 ± 0.03
$W_0^{\lambda 2796} > 1.0\text{\AA}, z \geq 2$					
HI 1215	3.576	10	0	6.42 ± 0.08	36.71 ± 1.09
MgII 2796	3.048	40	0	1.04 ± 0.05	5.58 ± 0.07
MgI 2852	2.970	9	22	< 0.07	1.57 ± 0.04
FeII 2374	2.938	16	18 (2)	< 0.09	1.40 ± 0.02
FeII 2586	3.016	22	13 (1)	0.13 ± 0.02	2.47 ± 0.02
FeII 2600	3.036	26	8 (1)	< 0.15	3.38 ± 0.02
CII 1334	3.200	5	0	0.62 ± 0.010	0.89 ± 0.02
CIV 1548	3.590	9	4	< 0.13	1.35 ± 0.08
CIV 1550	3.590	7	6 (1)	< 0.13	0.96 ± 0.08
SiII 1526	3.587	10	1	0.30 ± 0.02	0.92 ± 0.03
SiIV 1393	3.031	3	2 (1)	0.13 ± 0.02	0.79 ± 0.08
SiIV 1402	3.270	1	5 (1)	< 0.13	0.54 ± 0.02
AlII 1670	3.526	12	4 (1)	0.29 ± 0.02	0.96 ± 0.08
AlIII 1854	3.421	5	19 (3)	< 0.06	0.91 ± 0.01

^a Upper Limits are 5σ .

^b Values in parentheses are upper limits derived from blended lines.

Table 14
Two Sample Tests, $W_{\text{Ion}}/W_0^{\lambda 2796}$: Two Redshift Bins

Ion	Median, $0 < z < 2$	Median, $z \geq 2$	P_{LR}^a (%)	P_G^b (%)	P_{PP}^c (%)
H I 1215	2.82	8.86	< 0.1	< 0.1	< 0.1
Mg I 2852	0.15	0.07	< 0.1	< 0.1	< 0.1
Fe II 2374	0.17	0.14	4.4	2.4	1.9
Fe II 2586	0.29	0.20	1.2	1.1	0.8
Fe II 2600	0.42	0.39	38.6	51.6	47.6
C II 1334	0.54	0.42	77.5	32.1	34.0
C IV 1548	0.67	0.42	3.7	22.0	15.4
C IV 1550	0.43	0.27	0.9	9.3	5.7
Si II 1526	0.27	0.28	13.6	51.5	46.6
Si IV 1393	0.39	0.58	65.5	34.2	39.8
Al II 1670	0.24	0.27	52.8	95.6	75.5
Al III 1854	0.18	0.04	< 0.1	< 0.1	< 0.1

^a Log Rank Probability.

^b Gehan Probability.

^c Peto-Prentice Probability.

Table 15
Two Sample Tests, $W_{\text{Ion}}/W_0^{\lambda 2796}$: Three Redshift Bins

Ion	Median, $0 < z < 1.5$	Median, $1.5 \leq z < 3$	Median, $z \geq 3$	P_{LR}^{LMab} (%)	P_G^{LMcb} (%)	P_{PP}^{LMdb} (%)	P_{LR}^{LHab} (%)	P_G^{LHcb} (%)	P_{PP}^{LHdb} (%)	P_{LR}^{MHab} (%)	P_G^{MHcb} (%)	P_{PP}^{MHdb} (%)
H I 1215	2.87 ^e	8.29	< 0.1	< 0.1	< 0.1
Mg I 2852	0.15	0.08	0.05	7.3	10.4	8.6	< 0.1	< 0.1	< 0.1	2.1	2.0	1.9
Fe II 2374	0.21	0.17	0.13	31.2	24.0	19.6	3.2	0.5	0.5	10.0	7.7	6.3
Fe II 2586	0.30	0.25	0.20	21.6	5.9	8.5	11.6	4.8	5.5	41.2	47.9	42.5
Fe II 2600	0.41	0.46	0.39	78.8	91.2	99.5	64.5	44.5	51.2	46.1	52.4	50.4
C II 1334	0.61	0.44	0.42	2.0	4.3	4.3	12.3	10.5	9.5	65.9	96.8	95.3
C IV 1548	0.72	0.48	0.42	7.6	22.2	18.6	8.1	26.6	20.6	95.1	75.7	74.1
C IV 1550	0.62	0.37	0.28	6.2	33.8	22.7	3.0	7.3	6.5	46.0	56.7	50.5
Si II 1526	0.36	0.25	0.29	0.3	0.3	0.5	17.0	16.8	16.9	2.3	4.7	4.5
Si IV 1393	0.46	0.27	0.64	5.2	32.9	21.6	32.3	5.6	8.4	10.0	8.3	10.8
Al II 1670	0.33	0.21	0.24	1.4	1.8	1.9	6.8	9.7	10.8	41.8	44.9	42.1
Al III 1854	0.14	0.15	< 0.01	30.1	24.4	31.8	< 0.1	0.3	< 0.1	< 0.1	< 0.1	< 0.1

^a Log Rank Probability.

^b Superscripts represent samples compared: ‘L’, ‘M’, and ‘H’ are the low, medium, and high redshift samples, respectively.

^c Gehan Probability.

^d Peto-Prentice Probability.

^e Too few data points.

Table 16
Two Sample Tests, $W_{\text{Ion}}/W_0^{\lambda 2796}$: Weak vs Strong $W_0^{\lambda 2796}$

Ion	Median, $0.3\text{\AA} \leq W_0^{\lambda 2796} \leq 1.0\text{\AA}$	Median, $W_0^{\lambda 2796} > 1.0\text{\AA}$	P_{LR}^a (%)	P_G^b (%)	P_{PP}^c (%)
H I 1215	6.89	5.44	28.1	44.2	44.2
Mg I 2852	0.05	0.10	3.4	2.0	1.8
Fe II 2374	0.10	0.17	22.6	63.5	33.2
Fe II 2586	0.18	0.26	38.8	82.5	53.0
Fe II 2600	0.37	0.47	4.4	4.7	4.1
C II 1334	0.68	0.43	43.9	12.7	11.4
C IV 1548	0.97	0.29	2.7	0.2	0.2
C IV 1550	0.70	0.19	1.3	0.1	0.1
Si II 1526	0.28	0.30	95.2	80.4	85.2
Si IV 1393	0.61	0.19	0.1	0.1	0.1
Al II 1670	0.15	0.31	5.2	10.6	6.6
Al III 1854	< 0.01	0.04	87.3	48.4	94.7

^a Log Rank Probability.

^b Gehan Probability.

^c Peto-Prentice Probability.

Table 17Two Sample Tests, $W_{\text{Ion}}/W_0^{\lambda 2796}$: Weak vs Strong $W_0^{\lambda 2796}$
Two Redshift Bins

Ion	Median, $0 < z < 2$	Median, $z \geq 2$	P_{LR}^a (%)	P_G^b (%)	P_{PP}^c (%)
$0.3\text{\AA} \leq W_0^{\lambda 2796} \leq 1.0\text{\AA}$					
H I 1215	2.87	2.53	0.1	< 0.1	< 0.1
Mg I 2852	0.10	0.17	1.5	5.6	1.7
Fe II 2374	0.13	0.18	31.9	66.1	35.3
Fe II 2586	0.20	0.32	43.8	41.4	37.3
Fe II 2600	0.28	0.52	51.0	55.6	50.2
C II 1334	0.66	0.48	35.9	32.2	29.9
C IV 1548	0.80	0.47	59.9	77.2	73.1
C IV 1550	0.63	0.38	31.8	34.7	34.1
Si II 1526	0.21	0.29	22.2	50.9	43.4
Si IV 1393	0.50	0.25	5.3	16.2	19.6
Al II 1670	0.15	0.29	96.7	55.2	80.0
Al III 1854	0.17	0.17	2.5	4.8	2.2
$W_0^{\lambda 2796} > 1.0\text{\AA}$					
H I 1215	9.98	8.20	0.6	0.7	0.7
Mg I 2852	0.04	0.07	< 0.1	0.7	< 0.1
Fe II 2374	0.09	0.15	11.5	1.7	2.8
Fe II 2586	0.18	0.24	1.1	1.1	0.9
Fe II 2600	0.36	0.47	7.2	21.9	18.1
C II 1334	< 0.01	0.41	98.8	60.7	61.8
C IV 1548	0.81	0.22	2.2	3.6	3.1
C IV 1550	0.63	0.17	0.3	1.8	1.7
Si II 1526	0.28	0.27	44.9	88.2	86.5
Si IV 1393	0.79	< 0.01	79.6	81.1	75.7
Al II 1670	0.16	0.32	25.4	46.5	43.3
Al III 1854	< 0.01	0.04	< 0.1	0.2	0.2

^a Log Rank Probability.^b Gehan Probability.^c Peto-Prentice Probability.